Engineering Multicomponent Nanostructures for MOSFET, Photonic Detector and Hybrid Solar Cell Applications

Asghar Jamshidi Zavaraki

Doctoral Thesis in Theoretical Chemistry & Biology

School of Biotechnology

KTH Royal Institute of Technology

Stockholm, Sweden, 2015

Cover illustration:

- *On top: MOSFET device with four main parts - source, drain, channel and gate.*
- *On the right: Photonic detector device, containing p-i-n heterostructure on Si wafer.*
- *On the left: QD solar cell device containing quantum dots attached to photoanode, electrolyte and counter electrode.*

© Asghar Jamshidi Zavaraki, Dec 2015

TRITA-BIO Report 2015:16
ISSN 1654-2312
ISBN 978-91-7595-772-2
Stockholm, Sweden, 2015

Abstract

Silicon technology has been seeking for a monolithic solution for a chip where data processing and data communication is performed in the CMOS part and the photonic component, respectively. Traditionally, silicon has been widely considered for electronic applications but not for photonic applications due to its indirect band gap nature. However, band structure engineering and manipulation through alloying Si with Ge and Sn has opened new possibilities. Theoretical calculations show that it is possible to achieve direct transitions from Ge if it is alloyed with Sn. Therefore, a GeSn system is a choice to get a direct band gap. Extending to ternary GeSnSi and quaternary GeSnSiC structures grown on Si wafers not only makes the band gap engineering possible but also allows growing lattice matched systems with different strain and band gaps located in the infrared region. Different heterostructures can be designed and fabricated for detecting light as photonic sensing or emitting the light as lasers. Alloying not only makes engineering possible but it also induces strain which plays an important role for electronic applications. Theoretical and experimental works show that tensile strain could increase the mobility, which is promising for electronic devices where high mobility channels for high performance MOSFETs is needed to speed up the switching rate. On the other hand, high n-doping in tensile strains in p-i-n structures makes Γ band transitions most probable which is promising for detection and emission of the light. As another benefit of tensile strain, the direct band gap part shrinks faster than the indirect one if the strain amount is increased.

To get both electronic and photonic applications of GeSn-based structures, two heterostructures (Ge/GeSn(Si)/GeSi/Ge/Si and Ge/GeSn/Si systems), including relaxed and compressive strained layers used to produce tensile strained layers, were designed in this thesis. The low temperature growth is of key importance in this work because the synthesis of GeSn-based hetrostructures on Si wafers requires low thermal conditions due to the large lattice mismatch which makes them metastable. RPCVD was used to synthesize these heterostructures because not only it offers a low temperature growth but also because it is compatible with CMOS technology. For utilization of these structures in devices, n-type and p-type doping of relaxed and compressive strained layers were developed. HRRLMs, HRTEM, RBS, SIMS, and FPP techniques were employed to evaluate strain, quality, Sn content and composition profile of the heterostructures.

The application of GeSn-based heterostructures is not restricted to electronics and photonics. Another application investigated in this work is photovoltaics. In competition with Si-based solar cells, which have, or are expected to have, high stability and efficiency, third generation solar cells offer the use of low cost materials and production and can therefore be an alternative for future light energy conversion technology. Particularly, quantum dot sensitized solar cells

are associated with favorable properties such as high extrinsic coefficients, size dependent band gaps and multiple exciton generation and with a theoretical efficiency of 44%. In this work, two categories of QDs, Cd-free and Cd-based QDs were employed as sensitizers in quantum dot sensitized solar cells (QDSSCs). Cd-based QDs have attracted large interest due to high quantum yield, however, toxicity remains still to their disadvantage. Mn doping as a band gap engineering tool for Cd-based type II ZnSe/CdS QDs was employed to boost the solar cell efficiency. Theoretical and experimental investigations show that compared to single core QDSSCs, type II core-shells offer higher electron-hole separation due to efficient band alignment where the photogenerated electrons and holes are located in the conduction band of the shell and valence band of the core, respectively. This electron-hole separation suppresses recombination and by carefully designing the band alignment in the device it can increase the electron injection and consequently the power conversion efficiency of the device.

Considering eco-friendly and commercialization aspects, three different "green" colloidal nanostructures having special band alignments, which are compatible for sensitized solar cells, were designed and fabricated by the hot injection method. Cu_2GeS_3-InP QDs not only can harvest light energy up to the infrared region but can also be used as type II QDs. ZnS-coating was employed as a strategy to passivate the surface of InP QDs from interaction with air and electrolyte. In addition, ZnS-coating and hybrid passivation was applied for $CuInS_2$ QDs to eliminate surface traps.

Keywords:

Epitaxial Growth, Reduced Pressure Chemical Vapor Deposition, GeSnSiC, MOSFET, Photonic Detector, Resistivity, Phosphor and Boron doping, Colloidal QDs Sensitized Solar Cell, Cd-free and Cd-based QDs, High Resolution Reciprocal Lattice Map, High Resolution X-Ray Diffraction, High Resolution Transmission Electron Microscopy, High resolution Scanning Electron Microscopy.

Preface:

This doctoral thesis gives a report of the research carried out at the department of Theoretical Chemistry and Biology, School of Biotechnology (BIO), and at the department of Integrated Devices and Circuits, School of Information and Communication Technology (ICT), both at the Royal Institute of Technology. It includes a summary introduction and the appended publications listed below:

I. **A. Jamshidi**, M. Noroozi, M. Moeen, A. Hallén, B. Hamawandi, J. Lu, L. Hultman, M. Östling and H. Radamson, "Growth of GeSnSiC Layers For Photonic Applications", Surface and Coatings Technology, 2013. 230: p. 106-110.

II. M. Noroozi, **A. Jamshidi**, M. Östling, and H. H. Radamson, "Growth of GeSnSi Alloys by Reduced Pressure CVD", Manuscript (published with changes in ECS Transactions, 2014. 64(6): p. 703-710).

III. H. H. Radamson, M. Noroozi, **A. Jamshidi**, P. E. Thompson, and M. Östling, "Strain Engineering In GeSnSi Materials", ECS Transactions, 2012. 50(9): p. 527-531.

IV. C. Hu, P. Xu, C. Fu, Z. Zhu, X. Gao, **A. Jamshidi**, M. Noroozi, H. Radamson, D. Wu, and S. L. Zhang, "Characterization Of Ni(Si,Ge) Films On Epitaxial Sige(100) Formed By Microwave Annealing", Applied Physics Letters, 2012. **101**(9).

V. **A. Jamshidi**, C. Yuan, V. Chmyrov, J. Widengren, L. Sun, and H. Ågren, "Efficiency Enhanced Colloidal Mn-Doped Type Core/Shell Znse/Cds Quantum Dot Sensitized Hybrid Solar Cells", Journal of Nanomaterials, (2015) 921903.

VI. **A. Jamshidi**, J. Huang, Y. Ji, V. Chmyrov, J. Widengren, Y. Luo, L. Sun and H. Ågren, "Synthesis of Cd-Free and Low Toxic Cu_2GeS_3-Inp Quantum Dots For Infrared Solar Cell Applications", Manuscript

VII. **A. Jamshidi**, V. Chmyrov, J. Widengren, L. Sun and H. Ågren, "Green" Colloidal InP/ZnS Quantum Dot Sensitized Solar Cells, Manuscript.

VIII. J. Huang, B. Xu, **A. Jamshidi**, L. Sun and H. Ågren, "Strategies to Improve Photovoltaic Performance of "Green" $CuInS_2$ Quantum Dots: Hybrid Passivation vs Use of ZnS shells", Manuscript.

Author contribution to the papers

In paper **I**, the author performed synthesis, characterization, calculation, writing of the first draft of the paper.

In papers **II-III**, the author took part in the main synthesis, characterization, comments, disscussions as well as preparation of the paper.

In paper **IV**, the author performed structural characterization, calculation and took part in in the preparation of the paper.

In papers **V- VII** the author implemented synthesis, fabrication, measurement, calculation and writing of the paper.

In paper **VIII** the author contributed in comments and revisions of the paper as well as co-writing of the introduction.

Conference abstracts

I. **A. Jamshidi**, C. Yuan, J. Huang, L. Sun, H. Ågren, "Type II Manganese-Doped ZnSe/CdS QDs Sensitized Solar Cells", IPS20, July-August 2014, Berlin, Germany

II. **A. Jamshidi**, M. Noroozi, H. H. Radamson, "Strain Effect On Sn Incorporation in GeSnSi", Euro CVD 1 , September 2013, Bulgaria

III. M. Noroozi, **A. Jamshidi**, M.S. Toprak and H. H. Radamson, “Effect of Strain on Phase Formation of Ni Tin-Germanide”, EMRS, France, May 2013.

List of papers not included in the thesis

I. S. Majdi, M. Kolahdouz, M. Moeen, **A. Jamshidi**, K. K. Kovi, R. S. Balmer, H. H. Radamson and J. Isberg, High Performance Temperature Sensors using SC-CVD Diamond Schottky Diodes, manuscript (published with change in Applied Physics Letters , 2014. 105, 163510).

Acknowledgments

My research and study as PhD student under the supervision Prof. Hans Ågren, head of the department of theoretical chemistry and biology, has given me a great opportunity to learn how to work and collaborate systematically in science projects. I have had a great time working under Hans' supervision. He runs a competitive experimental group with nice atmosphere, and his expert supervision with continuous support encouraged me to work with high energy and without any stress. I appreciate and thank you Hans a lot with my sincerest and deepest gratitude.

I would like to thank Prof. Licheng Sun, my supervisor at the dept. of Molecular Devices, and Prof. Mikael Östling, my supervisor at the dept. Integrated Circuits and Devices for helpful advice and support.

I gratefully appreciate Prof. Paras Prasad at the Institute for Lasers, Photonics and Biophotonics, the State University of New York at Buffalo, for offering me the opportunity to work in his group and Dr. Guanying Chen for his enthusiastic help during my short visit in USA.

I especially thank Dr.Chunze Yuan, Jing Huang and Dr.Yongfei Ji for helpful advice, nice discussions and collaboration. Prof. Yi. Luo, Prof. Jerker Widengren and Volodmyr Chmyrov are warmly acknowledged for collaboration.

I also appreciate all professors, doctors and colleagues at the department for their time, nice comments and discussions in seminars as well as for all help during my PhD period.

Finally, I would like to send my greatest gratitude to all members of my family and family in law, especially my parents and parents in-law. My lovely family, my wife Roghayeh and my daughter Masoumeh, please accept my warmest and deepest gratitude; I dedicate my thesis to you.

At the end, I acknowledge the Ministry of Science, Research and Technology of Iran for offering me a PhD scholarship.

List of symbols and abbreviations

n-type	Boron-doped
Γ-band	Indirect bandgap valley
L-band	Direct bandgap valley
CMOS	Complementary metal oxide semiconductor
MOSFET	Metal oxide semiconductor field effect transistor
p-type	Phosphor-doped
Θ	Incident angle
Ω	Reflected angle
MBE	Molecular beam epitaxy
CVD	Chemical vapor deposition
APCVD	Atmospheric pressure chemical vapor deposition
RPCVD	Reduced pressure chemical vapor deposition
UHCVD	Ultra-high vacuum chemical vapor deposition
UV	Ultra violet
IR	Infrared
PECVD	Plasma enhanced CVD
FETs	Field effect transistors
MESFET	Metal semiconductor FET
IGFET	Insulated gate FET
JFETs	Junction FETs
DSSCs	Dye sensitized solar cell
FTO	Flour tin oxide
Red/Ox	Reduced/Oxidized
QD	Quantum dot
MEG	Multiple exciton generation
QDSSC	Quantum dot sensitized solar cell
SILAR	Successive ionic layer adsorption and reaction
IPCE	Incident photon to current efficiency
LHE	Light harvesting efficiency
APCE	Absorbed photon current efficiency
Ff	Fill factor
V_{oc}	Open circuit voltage
J_{sc}	Short circuit current
Mtorr	Mili torr
DI	Deionized water
P	Phosphor
B	Boron
Vir	Virtual
MWA	Microwave Annealing

RTA	Rapid Thermal Processing
TOP	Trioctylphosphine
OA	Oleic acid
ODE	Octadecane
ODA	Octadecylamine
DDT	1-dodecanethiol
OLA	Oleylamine
ICP-AES	Inductively coupled plasma atomic emission spectroscopy
TEM	Transmission electron microscopy
HRRLMs	High Resolution Reciprocal Lattice Maps
HRSEM	High Resolution Scanning Electron Microscopy
EDS	Energy Dispersive Spectroscopy
FPP	Four-Point-Probe
RBS	Rutherford Backscattering Spectroscopy
MQW	Multi quantum well

Table of the contents

Abstract……… i
Preface……… iii
Author contribution to the papers……… iv
Conference abstracts……… iv
List of papers not included in the thesis……… iv
Acknowledgments……… v
List of symbols and abbreviations……… vi

CHAPTER 1: Introduction

1.1. Nanotechnology……… 1
1.2. Semiconductor materials and semiconductor technology……… 1
1.3. Group IV semiconductors and their importance……… 2
1.4. Strain and strain engineering in Group IV materials……… 3
1.4.1. Lattice-matched and mismatched systems……… 3
1.4.2. Strain……… 3
1.4.3. Lattice mismatch and mismatch parameters……… 3
1.4.4. Uniaxial and biaxial strain……… 4
1.4.5. Tensile and compressive strain……… 4
1.5. Methods to growth and generate strain of group IV -based epitaxial layers……… 5
1.6. Solar cell technology……… 5
1.6.1. Categories of solar cell technology……… 6
1.7. Focus of this work……… 6

CHAPTER 2: Photonic Detectors, MOSFETs and Hybrid Solar Cells

2.1. Detectors, applications and categories……… 7
2.2. Basic principles of thermal detectors……… 7
2.2.1. Basic principles of photonic detectors……… 7
2.2.2. Technological progress and challenges for development of photonic detectors……… 8
2.3. Categories of Transistors……… 9
2.3.1. Basic principles of field effect transistors……… 9
2.3.2. Basic principles of MOSFETs……… 10
2.3.3. Technological progress and challenges for development of MOSFETs……… 10
2.4. Third generation solar cells……… 11
2.4.1. Dye sensitized solar cells……… 11
2.4.2. Perovskite solar cells……… 12
2.4.3. Quantum dot sensitized solar cell……… 13
2.4.3.1. Quantum dots……… 13
2.4.3.2. Categories of quantum dots……… 13
2.4.3.2.1. Type I core-shell quantum dots……… 13
2.4.3.2.2. Type II core-shell quantum dots……… 14
2.4.3.2.3. Core/ multi-shell quantum dots……… 14

2.4.3.2.4. Alloyed quantum dots……15
2.4.3.3. Advantages of quantum dots as sensitizers in solar cells……15
2.4.3.3.1. Multiple exciton generation effect……15
2.4.3.3.2. Size-dependent properties……16
2.4.3.4. Basic principles of QD sensitized solar cells……17
2.4.3.5. Overview of QD sensitized solar cells……19

CHAPTER 3: Experimental Aspects

3.1. Epitaxial layers……21
3.1.1. Materials and gas sources……21
3.1.2. Deposition technique and specifications……21
3.1.3. Wafer cleaning……22
3.1.4. Epitaxy growth of tensile Ge, pure and Phosphor (Boron)-doped GeSn on Si……22
3.1.5. Epitaxy growth of Ge, GeSnSi and GeSnSiC……23
3.1.6. Epitaxy growth of SiGe and Ni silicidation……24
3.1.7. Epitaxy growth of multi quantum wells of GeSn/Ge and Phosphor(Boron)-doped GeSn…25
3.1.8. Epitaxy growth of GeSn-based p-i-n structures proposed for photonic and electronic applications……26
3.2. Colloidal quantum dots……26
3.2.1. Materials……26
3.2.2. Method and instrument……26
3.2.3. Synthesis of ZnSe single core QDs……27
3.2.4. Synthesis of pure and Mn-doped type ll ZnSe/CdS core/shell QDs……27
3.2.5. Synthesis of Cu_2GeS_3 single core QDs……28
3.2.6. Synthesis of type II Cu_2GeS_3/InP core/shell QDs……28
3.2.7. Synthesis of InP single core and ZnS-coated InP QDs……28
3.2.8. Photoelectrode……28
3.2.9. Counter electrode……29
3.2.10. Electrolyte……29
3.2.11. QD solar cell assembly……29

CHAPTER 4: **Results and Discussion**

4.1. GeSn and its potential for utilization in photonic detectors and MOSFETs……30
4.2. Strain relaxed layers and their utilization to produce tensile strain for photonic detectors and MOSFETs……30
4.2.1. HRRLMs of GeSn grown on Si substrates……31
4.2.2. Estimation of Sn content from HRRLMs and RBS in GeSn layers……31
4.2.3. Morphology characteristics of GeSn/Si systems measured by SEM……32
4.2.4. Resistivity measurements of phosphor (boron)-doped GeSn/Si grown in different temperature……33
4.3. Compressive strain layers and their utilization to produce tensile strain for photonic detector and MOSFETs……34
4.3.1. TEM image of multi quantum wells of GeSn with different Sn content ……34
4.3.2. Resistivity measurements of phosphor (boron)-doped GeSn/Ge grown at different temperature……35
4.3.3. HRRLMs of GeSn/Ge system grown at different temperature……35

4.3.4. Thermal stability of the GeSn/Ge system…............……………..……..……………..……….36
4.3.5. Effect of P and B on incorporation of Sn…...……………...……………………….……....…...37
4.3.6. Strain engineering by incorporation of C and Si in GeSn matrices …...…….……….……..…..37
4.3.7. Effect of Si on incorporation of Sn …...…………………...…………………...…..…….…..38
4.3.8. Effect of Si and C on morphology of GeSn-based layers………………...………………...39
4.4. Tensile strain layers for photonic detectors and channel MOSFETs….......………………..40
4.4.1. Tensile Ge obtained from Ge/GeSn/Si system…...……………………...………………...40
4.4.2. Tensile Ge quality measured by HRTEM…...……………….……...……………….…….40
4.4.3. Strain amount in tensile Ge measured by HRRLMs…...…………………...……………...41
4.4.4. Tensile Ge obtained from Ge/GeSn(Si)/GeSi/Ge/Si system…...…...............……………..41
4.5. Nickel silicidation of the strained SiGe formed by RTP and MWA for source/drain of MOSFETs …...…………………...…………………...……….……….....……………...42
4.5.1. Annealing strategies: challenges and alternatives……...…………………...…………...…43
4.5.2. Resistivity measurements of NiSiGe layers……...………………………...…...……..…43
4.5.3. Measurements of NiSiGe layers by cross-sectional TEM……...…………………...…...…44
4.5.4. Measurements of NiSiGe layer by HRRLMs……...…………………...……………….…44
4.6. Quantum dot sensitized solar cells……...…………………….……………...……......45
4.6.1. Cd-based quantum dot sensitized solar cells……...………...…………………...……......45
4.6.1.1. Band gap engineering, effect of Mn dopants on optical properties of QDs ……....……..46
4.6.1.2. Performance assessment of device sensitized with Mn-doped ZnSe/CdS QDs 47
4.6.1.3. Study of excited state dynamics of ZnSe/CdS doped with different Mn concentrations.…49
4.6.2. Cd-free "green" quantum dot sensitized solar cells.……………………………...….……51
4.6.2.1. Optical and structural properties of Cd-free QDs….…………………...…….……………51
4.6.2.1.1. Cu2GeS single core and type II Cu_2GeS_3/InP core/shell QDs………...……………….…….51
4.6.2.1.2. InP single core and ZnS shell-coated InP QDs ………...……….……….……...…….…...52
4.6.2.1.3. $CuInS_2$ single core and ZnS-coated CuIns2 QDs………...……..……….………...………..53
4.6.2.2. Performance assessment - J-V and IPCE characteristics………...............……….…...…55
4.6.2.2.1. Cu_2GeS_3 single core and type II Cu_2GeS_3/InP QDs……………………....……….………55
4.6.2.2.2. ZnS-coated InP QDs………...…….……….…..…….……………….…...…….…………56
4.6.2.2.3. ZnS-coated $CuInS_2$ QDs………...…….……….……...…………………….…...………..57
4.6.2.3. Study of excited state dynamics of Cu_2GeS_3 single core and type II Cu_2GeS_3/InP QDs.…59

CHAPTER 5: **Conclusions and Future Outlook**

5.1. Conclusions…….…………...…………….………...…………………...………...…...…62
5.2. Future outlook..…….………… …….………...…...…………….………..………...64
References……............…….………….…………...……….………………...…………….……….…66

CHAPTER 1

Introduction

1.1. Nanotechnology

The term 'Nano' derives from the Greek word 'Nanos' meaning 'dwarf', and has become synonymous with one of the most swiftly developing and promising branches within natural science and technology. The term is nowadays used to label a wide range of contemporary technologies, like nanoelectronics, nanophotonics, nanolithography, nanobiotechnology and nanomedicine, which are based on materials and particles structured at the "nano" scale. Since the most conspicuous properties of "nanomaterials" appear for structures smaller than 100 nm, "nanotechnology" often refers to technology dealing with the scale from this limit all the way down to the atomic dimension of 0.2 nm. Nanocrystals and nanoparticles can thus be defined for crystals and particles having at least one dimension in that nanoscale[1]. The success of nanotechnology can essentially be traced to two outstanding properties of nanostructured materials; quantum confinement, leading to discrete energy states that are size-dependent[2], and the ability to support collective electron oscillations - plasmons. A third dimension of nanotechnology, or nanoparticle technology, has recently emerged, namely the ability of specifically designed nanoparticles to selectively convert incident light into other spectral regions. Nanomaterials show different properties than the properties in the bulk scale owing to the surface effect. In the nano scale, the atoms have fewer neighbors and unsatisfied bonds as the fraction of the atoms at the surface is increased and show binding properties that are much altered from that of bulk. New interesting properties - optical, mechanical, magnetic and electrical properties - thus appear for materials at the nano scale, laying the ground for new technologies within chemistry, chemical engineering, physics, material science, mechanics, electronics, photonics and medicine, to mention some of the main application areas[3].

1.2. Semiconductor materials and semiconductor technology

As a scientific term the word 'Semiconducting' or "Semiconductor" dates back to 1782 when Alexander Volta and his colleagues discovered electrical conductivity[4]. Based on the definition of electrical conductivity, semiconductors are categorized in two basic classes, namely intrinsic and extrinsic semiconductors. Intrinsic semiconductors refer to pure

semiconductors having a few but equal number of electrons and holes. Extrinsic semiconductors refer to semiconductors having excess or shortage of electrons and are made by adding impurities into intrinsic semiconductors. Depending on which type of impurity is doped into the intrinsic semiconductor, the extrinsic one is divided into n-type and p-type semiconductors having excess and shortage of electrons, respectively. By introducing dopants these semiconductors vary their properties like electrical conductivity and thermal stability. This has been the basis a for a technology called semiconductor technology for manufacturing devices with wide applications in the areas of photovoltaics[5], transistors[6, 7], photodetectors[8] and thermoelectrics[9].

1.3. Group IV semiconductors and their importance

Among different types of semiconductors, Group IV materials (Si, Ge, Sn and C) have attracted large interest in electronics and photonics technology. In particular Si, one of the most abundant elements found in nature, and Ge, which is less abundant, have found numerous applications. For example, Si and Ge have been used for fabrication of high speed transistors [10] and photonic detectors [11]. **Figure 1.1** shows the electronic band structures of Si and Ge.

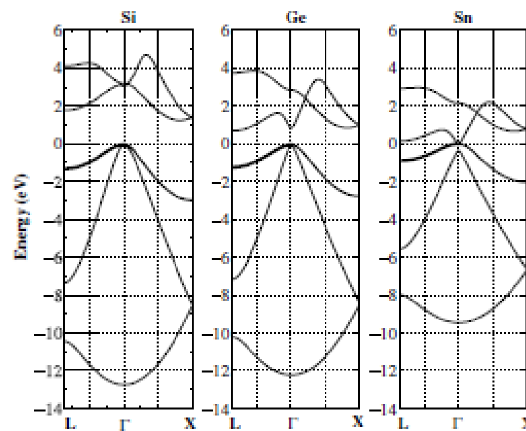

Figure 1.1: Electronic band structures of Si , Ge and Sn[12]

Since Si and Ge possess indirect band gaps[12], alloying the two compounds or allying with Sn and C makes it possible to engineer the their band gaps to smaller values and thereby open the possibility for a wider range of photonic and electronic applications. Introducing strain is a band gap engineering tool that may lead to a more effective shrinking of the direct band gaps (Γ-band) rather than in the indirect band gaps (L-band). This can result in Γ- band transitions suitable for detecting or emitting light [13-15]. The possibility of alloying and introducing strain in Group IV semiconductors to get direct band gaps, are two important aspects that have made these materials compatible with Si technology, and that provide an alternative for group III–V materials in semiconductor technology[12]. As an example, introducing compressive strain and tensile strain in Ge can increase the hole mobility and electron mobility, respectively [16, 17]. Introducing Sn into Ge is another possible way of engineering the electronic structure of Ge to boost the mobility in GeSn alloys for utilization in

high speed complementary metal oxide semiconductor (CMOS) devices [18]. Since the crystal size of GeSn is larger than for Si, Ge and SiGe, it is expected to have high flexibility of strain and a larger band gap that is demanded by the technology for electronic and photonic devices in integrated circuits. This thesis concerns both electronic and photonic properties of GeSn-based devices and pays attention to their application as metal oxide semiconductor field effect transistors (MOSFETs) and photonic detectors for utilization in CMOS devices.

1.4. Strain and strain engineering in Group IV materials

1.4.1. Lattice-matched and mismatched systems

A lattice matched system is a system in which the lattice constant of the over-epitaxy layer is similar to the lattice constant of the substrate. AlGaAs/GaAs is an example of a lattice matched system. In such systems high quality epitaxial layers with negligible defects can be obtained. In lattice mismatched systems, for example SiGe/Si and Ge/GeSn, the lattice constant of the epitaxial layer (SiGe, Ge) is larger or smaller than the lattice constant of the substrate (Si,GeSn). This results in strain in the epitaxial layer if the thickness of the overlayer is very thin.

1.4.2. Strain

The built-in strain in lattice mismatched structures affects the electronic and optoelectronic properties of the strained layers so that it can be utilized for boosting the device performance[19, 20]. Lattice mismatched systems based on group 4 alloy materials, where Si is the only high quality and cheap substrate, can be grown to introduce strain with wide possibilities of engineering the band gap. The lattice constant of alloyed layers can be calculated from Vega's law[12]:

$$a_L(x)^{AB} = (1-x)a_L^A + xa_L^B \tag{1.1}$$

where a_L^A and a_L^B are lattice constants of elements contributing in the layer.

1.4.3. Lattice mismatch and mismatch parameters

The difference of lattice constant between layer and substrate is defined by mismatch and strain components. The mismatch (f) and strain (ε) in parallel and perpendicular to a plane-lattice are derived from:

$$f_{\perp} = \frac{a_L^{\perp} - a_S}{a_S} \qquad f_{||} = \frac{a_L^{||} - a_S}{a_S} \tag{1.2}$$

$$\varepsilon_{\perp} = \frac{a_L^{\perp} - a_L}{a_L} \qquad \varepsilon_{||} = \frac{a_L^{||} - a_L}{a_L} \tag{1.3}$$

where a_S and a_L are the actual lattice constants of bulk substrate and layer, respectively. $a_L^{||}$ and $a_L^{\perp}$ are the lattice constants of a layer in parallel and perpendicular to the layer surface. In heterostructures grown on Si substrates, the mismatch parameters parallel and perpendicular to the growth direction can be obtained by the high resolution reciprocal lattice mapping (HRRLM) technique. Using this technique, a series of rocking curves obtained from a ω-2θ scan mode (ω changes with amount of Δω in each rocking curve) are considered (ω and 2θ refer to incident and reflected beams, respectively). The final rocking curves are plotted as contours in K-space. The mismatch parameters ($f_{||}$ and $f_{\perp}$) and lattice mismatch (f) are derived from:

$$f_{||} = \frac{Sin\theta_S \sin(\omega_S - \theta_S)}{Sin\theta_l \sin(\omega_l - \theta_l)} - 1 \quad (1.4)$$

$$f_{\perp} = \frac{Sin\theta_S \cos(\omega_S - \theta_S)}{Sin\theta_l \cos(\omega_l - \theta_l)} - 1 \quad (1.5)$$

$$f = (f_{\perp} - f_{||})\frac{1-\nu}{1+\nu} + f_{||} \quad (1.6)$$

where s, l are indicators of the substrate and epitaxial layer and ν is the Poisson ratio [21, 22].

1.4.4. Uniaxial and biaxial strain

When the epitaxial layer is grown on a substrate with different lattice constants, the lattice constant of the epitaxial layer is strained in both the plane of the substrate and in the growth direction (perpendicular to the surface). These strains are called biaxial if the strain is in two directions and uniaxial if the strain is in one direction.

1.4.5. Tensile and compressive strain

In case of tensile strain, $f_{\perp}\langle 0$, $f_{||} = 0$, $\varepsilon_{\perp}\langle 0$ and $\varepsilon_{||}\rangle 0$, but in compressive strain $f_{\perp}\rangle 0$, $f_{||} = 0$, $\varepsilon_{\perp}\rangle 0$ and $\varepsilon_{||}\langle 0$ [19, 20, 23, 24]. **Figure 1.2** shows the schematics of tensile and compressive strain layers deposited on a substrate.

The strain plays important and major roles in electronics and photonics. For example, by introducing tensile and compressive strains, the electron mobility can be increased and decreased, respectively[25]. The mobility increased by strain has been used to improve the performance of Si-based [26, 27] and GeSn-based MOSFETs T[28]. Alloying Ge with Sn not only introduces strain, used as a strategy in indirect-direct band gap engineering[29] for detecting and emitting[30] light, but also offers the possibility of fabricating high performance electronic devices[28]. Engineering the electronic band structure of Ge by introducing tensile strain has been theoretically examined [31-34] and experimentally confirmed [35-37].

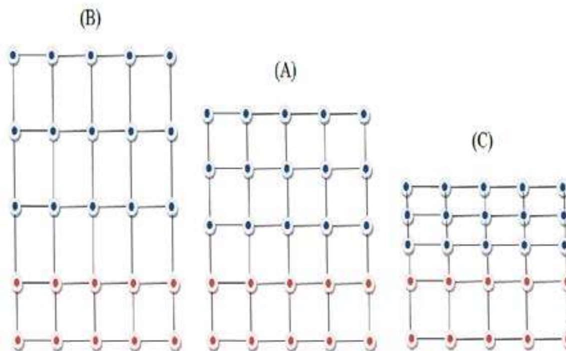

Figure 1.2: Schematic illustration of (A) no strain, (B) compressive strain and (C) tensile strain.

1.5. Methods to grow and generate strain of group IV-based epitaxial layers

Epitaxy means growth of high quality single crystalline layers on a single crystal substrate (usually an Si wafer). If the substrate is not a single crystal or the deposition process is not correct, then amorphous or polycrystalline samples will be grown. There are two main approaches for fabrication of group IV epitaxy layers - Molecular beam epitaxy (MBE) and Chemical vapor deposition (CVD), in which high quality and low defect epitaxial layers can be obtained. GeSn is an example of a novel and interesting alloy in Group IV that has been grown by MBE [38-40]. However, demands from CMOS technology for integrating the devices by commercially available and cheap gas sources on cheap Si substrates often calls for CVD. CVD has also been used for growth of GeSn-based epitaxial layers using SnD_4 gas as Sn source [41]. However, misfit dislocations are then often still seen in the epitaxial layers. Grzybowski et al[42] used SnD_4 as Sn source to grow high quality GeSn directly on Si substrates by ultra-high vacuum. Although the quality of GeSn deposited by ultra-high vacuum CVD (UHCVD) often is acceptable, the necessity of ultra-high vacuum for the deposition can be a negative aspect in the experimental work. The high toxicity of SnD_4 has for a long time been another negative point for using these materials in integrated circuit devices. To avoid SnD_4 as a recipe of an Sn gas source, Vincent et al [43] proposed the utilization of a commercially available Sn source ($SnCl_4$) and managed thereby to grow high quality GeSn epitaxial layers on Ge by atmospheric pressure chemical vapor deposition (APCVD). Based on that experience, this thesis (paper I- III) proposes a higher quality of GeSn grown by reduced pressure CVD (RPCVD) in which oxygen and other contamination compounds would be decreased significantly. This method offers a high growth rate with low cost of epitaxial layers, that is, it could be commercially interesting for fabrication.

1.6. Solar cell technology

As fossil fuels produce pollution and heat, global renewable energy, such as wind, water and solar energy, is called for as it is environment friendly and serves for clean sources of energy. Solar energy is the most abundant and powerful energy source - the energy of the sun fallen to earth in one hour is sufficient for human consumption in one year. Recent progress in nanotechnology has made solar technology a most important technology for converting solar

energy in many countries[44, 45]. Between different types of renewable energy, solar energy has been recognized as the most abundant source of renewable energy and can be utilized in different applications such as solar power plants, solar collectors, solar cells[46]. The first Si-based solar cell was fabricated by Pearson and his co-workers already in 1954[47].

1.6.1. Categories of solar cell technology

Nowadays, and after 60 years, the historical time line of solar cell technology includes three generations. The technology dealing with either single or mono crystalline Si wafers with a typical thickness of 200-300 µm is called the first generation technology. The typical thickness in the second generation technology comprises 1-20 µm semiconductor thin films and is usually called thin film solar cell technology. Amorphous silicon and other non-Si-based semiconductors like CdTe and Cu(In,Ga)(S,Se) are categorized in this generation. The production is cheaper for the second generation amorphous Si (14%) cells compared to the first generation crystalline Si cells. According to theoretical calculations, the maximum efficiency that could be obtained in a single junction crystalline Si is about 33% due to the Queasier thermodynamic limit. Therefore the third generation technology which aims to decrease production cost and increase the efficiency is needed. Perovskite solar cells and sensitized solar cells (with dye and quantum dots as sensitizers) are then categorized as the third generation solar cells [48-51].

1.7. Focus of this work

Based on previous studies showing large advantages of tensile Ge in electronics and photonics, this work presents design and engineering of two tensile Ge on GeSn(Si)-based systems for future utilization in photonic detectors and as MOSFETs in electronics. The focus is on growth of high quality GeSn epitaxial layers in low temperature by RPCVD which is compatible with CMOS technologies for its utilization for electronic and photonic applications. Experimental studies deal with the induction of high Sn contents in GeSn layers and the creation of different strains in the heterostructures as well as p(n)-doping in GeSn-based layers. It also includes silicide (formation of SiNi phase) in SiGe layers.

The third generation solar cells with cheap production as an alternative for Si-based solar cells for solar energy conversion are also investigated in this thesis. The focus is on the synthesis of quantum dots with different components (CdS, ZnSe, In, ZnS, Cu_2GeS_3) and their employment as sensitizers in sensitized solar cells. Different designs, such as single core, type I, type II and Mn-doped QDs were considered for device assembly. Improvement of device performance in terms of component and type of quantum dots where thereby analyzed.

CHAPTER 2

Photonic Detectors, MOSFETs and Hybrid Solar Cells

2.1. Detectors, applications and categories

Optical radiation of light resides in wavelengths between the infrared (IR) to the UV-Visible parts of the electromagnetic spectrum. Group IV based materials deal with the infrared region of radiation due to the nature of their band gaps. The detection of infrared radiation of light has in the past been of much interest due to broad applications in medicine[52], night vision [53] and astronomy[54, 55]. Infrared detectors convert the IR radiation of light with wavelengths of 700 to 3000 nm into another type of measurable energy. Depending on which mechanism is used for detection of the infrared spectrum, IR detectors are categorized into two types, namely thermal and photonic detectors.

2.2. Basic principles of thermal detectors

In thermal detectors, the mechanism of detection is based on that the IR photons are absorbed by a material resulting in an increase of the temperature of that material. The increase in temperature is monitored by changes in temperature dependent phenomena such as resistivity or dielectric constant - in this way IR photons are sensed and converted to measurable parameters. The Golay cell, pyroelectric devices, thermopiles, thermocouples and bolometers are examples of common thermal detectors [56].

2.2.1. Basic principles of photonic detectors

Photonics is often referred to as a science being parallel to electronics. Electronics and photonics are distinguished from each other by the mechanism of transmission, simply by that electrons, respectively, photons, are transmitted [57]. In photonic detectors, photons are absorbed by materials and generate currents that are sensed by electronic circuits. Photonic detectors are based on the excitation by light resulting in carrier generation whereas thermal detectors are based on thermally sensible phenomena. This makes photonic detectors wavelength dependent, while thermal detectors in general are not. Photonic detectors are subdivided into photovoltaic (**Figure 2.1 a)** and photoconductive (**Fig 2.1 b)**.

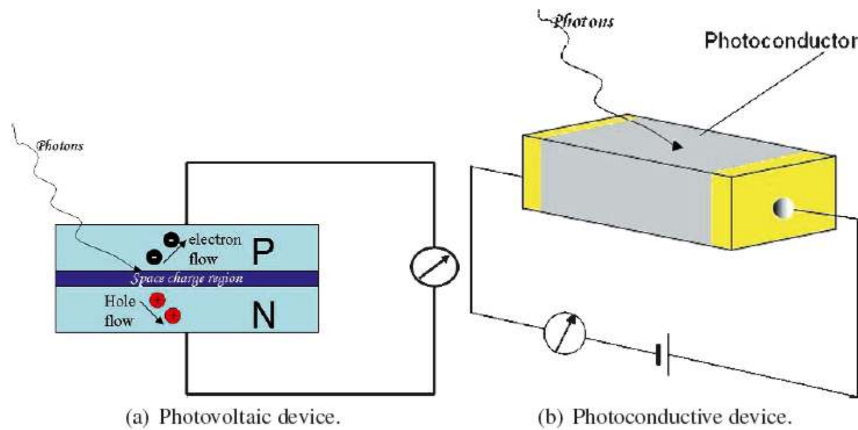

Figure 2.1 : Schematic illustration of basic principles of photoconductive and photovoltaic detectors [58].

The basic principles of photoconductive detectors rely on the fact that the carriers generated by excitation increases the conductivity of the material whereas in photovoltaic detectors an internal potential barrier separates photo-generated electron-hole pairs [56, 58].

2.2.2. Technological progress and challenges for development of photonic detectors

The PbS-based detector developed by Case in 1917 constituted the first photonic detector. It could sense infrared radiation up to 3000 nm. The fast development of IR detectors now includes the use of II-VI, III-V alloy materials for sensing broad parts of the wavelength spectrum in the infrared region [59]. One of the most used alloy materials for IR detection over the last 40 years is HgCdTe due to its broad wavelength coverage - 1000-300000 nm, large optical coefficient and high operation temperature [60]. Since 2000, the most common bulk detectors have been of HgCdTe and InSb types in which the mechanism of detection is related to interband transitions. Nowadays, quantum wells, quantum dots, type II superlattices and quantum dots with type II band-based detectors constitute new technologies for fabrication of IR detectors where the detection mechanism depends on intersubband transitions. Group III-V materials have often been used in these IR detector technologies (quantum wells [61-64], quantum dots [65-72], type-II supperlattices [73-83]. Si technology based on cheap Si substrates has opened a new window for development of group IV-based IR detectors with different wavelength sensitivity.

Fabrication of group 4-based IR detectors on Si substrates, such as Si [84, 85] , Ge [86, 87] and SiGe [88-92]-based IR detectors, are important because they are compatible with CMOS technology used to fabricate Si-based chips. As mentioned, Si and Ge have indirect band gaps, and one way to obtain direct band gaps for utilization in photonic detectors is to alloy them together. In the case of Ge, alloying with Sn can result in a direct band gap. Another way is to induce enough strain so that the direct band gap transition is most probable. Recently, Jay et al[93] fabricated GeSn-based photonic detectors **(Figure 2.2)** by the plasma enhanced CVD (PECVD) method with high response up to 1750 nm wavelength of InGaAs detectors. Werner et al[94] (**Figure 2.3 a**) and Su et al [95] (**Figure 2.3 b**) also fabricated GeSn-based

photodetectors by Molecular Beam Epitaxy. The photoresponse of these detectors covered the wavelength of telecommunication and more.

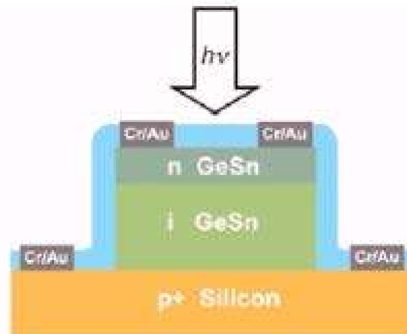

Figure 2.2: Schematic illustration of a GeSn-based p-i-n photodetector: phosphor-doped silicon/ intrinsic GeSn/boron doped GeSn[93]

Although previously published papers show good photoresponse from GeSn-based detectors their use is hampered by that the growth of such structures is expensive. On the other hand, RPCVD not only involves a fabrication process which is compatible with CMOS technology but also provides the application of a cheap source of Sn for growth of GeSn-based structures.

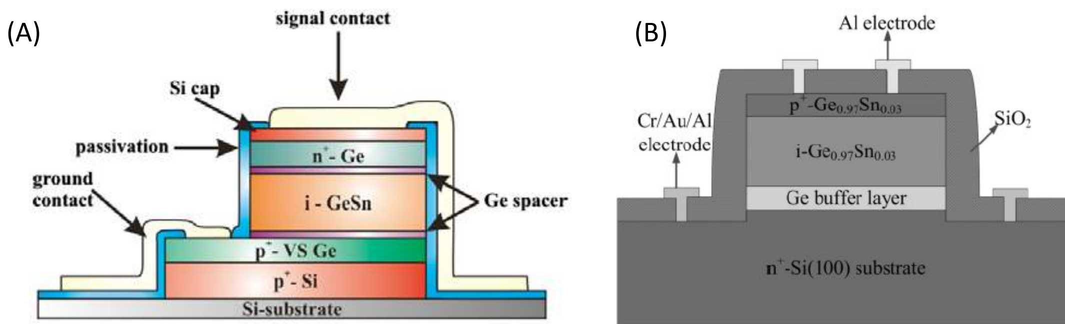

Figure 2.3: Schematic of GeSn p-i-n photo detector: (A) p-type Si substrate/P-doped virtual Ge/intrinsic GeSn/B-doped Ge[94] (B) n-type Si substrate/virtual Ge/intrinsic GeSn/P-doped GeSn[95].

2.3. Categories of Transistors

Transistors containing at least three terminals are electronic devices which can be used for amplifying or switching in integrated circuits. In a typical categorization of different types of transistors, the transistors are divided into bipolar transistors and field effect transistors.

2.3.1. Basic principles of field effect transistors

Field effect transistors (FETs) are transistors in which the channel conductivity can be modulated by applying an electric field on the gate. **Figure 2.4** shows the basic working principles of FETs. As illustrated in this figure, carriers (electrons or holes) flow from source to drain through the channel. The source and drain contacts are ohmic and it is very important

for the channel to be isolated from gate so that there is no carrier flow from gate to channel. In MOSFETs the channel is isolated from the gate by an oxide layer [19].

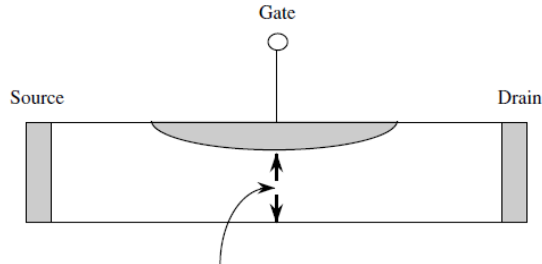

Figure 2.4: Schematic illustration of typical FETs containing source, drain and gate. The gray part between source and drain is called channel[19].

2.3.2. Basic principles of MOSFETs

Depending on which way the gate is formed in FETs, they are divided into MESFETs (metal–semiconductor FETs), IGFETs (insulated-gate FETs) and JFETs (junction FETs). IGFETs are further divided into MESFETs and MOSFETs in which metal semiconductor and metal oxide semiconductor systems are used as gate, respectively. MOSFETs are most important transistors in the IGFET family and serve as forefront devices in integrated circuits of microprocessors and memories. **Figure 2.5** shows the basic characteristics of MOSFETs[96]. Depending on type of doping in the channel, p-channel MOSFETs and n-channel MOSFETs are categorized for MOSFETs[97].

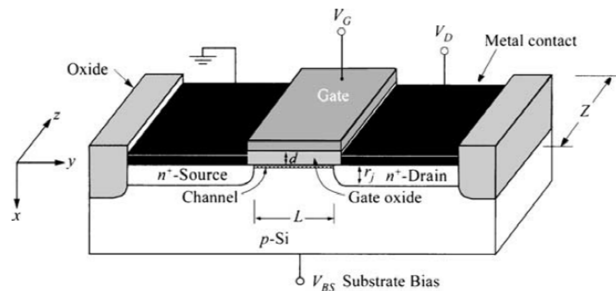

Figure 2.5: Basic schematic characteristics of a MOSFET. L and d are the length and the thickness of channel, respectively [96]

2.3.3. Technological progress and challenges for development of MOSFETs

A lot of experience has been gained for the fabrication of MOSFETs by different materials. SiC-based[98-104] Si-bas[105-110], Ge-based[111-119], SiGe[120-123], SiGe/Si[124, 125] GaAs-based[126-135], InGaAs-based[129, 136-142], InGaAs/GaAs-based[143] MOSFETS are examples of MOSFETs that have been studied so far. It is predicted that new materials with higher mobility will be deposited on Si substrates with fast development of CMOS technology. Ge and group III-V materials are now widely used as alternatives for Si channel materials[144].

Theoretical calculations of Jay et al [18] suggest the possibility of high mobility in GeSn alloyed materials through combination of strain and alloying. They considered two ways to increase electron mobility. One way was to grow the tensile strain of GeSn with 12.4% Sn content to get 2.5% tensile strain with a substantial mobility increase. Another way was to alloy Ge with 15% Sn content to get a larger lattice constant. For hole mobility, they found that about 1% biaxial strain can increase the phonon limited mobility up to 4 times and consequently a growth of strained Ge on GeSn with 12.4% could increase both hole and electron mobility. Supporting the performance benefit of GeSn-based channel MOSFETs, simulations by Suyog et al[145] predicted that the employment of GeSn in nMOSFETs could increase the performance significantly and showed also also that the growth of GeSn on relaxed SiGeSn could lead to strain free or tensile strain GeSn channels. Based on these theoretical studies, some experimental work has been carried out for the fabrication of high mobility GeSn-based materials for MOSFETs as switches in CMOS devices. Han et al [146] fabricated GeSn-based MOSFET channels by the MBE method in ultra-high vacuum. RPCVD is here an alternative for fabrication where not only ultra-high vacuum is not needed but also cheap sources and compatibility with CMOS technology are important advantages.

2.4. Third generation Solar cells

2.4.1. Dye sensitized solar cells

A typical scheme of dye sensitized solar cell (DSSC) device is demonstrated in **Figure 2.6.** The photoanode includes several micrometers film of a few nanometers thick TiO_2, ZnO, Nb_2O_5 or other wide band gap semiconductor nanoparticles stoked onto a conductive glass. A monolayer of dye is attached into the surface of the TiO_2. Electrolytes with organic solvents containing redox couples being injected into the space prepared between photoanode and counter electrode. Photoexcitation of the dye causes electron injection into the metal-oxide conduction band and the original state of dye is reset by the electrolyte [147].

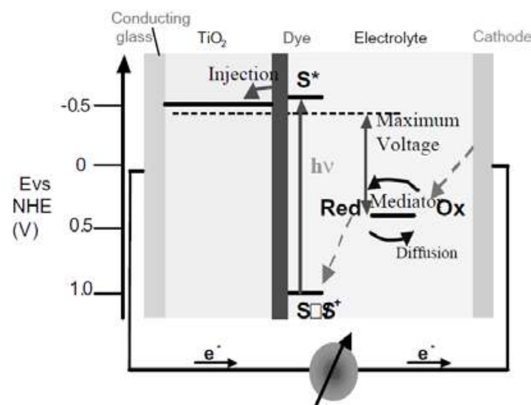

Figure 2.6: Schematic of dye sensitized solar cell containing dye deposited on TiO2, electrolyte and counter electrode[147].

The dye sensitized solar cell was invented by Michael Grätzel in 1991 by fabrication of devices based on dyes deposited on optically transparent films containing about few

nanometers TiO_2 particles. These devices gave an overall energy conversion of 7.1-7.9% [148]. Since the first demonstration of the dye sensitized solar cell in 1991, much effort has been spent by researchers and industrials to increase the efficiency and stability of dye sensitized solar cells as motivated by their low material cost, cheap fabrication and reasonably high efficiency [149-151]. Recent progress in development of dye sensitized solar cell has used other materials, such as polymer electrolytes [152-154], one dimensional photoanodes [155], carbon nanotubes [156], vegetable sensitizers [157], double oxide electrodes [158], plastic flexible substrates [159], PDOT in counter electrodes [160], graphene materials [161], nanostructured semiconductor photoelectrodes [162, 163], 3D electrodes [164-167] as strategies to boost the power conversion efficiency of dye sensitized solar cells. The currently highest efficiency of DSSCs was recorded by using porphyrin and perovskite dye as sensitizers with efficiency of 13% and 15%, respectively [168, 169].

2.4.2. Perovskite solar cells

The perovskite solar cell receives its name from that it is fabricated from materials with perovskite structure. The first working perovskite solar cell was fabricated in 2009 with an efficiency of 3.8%, similar to dye sensitized solar cells. The photoelectrode of these cells contain perovskite materials such as methyl ammonium lead bromide and methyl ammonium lead iodide. The counter electrode is generally fabricated from Pt-coated fluorine tin oxide (FTO) glass and the reduced/oxidized (red/ox) couple is made up from an organic solution of halogen and lithium halide [170]. One pressing challenge with such perovskite-based solar cells is the instability due to the corrosive materials used in the electrolyte. The stability of perovskite was improved when contacted to spiro-OMeTAD as a solid state hole transport layer [171, 172] and the efficiency was further increased by replacing TiO_2 with other scaffold materials[173]. In 2013 it was conceived that perovskite is able to transport both electrons and holes [174], and a new design without using porous scaffolds, entitled planar perovskite solar cells, was constructed [175, 176]. **Figure 2.7** illustrates two structures (sensitized and planar) designed for fabrication of perovskite solar cells.

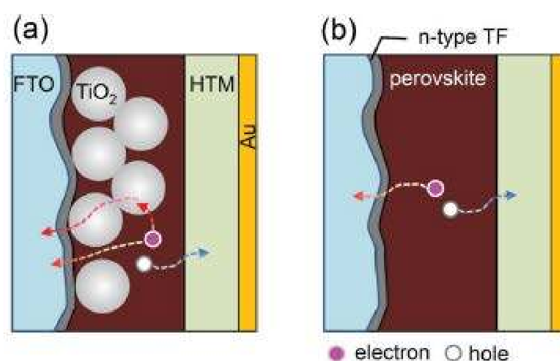

Figure 2.7: Schematic of structures considered for perovskite solar cells a) sensitized and b) planar [177]

Nowadays, researchers are trying to improve the performance of perovskite-based solar cells by using different strategies including quantum dots (QDs) as dopant [178, 179], n-type

electron transport layers [180], double electron transport layers [180], different hole transport materials like methoxydiphenylamine [181], WO_3[182] and graphene [183], one dimensional electron transport layers [184, 185] and one-dimensional TiO_2 layers such as nanowires [186] and nanotubes [187]. The highest power conversion efficiency reported for perovskite solar cells so far is about 20% that is fabricated from new perovskite materials (formamidinium lead iodide) through intermolecular exchange [188].

2.4.3. Quantum dot sensitized solar cells

In the last decade, nanotechnology that deals with the structures with size lower than 100 nm, locating between the bulk and molecule-atom levels, has been engaged in solar cell research in terms of nanoconfinement structures of different dimension:

1. Two dimensional nanostructures are the structures confined in one dimension. It means that carriers can no move in the confined direction. Thin films and quantum wells are examples of such structures.
2. In one dimensional structures, carriers can move in only one direction such as in quantum wires and quantum rods.
3. In zero dimensional structures, there is no freedom for carries to move at all. It means carriers are confined in all directions, like in quantum dots.

2.4.3.1. Quantum dots

A quantum dot (QD) is a zero dimensional nanostructure with an electron-hole exciton that is confined in three dimension with properties that can be both bulk-like and molecule-like [189]. The discovery of QDs is attributed to Ekimov and Onushchenki who in 1980 measured the absorption spectrum of microscopic CuCl nanocrystals grown on dielectric glass[190, 191]. The results related to this experiment were published in 1981[192]. The first attempt referring to colloidal QDs was made back in 1982 when Brus observed luminescence from a colloidal CdS solution while irradiating with energy above the CdS bandgap[193].

2.4.3.2. Categories of quantum dots

QDs with solar cell relevance can be categorized into single core, type I core-shell, type II core-shell, core/multi shell and alloyed QDs in terms of type and composition of structure.

2.4.3.2.1. Type I core-shell quantum dots

Single core or binary QDs are fabricated from elements in groups II-VI, IV or III- V such as CdS, Zns, GeSn, and GaAs. If the core semiconductor is surrounded by another semiconductor as a shell, a core-shell nanostructure or quantum dot is formed. Core-shell QDs are divided into two types depending on their bandgap and relative alignment of the conduction and valence bands. In type I, a wide band gap semiconductor covers another narrow band gap semiconductor. It means that the conduction and valence bands of the shell are higher and lower than that of the core, respectively. In this way excited electrons and holes are confined in

the core and the band gap of the core is an indicator of the band gap of this nanostructure band. **Figure 2.8 a** shows the scheme of band alignment in type I core-shell nanostructures.

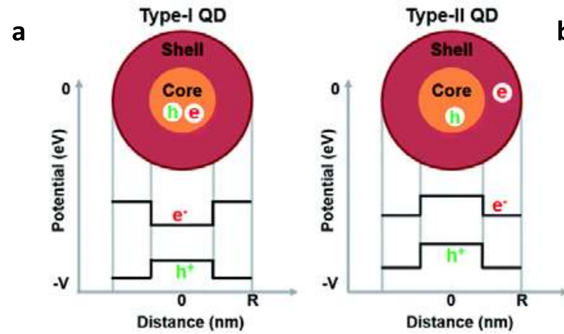

Figure 2.8: Band alignment in A) type I and B) type II core/shell quantum dot[194].

In type I the shell is used for passivation of the core semiconductor for improvement of the optical properties of the core. In this way the optically active surface of the core is separated from oxygen and water molecules, resulting in an increase in optical stability and optical properties[195, 196]. CdSe/ZnSe[197-201], CdS/ZnS[202-204] and InP/ZnS[205-209], CdSe/ZnS[210-214], ZnSe/ZnS[215-219] are examples of type I core-shell QDs.

2.4.3.2.2. Type II core-shell quantum dots

In type II core-shell, similar to type I, the core is surrounded by another semiconductor but with a band alignment that is different (shown in **Figure 2.8 b**). Now the conduction and valence bands of the shell are lower than that of the core so that the excited electron and hole are confined in the shell and core, respectively. Consequently, the difference between the bandgap of the core and shell is indicator of the core-shell nanostructure band gap which is smaller than the core and shell band gap. This smaller band gap causes broadening in the absorption compared to that of core and shell. Therefore the absorption and emission can be tuned by core and shell thickness, resulting in blue or red shift. It is notable that this emission and absorption can't be obtained by the core or shell alone[195, 196]. On the other hand, the special carrier separation in type II core-shell leads to a suppression of the recombination process and an increased luminescence lifetime. This long lifetime provides an excellent opportunity for utilization in solar cells. CdSe/CdS[220, 221], TiO_2/CdS[222, 223], CdSe/ZnSe[199, 224], CdTe/CdSe[225-228], CdTe/CdS[229-232], CdSe/ZnTe[233, 234], ZnTe/CdSe[235, 236], CdS/CdSe[237, 238], CdS/ZnSe-[224, 239], and ZnSe/CdS[198, 240] are examples of type II core/shell quantum dots.

2.4.3.2.3. Core/ multi shell quantum dots

These types of quantum dots are composed of one semiconductor core surrounded by two or more shells of semiconductor materials. Depending on the band alignments and band offsets (position of the valence and conduction bands), it can be type I or type II. The main idea for this type of QD is that each layer will have special optical and electrical properties in terms of

thickness and can be used as absorber or emitter. The former is promising for QD solar cells [241] and the latter is suitable for lightning and lasers[242]. CdSe/CdZnS/ZnS[243], ZnO/CdS/CdSe[241], CdSe/CdS/ZnS[242], CdTe/CdS/-ZnS[244], ZnSe/ZnS/CdS[245], CdTe/ZnCdTe/ZnTe[246], CdTeSeZnSe-/ZnS[247] and ZnS/InP/ZnSe[248] are examples of core/multi shell QDs.

2.4.3.2.4. Alloyed quantum dots

If three or more elements are employed to fabricate the quantum dots, we call them “alloyed” quantum dots. The possibility to tune the performance by composition is of key importance for this type of quantum dots, and is something that has attracted attention in recent years[249]. It means that the band gap and consequently the electronic and optical properties can be affected by type and composition content. In addition, alloyed QDs offer the possibility of changing the band gap without changing the size of the QDs. In several cases they show better optical and photovoltaic properties compared to binary QDs[250]. CdZnTe[251], CdSeTe[252, 253], CdSSe[250, 254], InPZnS[255], CdSeTeS[249, 256], CdHgTe[257], ZnCdSeS-[258, 259] are examples of ternary and quaternary alloyed quantum dots.

2.4.3.3. Advantages of quantum dots as sensitizers in solar cells

QDs have some benefits which have rendered interest in their use in solar cells in recent years. The high extinction coefficient which is promising for reducing dark current and enhancing power conversion efficiency is one such advantage[260]. Low cost materials, easy production, photostability, are other advantages of using QDs[261]. Theoretical analysis indicates that the efficiency of QDs can reach 44% due to the multiple exciton generation (MEG) process [262, 263]. These advantages make QD sensitized solar cells capable in principle to obtain higher efficiency than molecular DSSCs. Size-dependent optical properties and multiple exciton generation as two most important advantages of QDs are explained in the next sections.

2.4.3.3.1. Multiple exciton generation effect

The solar spectrum covers energies from UV to infrared corresponding to 0.5 to 3.5 eV energy. The basic limitation of solar cell efficiency is that the energy of photons having higher energy than the band gap energy of the semiconductor is lost through scattering processes. A few approaches have been applied to reduce this loss of energy: multiple p-n junctions and utilization of hot carriers before relaxation. The latter can be achieved in two ways; one way is to produce enhanced photovoltage and another way is to produce enhanced photocurrent. The former needs carriers to be extracted before relaxation, while the latter needs high energetic carriers to produce two or more electron-hole pairs through impact ionization. This phenomenon, called multiple exciton generation (schematically shown in **Figure 2.9**) is the inverse of an Auger process in which two electron-hole pairs are recombined to produce one energetic photon.

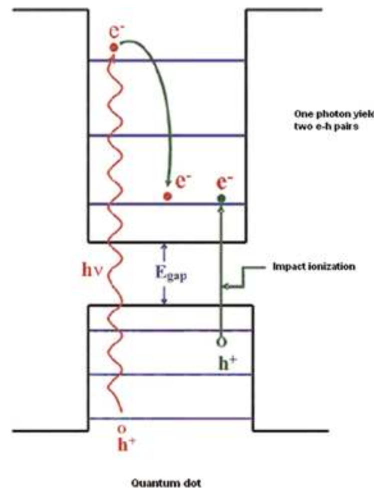

Fig 2.9: Multiple exciton generation process in a quantum dot: one photon generates two electron-hole pairs through impact ionization[264].

In fact, multiple exciton generation is a phenomenon in which more than one electron in the valence band is excited and transited to the conduction band while absorbing one photon [265]. It has been widely investigated and employed for improvement of third generation solar cell efficiency [266-272]. One of the main configurations considered for utilization of the MEG effect in QD-based solar cells is to attach the QDs into a wide band gap porous semiconductor like TiO_2 (shown in **Figure 2.10**)[265]. In this way, engineering of the carriers generated from MEG can make the efficiency exceed 44% as based on theoretical calculations [262, 263].

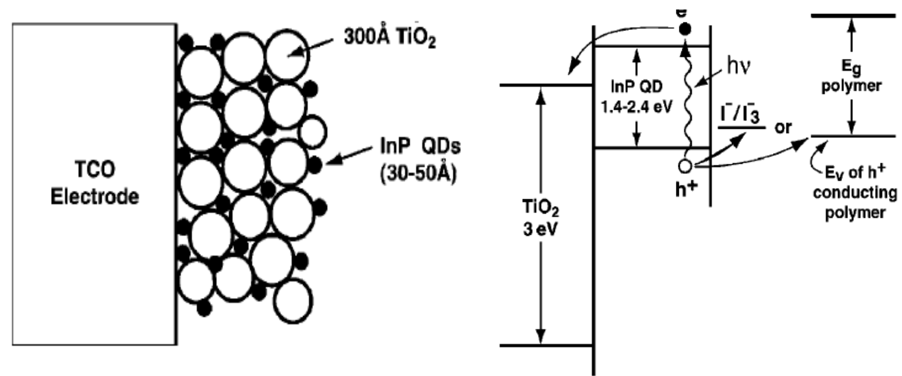

Figure 2.10: Configuration considered for utilization of MEG in quantum dot-based solar cells [265].

2.4.3.3.2. Size-dependent properties

Another important effect which makes QDs interesting in new technologies, particularly in solar cell technology, is the size-dependent effect. This effect means that the properties of the QDs is different from bulk, and depends strongly on the size. For example, optical properties of QDs, with key importance for solar cell applications, can be tuned because of the size dependence of the band gap. The size-dependent properties of QDs are due to quantum

confinement occurring when the size of the QDs is comparable to the extension, or Bohr radius, of excitons [273, 274]. The relationship between QD size and band gap is well established theoretically [275-278] and experimentally [279-287]. In terms of optical properties, the absorption edge position and emission peak are moved to longer or shorter wavelength, when the size of QDs is changed. It means that the smaller the QD the more blue shift and the bigger the QD the more red shift in both emission and absorption[288]. This means that QDs are band gap tunable which makes them very useful as sensitizers in sensitized solar cells [287]. **Figure 2.11** illustrates the effect of size of CdSe QDs on absorption edge and fluorescence peak wavelengths.

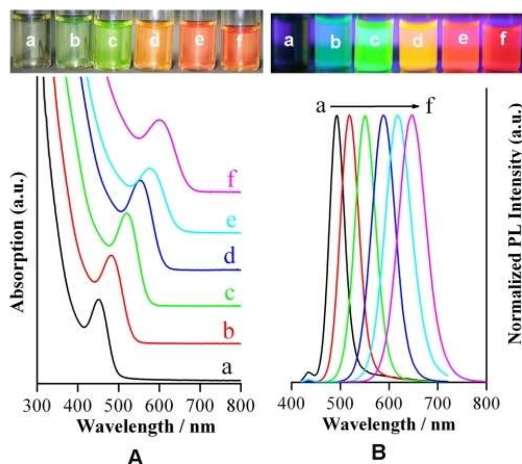

Figure 2.11: Absorption and photoluminescence of CdSe quantum dots with different size [289].

2.4.3.4. Basic principles of QD sensitized solar cells

Among different types of third generation solar cell technologies, QD sensitized solar cells have attracted a large interest due to their versatile optical and electrical characteristics [290-292]. QDs used as sensitizer solar cells not only have similar function as dyes in such solar cells but have also benefits such as size-dependent optical properties, large quantum efficiency due to multiple exciton generation and better junction formation, as already commented [293]. QDs can harvest the excess of energy as additional carriers by the multiple exciton generation[267] which can be useful in solar cells where more electron-hole pairs with proper band alignment is needed to increase the power conversion efficiency. The physical structure and operation principles of quantum dot sensitized solar cells (QDSSCs) are very similar to DSSCs [261]. In the configuration illustrated in **Figure 2.12** the oxide porous nanocrystals with wide band gap semiconductors such as TiO_2, ZnO are sensitized by the QDs. Two methods are used and analyzed in this thesis for the attachment of QDs onto the porous nanocrystals, namely the methods of successive ionic layer adsorption and reaction (SILAR) and the method of using pre-synthesized QDs attached onto porous nanocrystals by bi-linkers [294]. Yet another approach is to combine the pre-synthesized bi-linker QDs and the direct formation of QDs by the SILAR method[295].

Under illumination by light, the QDs linked to TiO_2 are excited and generate electron-hole pairs localized in the conduction and valence bands. Electrons located in the conduction band of the QDs are injected into the conduction band of the porous nanocrystal, which causes the QDs to oxidize. The QDs are then refreshed by receiving electrons from the electrolyte and the electrolyte gets reduced by electrons from the counter electrode. This process repeats to make the current flow in the circuit[296].

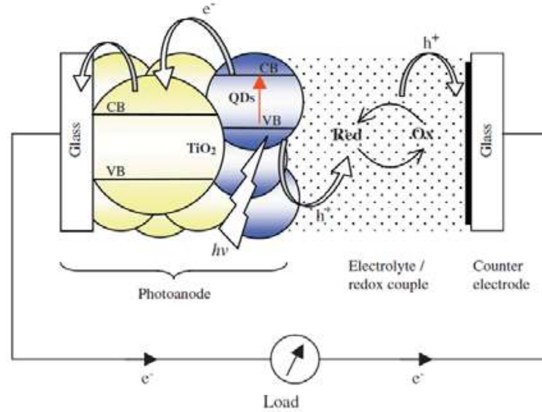

Figure 2.12: Basic configuration of quantum dot sensitized solar cells [261].

The efficiency of a solar cell can be estimated from the following equations [297, 298]:

$$\eta = \frac{J_m \times V_m}{P} \tag{2.1}$$

$$\eta = \frac{J_{sc} \times V_{oc} \times FF}{P} \times 100 \tag{2.2}$$

where P, J_m and V_m are power density, current and voltage at the operating point, respectively. J_{sc}, V_{oc} and FF represent short circuit current, open circuit voltage and fill factor, respectively. The photocurrent response to incident light can be measured from the incident photon to current efficiency (IPCE) which is estimated from[299]:

$$IPCE(\lambda) = LHE(\lambda)\eta_{coll}\phi_{inj} \tag{2.3}$$

$$IPCE(\lambda) = \frac{1240 \times J_{sc}}{\lambda \times I_{inc}} \times 100 \tag{2.4}$$

where, I_{inc}, ϕ_{inj}, η_{coll} are the power of incident light, the quantum yield and the electron collection efficiency, respectively. $LHE(\lambda)$ is the light harvesting efficiency in terms of the wavelength of incident light obtained from:

$$LHE(\lambda) = 1 - 10^{-Abs(\lambda)} \quad (2.5)$$

J_{sc} can be obtained by integrating IPCE, electron charge (q) and the density of incident photon flux($f(\lambda)$) in terms of wavelength of incident light as follows[298]:

$$J_{sc} = \int qf(\lambda)IPCE(\lambda)d\lambda \quad (2.6)$$

The absorbed photon to current efficiency can be obtained from[300]:

$$APCE(\lambda) = \frac{IPCE(\lambda)}{1 - 10^{-Abs(\lambda)}} \quad (2.7)$$

Since the light harvesting efficiency is related to the amount of QDs loaded into the TiO_2 matrix, the APCE obtained from real absorption of the QDs loaded in the TiO_2 matrix is a more precise way to explain the electron transfer efficacy which can not be exactly explained by the IPCE.

2.4.3.5. Overview of QDs sensitized solar cells

The utilization of pre-synthesized quantum dots as sensitizers in solar cells dates back to 1998[301] when InP QDs were pre-synthesized by a colloidal chemistry method and then attached into a TiO_2 matrix. In 2004, Ag-doped ZnO was used to improve the efficiency of DSSSCs[302] and CdS QDs self-assembled on TiO_2 were successfully employed as sensitizers in solar cells[303]. After 2004, much research has focused on QD sensitized solar cells. **Fig 2.13** illustrates the number of articles published in each year starting from 2004. The fast growth of papers published per year is a good evidence of the importance of QDSSCs as promising alternatives in photovoltaic technology.

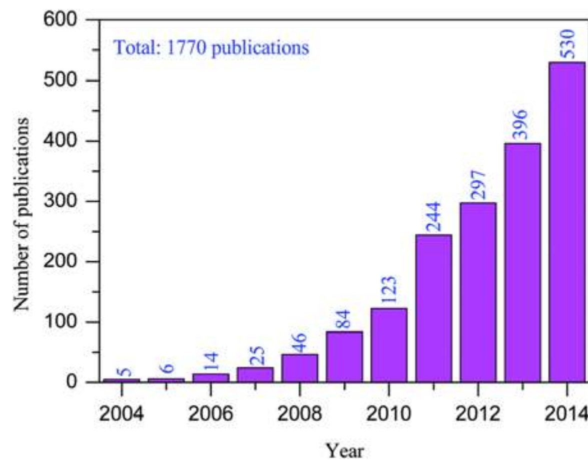

Figure 2.13: The number of publications per year for research related to quantum dots sensitized solar cells[304].

Most of the materials used as sensitizers for QDSSCs reported in papers published since 2004 are based on heavy metals such as Cd, Pb and Hg. The maximum efficiency which has been achieved until now refers to colloidal PbS-based [305] and CdSeTe-based QDs[306]. While, the high quantum yield is a positive aspect for these materials they are also highly toxic which is of environmental concern and restricts commercialization.

$CuInS_2$ are low toxic QDs and provide an alternative to Cd and Pb-based QDs. They have recently been employed to boost the efficiency of not only dye-based [307] and perovskite solar cells [179] but also QDs-based solar cells[308]. ZnSe and ZnS shell coating has been used as a strategy to enhance the efficiency of $CuInS_2$ QDSSCs [309, 310]. In this work, type II Mn-doped ZnSe/CdS QDs are investigated as Cd-based QDSSCs and colloidal InP-ZnS and Cu_2GeS_3-InP QDs as low toxic Cd-free and Pb-free QDSSCs. Furthermore, ZnS-coating and hybrid passivation are tested for low toxic CuInS2 QDSSCs - the results are discussed in chapter 4.

CHAPTER 3

Experimental Aspects

In this part, the experimental works implemented to grow epitaxial heterostructures, to synthesize QDs and to fabricate devices are described and the corresponding instruments and set ups are detailed.

3.1. Epitaxial layers

3.1.1. Materials and gas sources

Since the RPCVD technique was used to fabricate epitaxial layers, special substrates and precursors were employed. In papers I-IV a Si wafer (4 inch, p-type and n-type) was used as substrate and the gas sources listed in **Table 3.1** were employed as precursors.

Table 3.1: Gas sources, cleaning solution and carrier gas used for growth of epitaxial layers

Gas sources	Si	SiH_4, Si_2H_6, Si_3H_8
	Ge	GeH_4, Ge_2H_6
	Sn	SnD_4, $SnCl_4$
	C, P and B doping	Ch_3SiH_3, PH_3, B_2H_6
Cleaning solutions	H_2SO_4, HCl, HF	
Carrier gas	H_2	

3.1.2. Deposition technique and specifications

The reduced pressure chemical vapor deposition (RPCVD) technique was used for growth of single crystals. An Epsilon 2000 ASM working from atmospheric to 20 mtorr was used as instrument for chemical vapor deposition. This instrument is a completely automatic machine and composed of two main parts – the monitor controller and the main chamber. Gas source bottles are connected into the main chamber by a narrow pipe and the flow of each gas can be controlled from the monitor controller. Si wafers are loaded into the main chamber and delivered to the delivery box by a mechanical arm. **Figure 3.1** shows (A) Monitor controller, (B) main chamber in which Si wafer is put on reaction plate, (C) connection part between main chamber and delivery part, and (D) delivery part of Epsilon. The reaction plate temperature is controlled for heating the Si wafer during reaction.

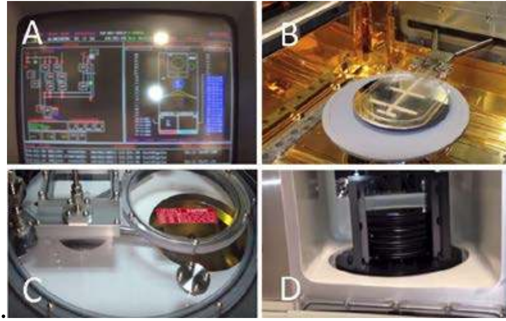

Figure 3.1: Main parts of Epsilon 2000 ASM; A) monitor controller, B) main chamber, C) connection part which connects the main chamber to the delivery box, D) delivery box

3.1.3. Wafer cleaning

Since contamination can affect the device reliability and circuit performance, the fabrication process needs a place which is as contamination-free as possible, thus where air, people, machines and chemicals as sources of contamination are avoided. To get this goal, all processes with Si wafer handling are performed in the cleanroom. To obtain epitaxial growth, a clean surface of a single crystal is needed. If the contamination or native oxide exists on the wafer surface, an epitaxial layer will not occur. Therefore, wafers must be cleaned before being loaded into the deposition instrument. Contamination of the Si wafers may origin from particles, organic materials, heavy metals/ions or native oxides. Since the epitaxial layers grown on Si wafers are constructed according to the Si structure, all contamination should be removed by a chemical method before epitaxy is made to be sure that a single crystal with high quality can be grown. Typically in this step, in order to clean the Si wafer before using it for epitaxy, firstly the wafers are put in a plastic wafer holder and then put in the solution batch composed of a 2:1 volume ratio of H_2SO_4/HCl under N flow typically for 5 min followed by rinsing in a deionized water (DI) bath for another 5 min. Mixing H_2SO_4 and HCl results in self-heating of the reaction solution in which the organic materials are oxidized and heavy metal/ions are removed from the Si wafer. To remove oxide, the wafer is typically put in HF solution for 10 seconds followed by rinsing by DI water for another 5 min and drying in a spin dryer. At the end of this step wafers are ready to be inserted into the load box of Epsilon where vacuum and nitrogen flow prevent oxidation and contamination by particles. In order to measure the thickness of the epitaxial layer the wafers are weighed before and after deposition.

3.1.4. Epitaxy growth of tensile Ge, pure and Phosphor(Boron)-doped GeSn on Si

The wafers cleaned and loaded in the main chamber before deposition must be etched by HCl to remove the native oxide created on the surface of the wafers. The GeSn layers are then grown directly on the prepared Si substrate. First, the chamber temperature is increased to 1190 °C for 2 min under N flow by HCl to remove the layers and atoms remaining from the last deposition done in the chamber. The wafer is then loaded into the main chamber and baked at 1190 °C for 1 min and etched by HCl and cooled down to 290 °C to start growing the layer. In a typical synthesis procedure, the pressure of 20 torr and temperature of 290-380 °C are applied

in the chamber. GeSn layers were deposited directly on the Si substrate (**Figure 3.2 A**) in different temperatures - 290, 350 and 380 °C - with GeSn/Si structures.

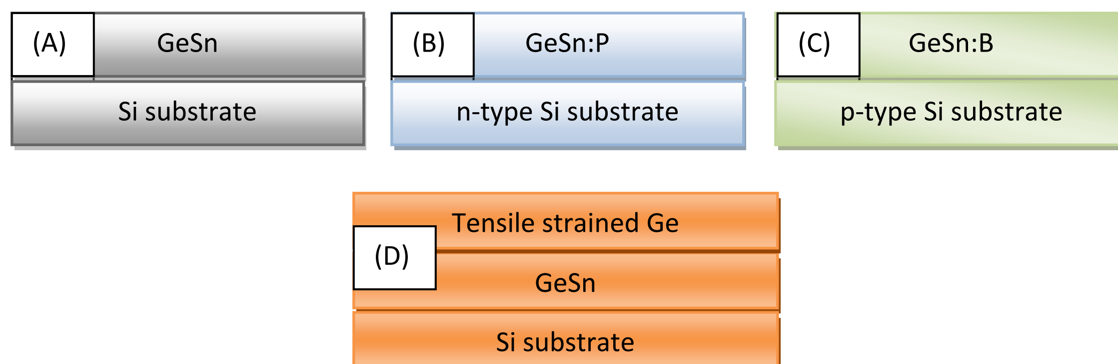

Figure 3.2: Schematic of GeSn-based structures, A) intrinsic GeSn, B) p-type GeS, C) n-type GeSn, D) tensile strained Ge deposited on GeSn.

In order to integrate the GeSn layers in the device, both boron (B) and phosphor (P) doped GeSn are needed as n-type and p-type layers. GeSn layers deposited at 290 and 350 °C are selected as best samples for n and p doping. Desired layers (Si/GeSn:P and Si/GeSn:B) are prepared by adding P or B precursors injected into the chamber to grow p-type and n-type GeSn layers (**Figure 3.2 B and C**). Data for the partial pressure applied in the system for P and B doped GeSn layers deposited at 290 and 350 °C are listed in **Tables 3.2** and **3.3**.

Table 3.2: Partial pressure of Diborane applied for n-doping GeSn layer deposited on Si

Samples	(a)	(b)	(c)	(d)	(e)	(f)
$Log_{10}(B_2H_6$ partial pressure(μ torr))	802	93	1.59	0.66	0.06	0.009

Table 3.3: Partial pressure of Phosphine applied for p-doping GeSn layer deposited on Si

Samples	(a)	(b)	(c)	(d)	(e)
$Log_{10}(PH_3$ partial pressure(μ torr))	1221	983	747	146	26

To introduce tensile strain in GeSn-based structures, the structure of Si/GeSn/Ge was also grown. Growth of this structure was like the growth of Si/GeSn layers followed by deposition of another Ge layer which is expected to be tensile strained and suitable for photonic and electronic applications (**Fig 3.2 D**).

3.1.5. Epitaxy growth of Ge, GeSnSi and GeSnSiC

To engineer the strain in GeSn, a series of GeSnSi layers, with different Si partial pressure (0, 10, and 40), and GeSnSiC layers were grown on a Ge virtual substrate (Ge layer deposited on Si substrate). In all samples, virtual Ge was deposited at 650 and 400 °C to obtain a smooth surface (**Figure 3.3**). In these samples, Si_2H_6 and CH_3SiH_3 were used as Si and C precursor, respectively.

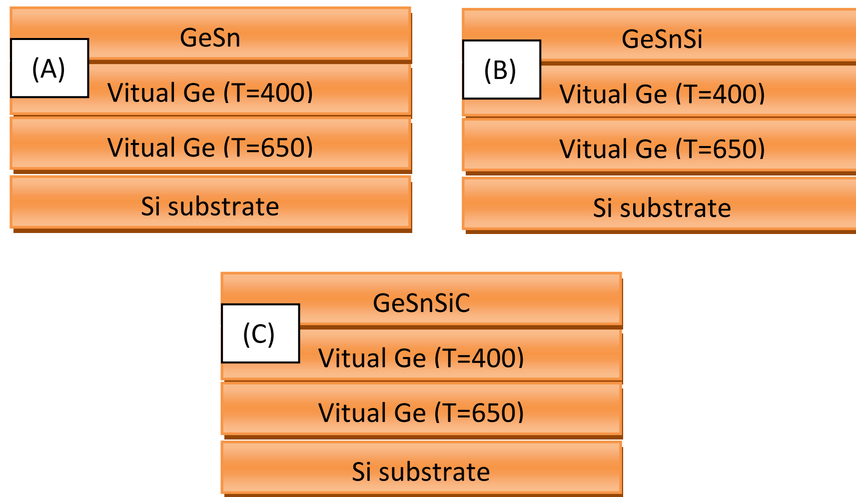

Figure 3.3: Schematic of samples containing A) GeSn, B) GeSnSi and C) GeSnSiC deposited on a virtual Ge substrate.

3.1.6. Epitaxy growth of SiGe and Ni silicidation

Silicide quality is important for the contact region of p-i-n structures and electronic devices like MOSFETs. In this thesis, the epitaxy of SiGe layers and their silicidation was also studied. The CVD technique was used for growth of these epitaxial layers and Ni was deposited on it by using a sputtering technique.

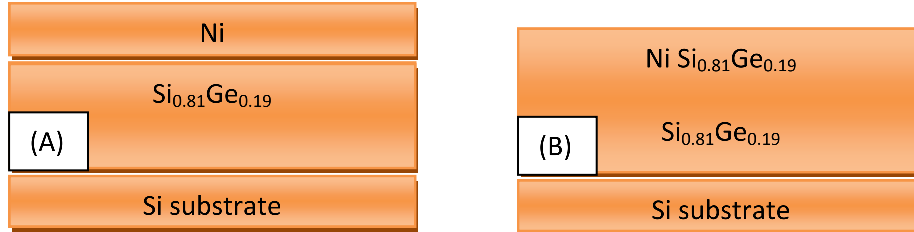

Figure 3.4: Schematic of sample containing SiGe layer, A) before and B) after annealing.

The sample is divided into two series of 2×2 cm^2 and annealed in Rapid Thermal Processing (RTA) and Microwave Annealing (MWA) systems under nitrogen flow at different temperatures (284, 315, 400, 450 and 515 °C). **Figure 3.4** shows a scheme of this sample before and after annealing and **Figure 3.5** shows the schematics of an MWA system.

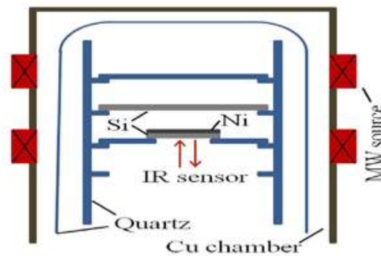

Figure 3.5: Schematic of MWA system used for silicide formation in SiGe layers (Paper IV).

3.1.7. Epitaxy growth of multi quantum wells of GeSn/Ge and Phosphor(Boron)-doped GeSn

In order to study the effect of Sn content with respect to quality and morphology of GeSn layers, multi quantum wells Ge (Vir)/$Ge_{0.98}Sn_{0.02}$/Ge/$Ge_{0.97}Sn_{0.03}$/Ge/$Ge_{0.94}Sn_{0.06}$/Ge (shown in **Figure 3.6 A**) were grown by the same method as for GeSn but with different Sn content. In addition, these GeSn layers were deposited on a Ge virtual substrate. The latter was made by growing two layers of Ge deposited at 650 and 400 °C to minimize defect density. The Sn content in the GeSn layers was changed by controlling the flow of injection from the Sn source. The deposited structure was in this case found to have three layers of GeSn with Sn concentration of 2, 4 and 6%.

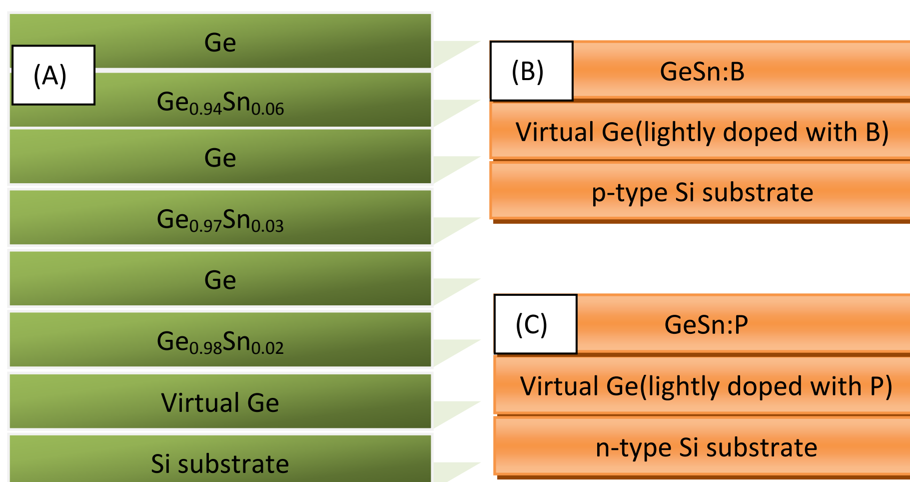

Figure 3.6: Schematic of A) GeSn/Ge quantum well with different Sn content and B)GeSn- P and C) B doped.

To examine the possibility of integrating the GeSn layers deposited on the Ge virtual substrate as p-i-n structures in the device, P and B doped variants of these layers were grown (**Fig 3.6 B and C**). The partial pressure of B_2H_6 and PH_3 are summarized in **Tables 3.4 and 3.5**, respectively.

Table 3.4: Partial pressure of Phosphine applied for p-doping GeSn layer deposited on Ge

Samples		(a)	(b)	(c)
PH_3 partial pressure (μ torr) (T=290)		1513	526	154
Samples	(a)	(b)	(c)	(d)
PH_3 partial pressure (μ torr)(T=310)	1513	592	526	154

Table 3.5: Partial pressure of Diborane applied for n-doping GeSn layer deposited on Ge

Samples	(a)	(b)	(c)	(d)
B2H6 partial pressure (μ torr)(T=290 and 310)	303	69	14.3	1.83

3.1.8. Epitaxy growth of GeSn-based p-i-n structures proposed for photonic and electronic applications

Being successful in n and p doping, two p-i-n structures Si/Ge(vir)/Ge:p/GeSi/GeSn/Ge and Si/Ge(vir)/Ge:p/GeSi/GeSn/Ge were designed to get a tensile Ge layer desired for photonic and electronic devices. **Figure 3.7** shows a schematic illustration of these p-i-n structures.

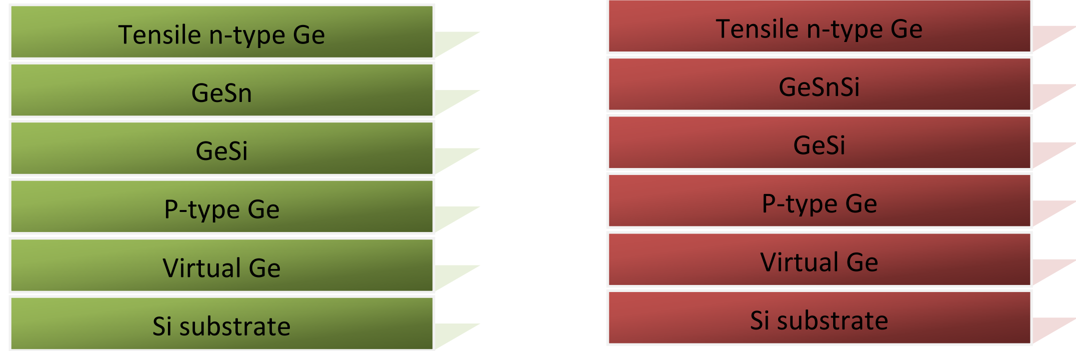

Figure 3.7: Schematic illustration of GeSn-based p-i-n hetrostructures.

3.2. Colloidal Quantum Dots

3.2.1. Materials

The hot injection technique was used to synthesize colloidal QDs. In this method, the semiconductor materials attached onto organic ligands are reacted in high temperature to yield QDs. All reactions are implemented in a three-necked flask under nitrogen or argon flow to reduce air contamination and consequently produce high quality QDs.

To synthesize ZnSe single core QDs, pure and Mn doped type II ZnSe/CdS core/shell QDs, sulfide, zinc stearate, cadmium oxide, manganese tetrahydrate and grey selenium were used as S, Zn, Cd, Mn and Se precursors, respectively. In addition, trioctylphosphine (TOP) and octadecane (ODE) were used as solvent and oleic acid (OA) and octadecylamine (ODA) were used as ligands. The synthesis of Cu_2GeS_3 single core and type II Cu_2GeS_3-InP core/shell QDs were performed by means of copper acetate, sulfur, germanium chloride, indium myristate, tris (trimethylsilyl) phosphine as Cu, S, Ge, In and P precursor, respectively. Furthermore, dodecanethiol (DDT) as activation agent and octadecane (ODE) and oleylamine(OLA) as solvents were used. In, P, Zn and S precursors, mentioned above, and 1-dodecanethiol (DDT) and ODE as activation agents and solvents were employed for synthesis of InP single core and type I InP/ZnS core/shell QDs.

3.2.2. Method and instrument

All nanocrystals (QDs) including single core, type II core/shell and type I core/shell QDs were synthesized by the hot injection method. In this method, the room temperature solution of anion precursors is injected into a hot cation solution. As illustrated in **Figure 3.8**, a cation solution containing cation precursors dissolved in solvent is put in a three-neck flask and, after

air removal by a rotary pump, it is elevated to high temperature under nitrogen or argon flow. When the temperature is high enough for reaction of anions and cations to occur, the anion solution is injected into the hot cation solution. After injection, the reaction starts and consequently the temperature is a little bit cooled down. For nanocrystal growth, the temperature is increased to higher temperature and kept so for the desired nanocrystal size.

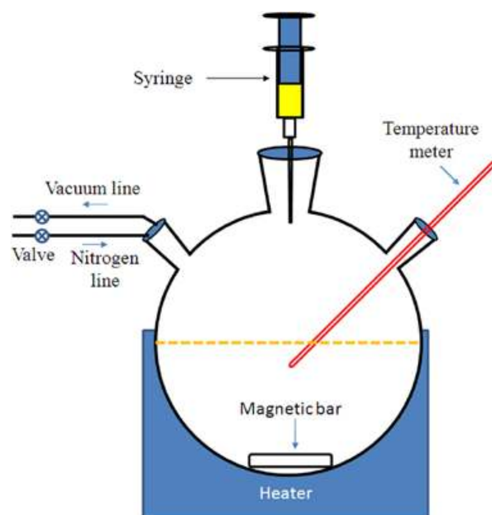

Figure 3.8: Hot injection method setup [311].

A UV-Visible spectrophotometer was used for absorption and fluorescence measurements. Inductively coupled plasma atomic emission spectroscopy (ICP-AES) and transmission electron microscopy (TEM) was employed to estimate composition content and size of the QDs, respectively. Simulator and IPCE techniques were used to evaluate the solar cell performance.

3.2.3. Synthesis of ZnSe single core QDs

In order to synthesize ZnSe single core QDs, a Zn precursor as cation solution and an Se precursor as anion solution were, respectively, prepared as follows: a specific amount of zinc stearate and stearic acid were dissolved in octadecane under pumping, stirring and heating slowly to 120°C. After a 3 times degas process, the solution was heated to 240°C under nitrogen flow to get a clear solution. Selenium (Se) dissolved in trioctylphosphine (TOP) was then swiftly injected into the Zn solution and the new solution was heated to 280°C and kept for 20 min to grow a nanocrystal with desired size. The growth process was terminated by cooling down to room temperature. The synthesized nanocrystals were precipitated by methanol and acetone and collected from centrifugation at 12krpm.

3.2.4. Synthesis of pure and Mn-doped type ll ZnSe/CdS core/shell QDs

The ZnSe core prepared in the last step and dispersed in chloroform was considered as core for ZnSe/CdS core/shell QDs. The CdS shell solution was prepared from a mixture of cadmium oxide and Sulphur (S) in ODE. To grow a shell around the ZnSe core, the CdS shell

solution was slowly injected into the ZnSe core solution and degassed and heated to 240°C under nitrogen flow. The reaction solution was further heated to 280°C to get the desired nanocrystal size and terminated after 20 min followed by cooling down to room temperature for precipitation and collection by acetone and methanol. In case of Mn-doped ZnSe/CdS QDs, the process is the same except that a specific content of Mn(0.25-3%) precursor was mixed with the Cd precursors.

3.2.5. Synthesis of Cu_2GeS_3 single core QDs

The copper precursor was prepared from mixing Cu, oleic acid, octadecane and dodecanethiol in a 25 ml flask followed by degassing below 100°C. The solution was then heated to 130°C and 180°C with injection of germanium and sulfur precursors, respectively. To grow the nanocrystals, the reaction flask was heated to 280-290°C and kept for 15 min. The reaction was terminated by cooling down to room temperature for precipitation by methanol and acetone followed by centrifugation at 12krpm.

3.2.6. Synthesis of type II Cu_2GeS_3/InP core/shell QDs

The Cu_2GeS_3 core prepared in the previous step was used as a core for the preparation of Cu_2GeS_3/InP core/shell QDs. Briefly, the mixture of In and P precursors prepared from tris(trimethylsilyl)phosphine, octadecane, indium acetate and myristic acid in glovebox under nitrogen ambient condition was injected into a Cu_2GeS_3 solution at 280-290°C. The reaction was terminated after growth of the InP shell for 15 min and cooled down to room temperature for precipitation of nanocrystals by methanol and acetone and collection by centrifugation.

3.2.7. Synthesis of InP single core and ZnS-coated InP QDs

One pot synthesis was used to fabricate ZnS-coated InP nanocrystals. Briefly, indium acetate, myristic acid, zinc stearate, 1-dodecanethiol, tris(trimethylsilyl)phosphine and octadecene were mixed in a three necked flask. After degas process, the solution was heated to 280 in 10 min and maintained in this temperature for different time to get nanocrystals with desired size. The reaction was terminated by cooling down to 60 followed by precipitation and nanocrystal collection by 1:10 equivalent of methanol/acetone. The synthesis of InP single core was performed by the procedure mentioned for InP-ZnS but without Zn and S precursors.

3.2.8. Photoelectrode

Two main important properties that should be considered for photoelectrodes are transparency and conductivity. To satisfy these requirements, FTO (fluorine tin oxide) glass was chosen as substrate. Before TiO_2 deposition, the FTO glass was firstly treated by soap while sonicating for 30 min. After washing by DI water, it was immersed in 2-propanol, KOH, ethanol and acetone under sonication for 30 min in each step. It was finally treated by $TiCl_4$ solution (40 min) to form a thin TiO_2 block layer. Three transparent layers and one scattering layer of TiO_2 layer were deposited by the screen printing method. The photoanode was then annealed at high temperature (500°C) in the furnace, cut to desired size and kept in a desiccator for future use.

3.2.9. Counter electrode

In a typical device, a brass sheet is chosen as counter electrode because its Fermi level matches the band alignment in the devices fabricated in this work. The brass sheet was cut to the desired size with the small hole constructed for electrolyte injection. The cleaning process includes sanding by sand paper and washing by soap followed by DI water rinsing. To remove possible oxide layers formed on the surface, it was immersed in HCl solution for 10 min followed by washing by ethanol. Fabrication of the counter electrode was ended by formation of Cu_2S on the surface via reaction of pure Cu and electrolyte solution containing sulfur.

3.2.10. Electrolyte

The selection of redox couples in electrolyte solution is generally based on band alignment in the device. Two common electrolytes used in QD sensitized solar cells are iodine and sulfide electrolytes containing S^{2-}/S_x^{2-} and I^{2-}/I_x^{2-} redox couples. In this work an S^{2-}/S_x^{2-}-based electrolyte was prepared from sulfur, potassium chloride and sodium sulfide dissolved in methanol and water.

3.2.11. QD solar cell assembly

QD sensitized solar cell devices are composed of an electrolyte solution embedded between a photoanode and a counter electrode. In this thesis work, the photoanode contains QDs attached to TiO_2 deposited onto an FTO glass substrate. There are two ways for attaching the QDs to TiO_2, one way is to immerse the photoanode in the solution containing QDs, the other way is drop casting of QDs dissolved in an organic solvent such as toluene. After the deposition of the QDs, the photoanode can be covered by another thin ZnS layer to passivate the QDs from reacting with the electrolyte. The counter electrode and photoanode were stacked together by a spacer and the electrolyte was injected into the space between counter electrode and photoanode.

CHAPTER 4

Results and Discussion

4.1. GeSn and its potential for utilization in photonic detectors and MOSFETs

While Group IV materials have been widely used for electronic applications they have not been used for photonic applications to the same appreciable extent due to their indirect band gap. During the last few years, however, attempts have been made to utilize Group IV materials for photonic applications [312-314] and they have been theoretically investigated and experimentally examined in order to integrate them for both photonic and electronic applications using CMOS technology. In this way, they may be used for data processing and communication in electronic and photonic devices. Among Group IV materials, Ge is promising for achieving such a goal due to its band gap that can be tailored to communication wavelengths by introducing strain. For example, tensile strain can decrease the band gap through shifting down the Γ band for detecting or emitting the light[315]. Another approach for photonic utilization in Group IV is to alloy Ge with Sn to get a direct bandgap. Tensile strained Ge deposited on GeSn thus offers a direct bandgap for detecting and emitting the light as well as high mobility and compressive strained GeSn deposited on Ge can be used as stressors in Ge-based MOSFETs. To achieve such goals, MBE was first applied many years ago [316, 317], later on CVD was employed with cheap, commercially available and stable Sn gas sources. In this work, Ge-based structures in different conditions deposited on Si and virtual Ge substrates were prepared and developed for utilization in channel MOSFETs and photonic detectors in CMOS devices. This goal can be obtained through manipulating the electrical and optical properties of the epitaxial layer by strain engineering. Since the lattice constant of Group IV materials is increased from C to Sn, the type and amount of the strain in the epitaxial layers is defined by the substrate or virtual substrate type and layer compositions.

4.2. Strain relaxed layers and their utilization to produce tensile strain for photonic detectors and MOSFETs

In paper I, intrinsic and doped GeSn layers were deposited directly on Si substrates at different temperatures (290-380 °C). In this case, a strain-relaxed epitaxial layer is expected due to the very large mismatch between the lattice constant of substrate and layer. GeSn/Ge multi-structures grown on Si substrates were considered in order to obtain tensile strain in the

Ge top layer to improve performance in high performance channel MOSFETs or p-i-n for photonic detectors. The mobility in the MOSFET and the responsivity of the detector can be tailored by the amount of strain and composition which defines the band gap of the layer.

4.2.1. HRRLMs of GeSn grown on Si substrates

In paper I, all samples were measured structurally by the High Resolution Reciprocal Lattice Maps (HRRLMs) technique (the experimental details were discussed above in chapter 3). The surface morphology and the dopant concentration of the intrinsic layer and sheet resistance of the doped layers were evaluated by High Resolution Scanning Electron Microscopy (HRSEM) equipped with Energy Dispersive Spectroscopy (EDS) and Four-Point-Probe (FPP), respectively. The Sn content in the epilayers was evaluated by both Rutherford Backscattering Spectroscopy (RBS) and the HRRLM technique. As illustrated in **Figure 4.1**, ω-2θ scan HRRLMs of GeSn layers deposited on a Si substrate with different temperature around the (113) reflection, demonstrates intensity of two peaks which belong to Si and GeSn (ω and 2θ refer to the incident and reflected beam, respectively).

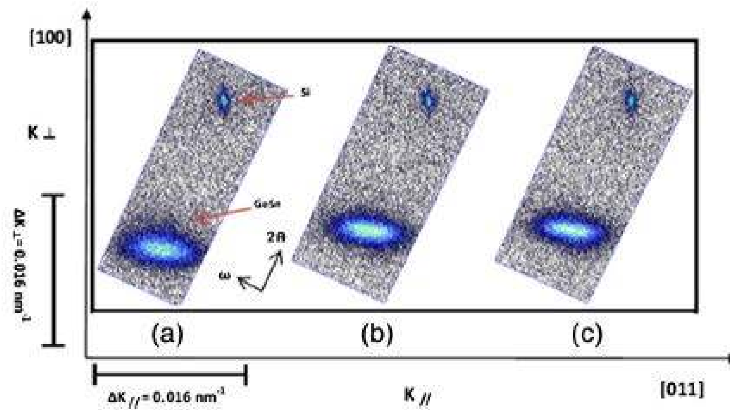

Figure 4.1: HRRLMs of GeSn deposited on si substrate at different temperature [318].

The broadened peak in the ω direction is an indicator of a successfully grown GeSn layer and confirms the presence of defects in the GeSn layer. It is attributed to a large mismatch between the lattice constants of layer and substrate. As understood from the figure, the defect density is almost the same for all samples.

4.2.2. Estimation of Sn content from HRRLMs and RBS in GeSn layers

In order to estimate the Sn content in the layer, lattice mismatch parameters are needed. The position of the GeSn layer and the Si substrate in the reciprocal (K) space can give an estimate of the lattice mismatch parameter in the perpendicular and parallel directions to the substrate surface as can be calculated from the equation:

$$f = (f_{\perp} - f_{||})\frac{1-\upsilon}{1+\upsilon} + f_{||} \tag{4.1}$$

where ν is the Poisson ratio of GeSn, which can be obtained from the equation[319]:

$$\upsilon = C_{12} / (C_{11} + C_{12}) \quad (4.2)$$

The elastic parameters of Ge and Sn summarized in **Table 4.1**[320, 321] are used to calculate $C_{ij}(GeSn)$ as:

$$C_{ij}(GeSn) = (1-x)C_{ij}(Ge) + xC_{ij}(Sn) \quad (4.3)$$

Table 4.1: Elastic constant of Group IV materials [320, 321]

Elastic constant	Ge	Sn	Si
C11 (GPa)	132	69	167
C12 (GPa)	49.4	29	65

The Poisson ratio and lattice constant of GeSn obtained from above equation are used to finally calculate the composition of Sn from:

$$a_{GeSn}(x) = a_{Sn}x + \theta_{SnGe}x(1-x) + a_{Ge}(1-x) \quad (4.4)$$

where θ_{SnGe} is 0.166 for Ge[322]. **Table 4.2** shows a comparison of Sn content obtained from HRRLMs and RBS. As understood, the HRRLM technique is a precise method to calculate the composition content of an epitaxial layer.

Table 4.2: Sn content obtained from HRRLMs and RBS for a GeSn layer grown at different temperature [318]

Growth temperature(°C)	HRRLMs (%)	RBS (%)
290	2.61	2.7
320	0.97	1
350	1.55	1.5
380	1	0.92

4.2.3. Morphology characteristics of GeSn/Si systems measured by SEM

Since growth GeSn layers are developed in the present work forutilization as hetrostructures in devices, a surface morphology measurement of the layers is necessary because of device performance. To accomplish this, the surface morphology of these layers was measured by HRSEM (**Figure 4.2**). As seen in this figure, the surface quality of the GeSn layer is affected by changing the growth temperature. The lower growth temperature (290°C) results in a smooth surface, while the higher temperatures (350 and 380°C) lead to rougher surfaces. The roughness of the surface of the samples grown at the higher temperatures (350 and 380°C) is due to Sn segregation which generates some Sn dots on the surface. The original reason for Sn segregation is attributed to excess of Sn content on the substrate in the chamber. On the other hand, the large size of the Sn spots (larger than the Ge spots) and the low solid solubility of Sn in the Ge matrix make the excess of Sn move upward towards the surface during growth. Based on these results, lower temperature, smaller dopant size and lower Sn gas flow can decrease Sn segregation and improve surface roughness. For example, in ternary GeSnSi or

quaternary GeSnSiC epitaxial layers, the size dependent effect for Sn segregation can be decreased due to incorporation of Si and C with small size in group IV materials. In this case, strain is compensated by controlling the Si and C content.

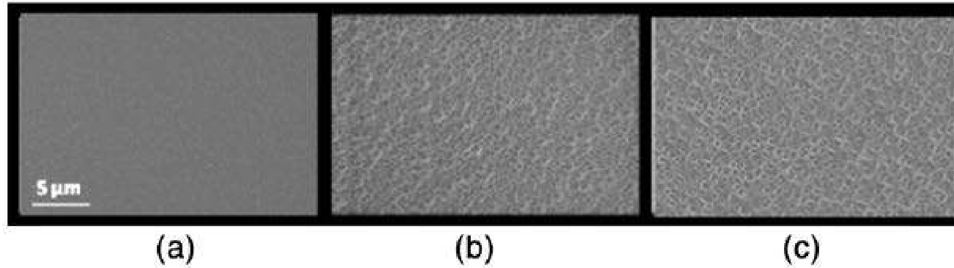

Figure 4.2: HRSEM image of GeSn samples grown at a) 290, b) 350 and c) 380°C [318].

4.2.4. Resistivity measurements of phosphor(boron)-doped GeSn/Si grown at different temperature

To utilize GeSn layers in a CMOS device, both boron and phosphor doped strain relaxed GeSn layers were synthesized at 290°C in paper I with different partial pressure mentioned in the experimental part. The resistivity vs phosphor (boron) partial pressure is shown in **Figure 4.3**. Boron doped layers at higher temperature (not shown here) did not appreciably affect the resistivity whereas a lower temperature measurement (**Fig 4.3 a**) shows a minimum resistivity of 0.95 mΩ-cm. In the case of phosphor doped layers (**Fig 4.3 b**), higher temperature means lower resistivity, which is interesting for device applications, while a high Sn segregation on the surface of these samples is a negative point that may prohibit the use of the device. In case of strained layers, both phosphor and boron doped layers show low resistivity; 0.5 and 2 mΩ-cm, respectively[323]. The low resistivity of the doped layers corresponds to a partial pressure of 0.05 and 18 µtorr for B and P, respectively, indicating that the low resistivity for B-doped layers can be obtained with 40 times smaller partial pressure than for P-doped layers. This indicates that boron can better be incorporated in the layer matrix than phosphor, which could be due to its smaller atomic size than P.

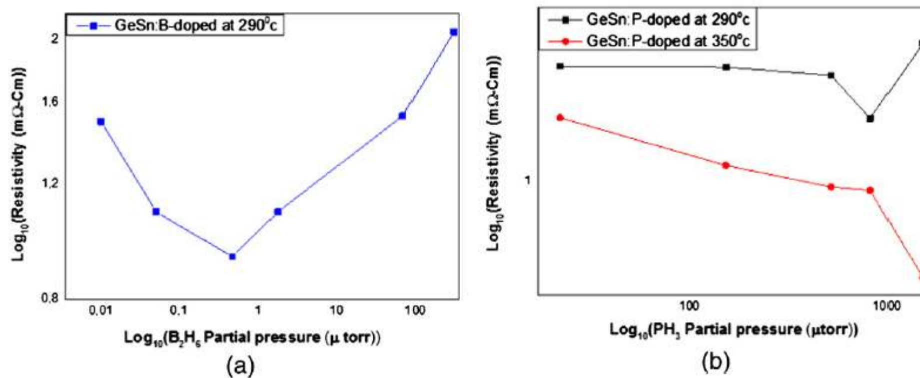

Figure 4.3: Resistivity versus a) boron and b) phosphor doped GeSn layers grown at 290and 350 °C [318].

Based on the results in this work, a compressive strain GeSn layer deposited on a Ge virtual substrate, which has better quality than relaxed GeSn, is proposed as stressor in source and drain of MOSFETs to induce tensile strain in the channels.

4.3. Compressive strain layers and their utilization to produce tensile strain for photonic detectors and MOSFETs

Although introducing Sn into a Ge matrix as a compressive layer is a difficult task due to the large mismatch, the growth of such a layer has been examined in many cases with high quality and high Sn content [323-325] which could be a way to utilize indirect-direct band gaps for photonic applications. GeSn-based layers have served for detection of light in the communication wavelength region by strain engineering in p-i-n heterostructures [326, 327]. A compressive GeSn layer can be used as a template to produce tensile strain which is promising for MOSFETs. Furthermore, it can be used as stressor in source and drain of MOSFETs to induce tensile strain in the channel.

4.3.1. TEM images of multi quantum wells of GeSn with different Sn content

In paper III, a series of GeSn/Ge multi quantum wells (MQW) were grown on virtual Ge substrates to find optimum temperature and gas flow. Virtual Ge substrates were obtained through two step growths of Ge at 600 and 400 °C, in which the defect density was decreased.

It was found that the quality of the layer was dependent on growth temperature and the defect density in the virtual layer. GeSn/Ge multi quantum wells were grown with different Sn content by $SnCl_4$ as Sn gas source. The Sn content in each well was evaluated by RBS and was obtained as 2, 3 and 6%. As illustrated in **Figure 4.4**, no visible defect was observed in any MQW (one thin layer sandwiched between another thin layer). Two thin GeSn top layers (10-30 nm) were obtained with sharp surface but where the first GeSn thick layer suffered from Sn dots segregated at the surface. It is notable that the segregation of Sn started from the first layer of epitaxy and became larger with increasing thickness.

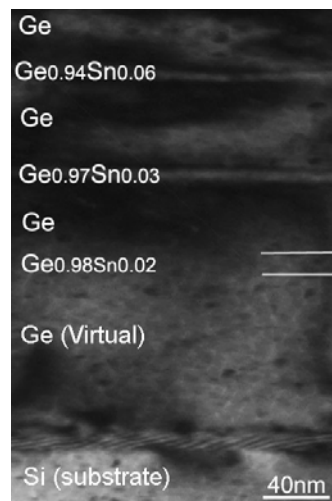

Figure 4.4: HRTEM image of multi quantum well of GeSn grown with different Sn content (2, 3 and 6%) [328].

4.3.2. Resistivity measurements of phosphor(boron)-doped GeSn/Ge grown at different temperature

In order to integrate GeSn layers in electronic or photonic devices as p-i-n structures, n-type and p-type doping at the level of 1×10^{17} - 1×10^{19} cm^{-3} is needed. A desired doped GeSn layer was developed using SnD_4 as Sn gas source[329]. Here, P and B-doped GeSn layers were grown by $SnCl_4$ at 290 and 310°C. **Figure 4.5** illustrates the effect of partial pressure of phosphor and boron on the resistivity of GeSn layer in terms of Sn content.

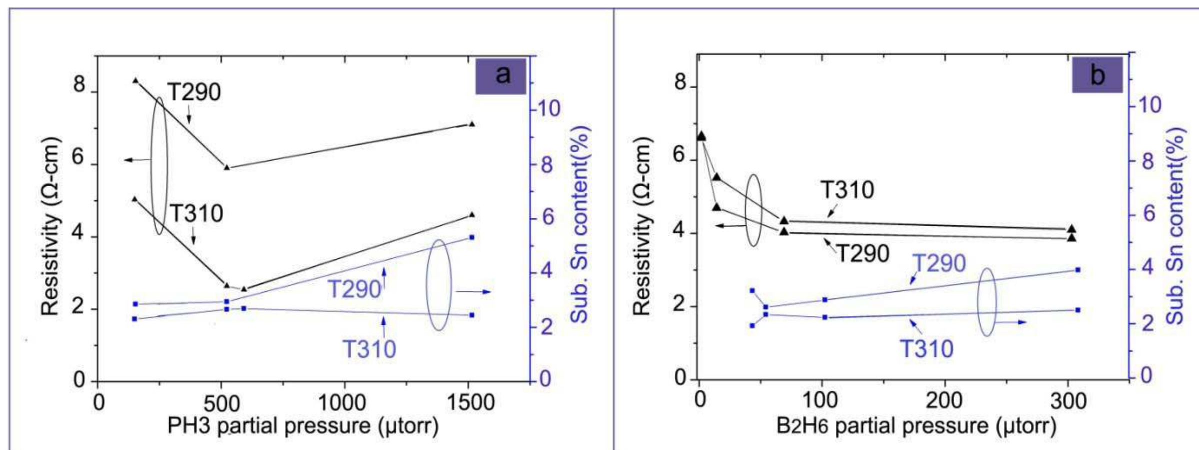

Figure 4.5: The resistivity versus partial pressure of a) phosphor and b) boron in GeSn doped layer [328].

Phosphor-doped GeSn layers prepared at higher temperature show lower resistivity resulting from higher dopant concentration (**Fig 4.5 a**). This may be due to the decrease of dopant in the presence of Sn atoms. In paper III the Sn content was increased by increasing the P partial pressure. This is evidence for strain compensation between Sn and P to minimize crystal energy.

As seen in (**Fig 4.5 b**), the resistivity curves of B-doped GeSn layers grown at higher temperature is higher than that at lower temperature, showing opposite behavior to P-doped layers (**Fig 4.5 a**). Moreover, the incorporation of B into the layer helped increasing the Sn content. The effect of temperature on the resistivity for the B-doped layer is weaker than that of the P-doped layer. The SIMS technique was used to estimate the atomic doping concentration of P and B in the layers and high concentrations of 1×10^{20} and $5\times10^{18}cm^{-3}$ for P and B were observed, respectively, which are sufficient for the n and p-type region of the p-i-n structure designed for device fabrication.

4.3.3. HRRLMs of GeSn/Ge system grown at different temperatures

In paper II, HRRLM images of GeSn layers deposited on virtual Ge at 290, 300 and 320°C were produced, these are shown in **Figure 4.6**. The GeSn peak in k space is seen to be aligned with the Ge peak and located below, indicating a compressive strain in the GeSn layer which can be used as stressor in source and drain of MOSFETs.

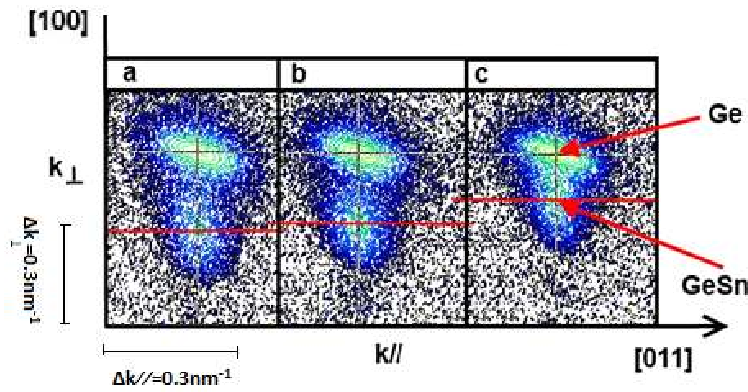

Figure 4.6: HRRLMs of GeSn/Ge/Si structures grown at different temperatures a) 290, b) 300 and c) 320 °C[330].

A minor relaxation can be seen in all samples but is more visible in sample C, showing that higher temperature causesmore relaxation which may be due to a high surface energy in the crystal. The Sn content in all samples was estimated from HRRLMs and compared with the Sn content obtained from the RBS (**Table 4.3**).

Table 4.3: The Sn content of GeSn layer obtained from HRRLMs and RBS[330]

GeSn Growth temperature(°C)	HRRLMs (%)	RBS (%)
290	3.5	3.3
300	2.5	2.5
320	1.5	1.1

4.3.4. Thermal stability of the GeSn/Ge system

Since the layers discussed above are to be used in a device, their thermal stability of the layers should be studied as this is of key importance in a high performance device. The thermal stability of the layers was investigated in paper II in terms of strain relaxation and mismatch. **Figure 4.7** illustrates the annealing temperature vs mismatch for intrinsic GeSn as well as phosphor and boron doped GeSn.

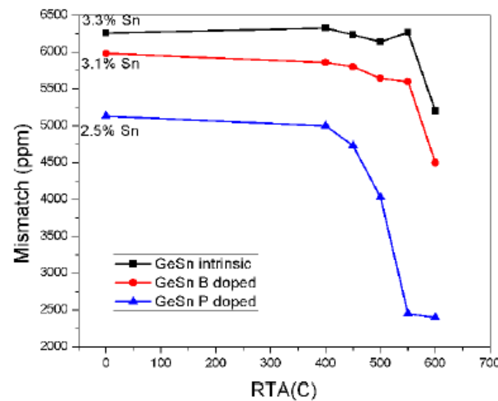

Figure 4.7: Mismatch versus annealing temperature for pure, boron and phosphor doped GeSn layer[330].

Mismatch obtained from strain in parallel and perpendicular to the growth direction and Sn content were estimated for all samples from HRRLM images. The best thermal stability refers to intrinsic and boron doped GeSn. These layers were stable up to 550 °C and afterward the large strain relaxation started. In P-doped GeSn the strain started relax in the critical temperature of 450 °C, much lower than the critical temperature for the intrinsic and boron doped layers. A similar effect was seen for the thermal stability of doped SiGe layers[331].

4.3.5. Effect of P and B on incorporation of Sn

In case of B and P doped GeSn layers, it is found that incorporation of Sn is increased with increasing dopant concentration (shown in **Figure 4.8**), strengthening the notion that incorporation of Sn atoms into the crystal is inversely proportional to the crystal energy.

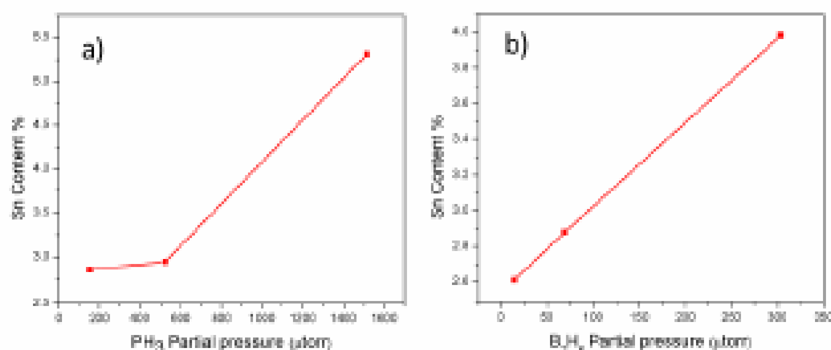

Figure 4.8: The Sn content versus a) phosphor and b) boron partial pressure[330].

It means that more Sn content could be incorporated in the crystal matrix if the crystal energy is decreased by more incorporation of small dopants.

4.3.6. Strain engineering by incorporation of C and Si in GeSn matrices

In group VI materials, GeSnSi is an interesting system due to the possibility of engineering the strain and bandgap by controlling the composition content. A tunable indirect-direct bandgap of 0.8-1.4 eV in ternary GeSnSi has opened a new window for development of electronic and photonic devices [332, 333]. The strain in this system can be tailored for the bandgap of 0.8-1.4 eV depending on the Si/Sn ratio[331]. Ternary GeSnSi having compositions with different lattice constant (5.43, 5.65 and 6.49 for Si, Ge and ∝-Sn, respectively) is here important. Theoretical calculations indicate that the tensile strain for Ge grown on GeSnSi layer can be tailored by controlling the Ge, Sn and Si content[334]. The possibility for indirect-direct band gap in the Ge matrix is another feature of GeSnSi which is in demand for photonic applications [335, 336]. In addition, totally relaxed GeSnSi/Ge can be used as virtual substrate for Ge for producing tensile Ge which is promising for detecting light in photonic detectors and for laser light emission. One way for strain engineering, used in the work of paper I, is to grow GeSnSi layers with different Si content as well as to grow GeSnSiC layers. In this case, compressive strain and strain compensation are expected for the layers by increasing Si and C content. To get this goal, GeSn(Si,C)/Ge layers were deposited on an Si

substrate at different temperature under $SnCl_4$ flow of 0.6-1.3 g/h and characterized by HRRLMs. In all samples, the thickness of the virtual Ge was made as small as possible (10nm) to prevent strain relaxation. In samples a, b and c, the partial pressure of 0, 10 and 40mtorr was chosen for Si_2H_6, respectively, and in sample d, a partial pressure of 2.5 mtorr for CH_3SiH_3 was employed (paper I).

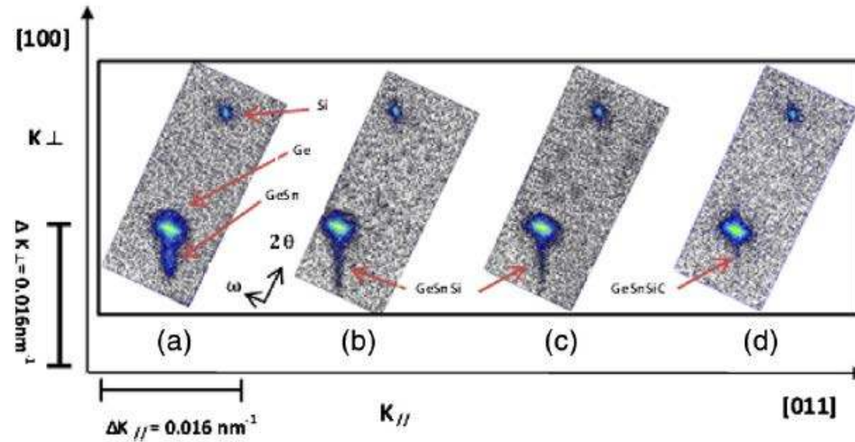

Figure 4.9: HRRLMs of GeSnSi with Si partial pressure of a) Si= 0, b) Si=10, c) Si=40mtorr and d) GeSnSiC with C partial pressure of C=2.5 mtorr[318] .

In **Figure 4.9 a-c**, the GeSn layer peak is aligned with the virtual Ge peak in K space. Since the layer peak is located at the left of the Ge peak, the layer is expected to be compressively strained. The layer peak moves toward the Ge peak by introducing more Si content. On the other hand, **Figure 4.9 d** shows that the strain was totally compensated by introducing C atoms into GeSnSi so that the layer peak is located at the Ge peak. The Sn, Si and C content in **Fig 4.9 a, c** and **d** were 3, 12 and 6%, respectively. The strain compensation in **Figure 4.9 b-d** is due to the smaller size of Si and C than Sn, which leads to a decrease of the lattice constant of the layer so that it becomes almost equal with the Ge lattice constant.

4.3.7. Effect of Si on incorporation of Sn

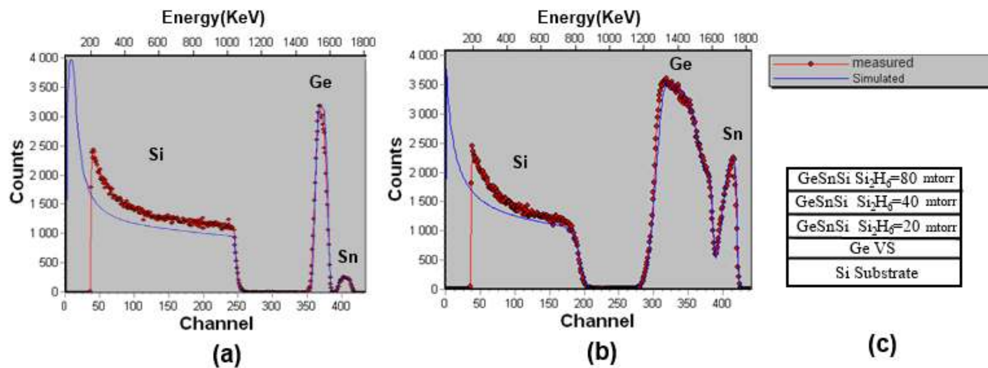

Figure 4.10: RBS spectra of a) GeSn and b) GeSnSi with gradient Si layer. c) schematic of sample b [330].

As understood from RBS spectra of GeSn and GeSnSi grown on the virtual Ge substrate (**Figure 4.10**), the Sn content shrinks from 3% in the GeSn layer to 6% in the GeSnSi layer with increase of the Si content in the layer. The Sn content versus Si partial pressure of all samples is illustrated in **Figure 4.11** which shows a continually increase for Sn content with increasing the Si partial pressure. This is attributed to strain compensation created by increasing the Si content.

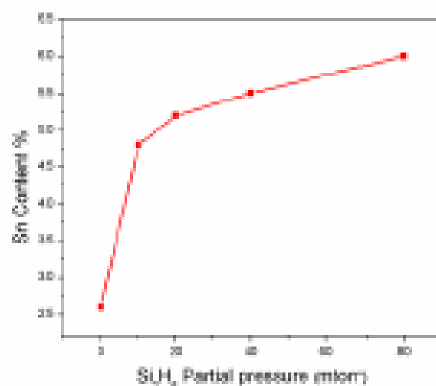

Figure 4.11: The Sn content versus Si partial pressure for GeSnSi layers grown with different Si partial pressures [330].

4.3.8. Effect of Si and C on morphology of GeSn-based layers

Since Sn was segregated on the surface of the GeSn layer, surface morphological measurement of the GeSnSi layer in presence and absence of C was studied in paper I. In these samples, Sn gas was injected into the chamber with flow of 0.6 g/h and Ge_2H_6, Si_2H_6 and Ch_3Sih_3 were employed as Ge, Si and C gas sources, respectively.

HRSEM images of samples a-c in **Figure 4.9** are shown in **Figure 4.12**, indicating the effect of introducing Si and C atoms into the GeSn layer on the surface morphology of the final layer.

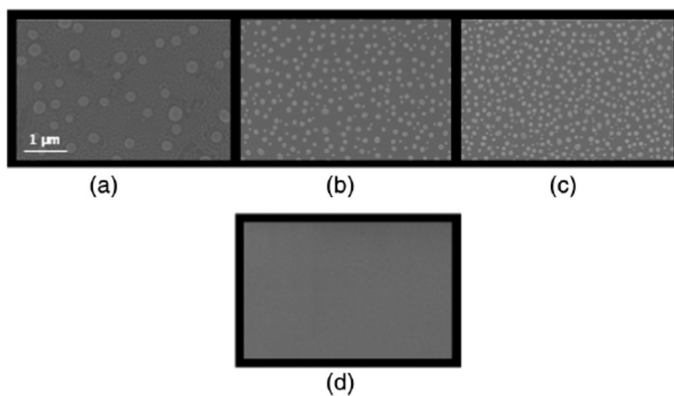

Figure 4.12: HRSEM image of GeSnSi layer grown with Si partial pressure of a) 0, b) 10, c) 40 mtorr and GeSnSiC layer with C partial pressure of 2.5 mtorr[318].

Figure 4.12a shows very big dots on top of the surface, which become smaller in **Figure 4.12b** by introducing Si. The big dots in sample (a) origin from Sn segregation due to the big size and low solid solubility. These big dots on the surface of GeSnSi (sample a) become invisible in sample d. This shows that the introduction of C atoms not only prevents Sn segregation but also helps incorporating Sn into the Ge matrix. Increasing Si content and introducing C atoms result in a completely smooth surface for sample d containing both Si and C. The same observation was earlier reported for Ge dots on SiGe layers [337, 338]. Kouvetakis et al predicted the band gap of 0.86-1.4eV for GeSnSi layers with respect to Si and Sn content incorporated in a Ge matrix where the Si source was Si_3H_8 [339]. Here, the successfully growth of GeSnSi layers by Si_2H_6 as Si gas source offers a cost-effective way for future utilization in photonics and electronics. It should also be mentioned here that the introduction of Si and C was not successful in strain-relaxed GeSn whereas it was successful for compressive strained GeSn. This confirms that strain plays an important role for introducing more Sn content, which thus is promising for electronic and photonic applications.

4.4. Tensile strain layers for photonic detectors and channel MOSFETs

4.4.1. Tensile Ge obtained from the Ge/GeSn/Si system

The results obtained so far indicate that strain relaxed GeSn layers can be used as virtual substrates to produce tensile Ge. Since the lattice constant of relaxed GeSn layers is bigger than for Ge, one can expect tensile Ge if the Ge is carefully grown on this virtual substrate. In fact, in GeSn/Ge structures relaxed GeSn plays the role of a template for growth of tensile Ge. That is a promising aspect considering the common use of indirect-direct band gap Ge-based materials in photonic detectors.

4.4.2. Tensile Ge quality measured by HRTEM

As illustrated in **Figure 4.13 a**, GeSn layers have high density of misfit and threading dislocations starting from the interface with the Si substrate and decreasing dramatically towards the Ge top layer. This indicates that the Ge top layer was grown with better quality compared to the GeSn layer. The quality of the Ge top layer is more precisely shown in **Figure 4.13 b**.

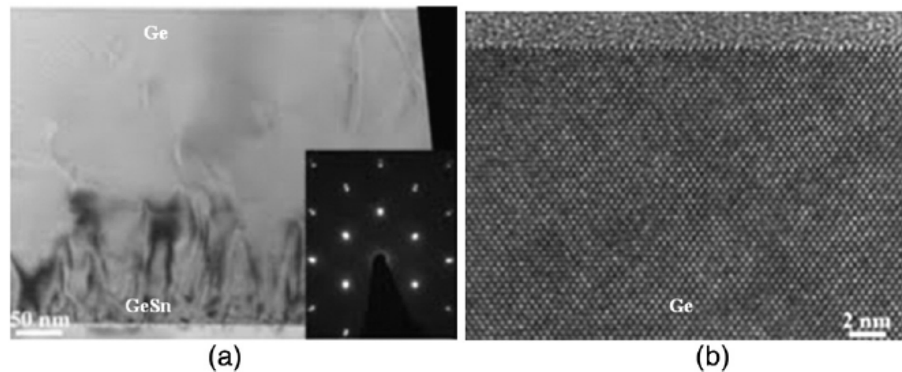

Figure 4.13: HRTEM image of a) Ge/GeSn/Si system and b) Ge top layer[318].

This result indicates that a GeSn layer deposited directly on the Si substrate is not suitable for device fabrication. It can though still be used as virtual substrate for Ge. Since GeSn will be relaxed, its crystal size is expected to be larger than that of the strained GeSn layer. This makes the Ge top layer tensily strained, which is promising for photonic detector and MOSFET applications.

4.4.3. Strain amount in tensile Ge measured by HRRLMs

In addition to layer quality, the amount of strain in the Ge top layer plays an important role for photonic detectors, where the probability of detecting the light depends on the position of the Γ-band with respect to the valence band.

As illustrated in the HRRLM image of the Si/GeSn/Ge structure in **Figure 4.14**, the Ge peak in K space is located on top of the GeSn peak, indicating tensile strain of 0.52% in the Ge layer. This strain amount corresponds to a band gap of 0.65 eV in the Ge layer and is related to the Sn content in the virtual substrate. Therefore, by strain engineering of the band gap, a tensile Ge layer can be proposed not only for detection applications where an indirect-direct band gap is promising, but also for high performance channel MOSFETs in CMOS technology where high carrier mobility tensile strain layers are needed.

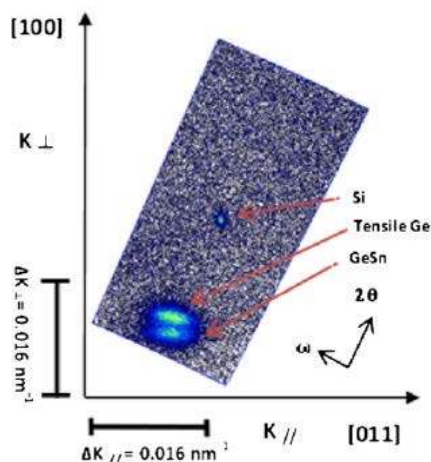

Figure 4.14: HRRLMs of GeSn/Ge/Si system[318].

4.4.4. Tensile Ge obtained from a Ge/GeSn(Si)/GeSi/Ge/Si system

Another p-i-n structure proposed (in paper III) to produce tensile Ge are multi quantum wells of GeSi/GeSn and GeSi/GeSnSi sandwiched between a virtual p-type Ge layer and an n-type Ge top layer. Since a direct band gap Ge is needed for designing Ge-based photonic detectors, the n-type Ge layer on top of these structures was heavily doped by boron to fulfill the requirement for detecting the light. In this way, the L valley in the conduction band is filled by electrons and electrons are transited from the Γ valley. These structures were analyzed by

the SIMS and HRRLM techniques to study strain and doping profiles. The boron concentration of 8×10^{19} cm^{-3} in the Ge top layer was estimated by SIMS that fulfills the requirement in the n-type region for design of p-i-n structure detectors. **Figure 4.15** shows an HRRLM image of the structures measured in (113) reflection.

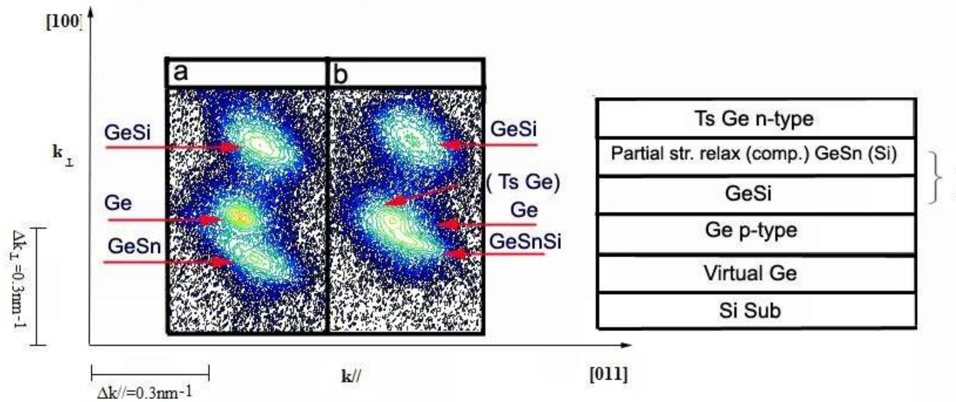

Figure 4.15: HRRLMs of a) Ge/GeSn/GeSi/Ge/Si and b) Ge/GeSnSi/GeSi/Ge/Si[328].

The Ge top layer peak in **Figure 4.15a-b** is located on top of the GeSn peak, showing tensile strain. The GeSn peak was not aligned with the Ge peak, indicating that the strain was partially relaxed so that the Ge top layer is expected to be tensile strained relating to the Si and Sn content in the GeSn(Si) layer. Indeed this was the case, with an amount of 0.45% corresponding to a band gap of 0.72 eV. Introducing Si into the GeSn matrix not only compensates the strain but also causes more incorporation of Sn into the layer. The GeSnSi peak in **Figure 4.15b** was almost located on top of the Ge peak, indicating a well-compensated strain layer in which the Si content was estimated to 12%. The ternary GeSnSi system in **Figure 4.15b** is a more interesting system than the binary GeSn system due to an increased possibility of strain and band gap engineering. In this way, not only different layers with different band gaps can be obtained in one heterostructure but also the amount of strain of the Ge top layer can be tuned by proper composition. These results propose a way to design and fabricate many different and interesting p-i-n hetrostructures as photonic detectors operating in the infrared wavelengths of 1-1.5 µm and as MOSFETs for high speed switching.

4.5. Nickel silicidation of the strained SiGe formed by RTP and MWA for source/drain of MOSFETs

After being successful in the study of strained nanostructures for utilization as MOSFETs, nickel silicidation of strained SiGe as material of choice for contact metallization in source/drain of MOSFETs was investigated in paper IV. In this process, Ni, thermally deposited on the strained layer, is annealed and the formation of strained silicide is studied. Here, a rapid thermal process (RTP), in which a halogen lamp is used for heating, is employed as the traditional process for formation of Ni silicide. Microwave annealing (MWA) was also employed as an alternative method for low temperature annealing. The effects of these two processes on silicide formation are compared.

4.5.1. Annealing strategies: challenges and alternatives

In the community of semiconductor technology there has been surge for methods alternative to the traditional annealing process that can be used in scaling down CMOS devices [340]. A low thermal budget then plays an important role where retain of the strain after the thermal process is needed for increasing the mobility[341]. This role becomes more important when strained thin layers with low resistivity and high quality are demanded for drain/source of MOSFETs [342, 343]. Laser annealing [344] with millisecond heating and microwave annealing are methods of choice. The basic challenge for laser annealing is that the absorption of photons depends strongly on the surface emissivity of the substrate [345, 346]. Microwave annealing (MWA) is a good alternative because not only is the energy then directly transferred to the substrate but also the energy transfer is not affected by the surface emissivity of the substrate[347]. The MWA process is often successful to produce homogenous contact silicide layers formed at low temperature[348].

Paper IV reports a study of silicide formed by MWA and RTP techniques in strained SiGe as motivated by their use as contacts in source/drain of MOSFETs.

4.5.2. Resistivity measurements of NiSiGe layers

For a typical sample, a 10 nm thin layer of Ni was sputter deposited on strained SiGe grown on a Si substrate, see paper IV. The sample was sliced and categorized into two groups, one for MWA and the other for the RTP process. After being annealed, all samples were measured by four point probes to evaluate the changes in sheet resistance and resistivity - the results are shown in **Figure 4.16**.

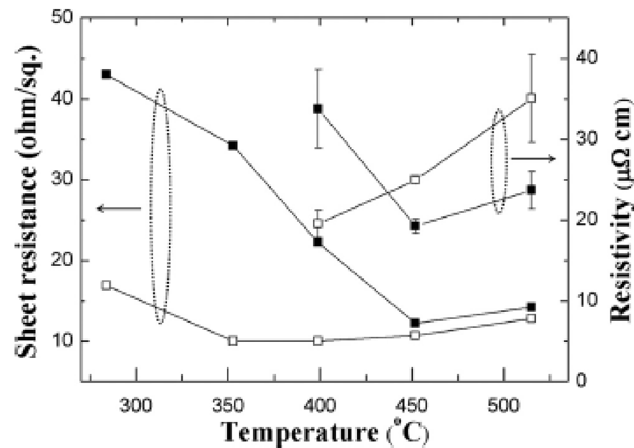

Figure 4.16: The sheet resistance and resistivity versus annealing temperature for samples annealed by MWA (black dot) and RTP (white dot)[349]

The samples annealed by the MWA technique show low resistivity formed at a lower temperature than that of RPT. According to XRD data it is found that only the NiSiGe layer is formed at 285 °C in MWA and at higher than 400 °C in RTP. This has been theoretically[350] predicted and experimentally[351, 352] confirmed.

4.5.3. Measurements of NiSiGe layers by cross-sectional TEM

Figure 4.17 illustrates a cross sectional TEM image of the samples annealed by MWA and RTP at 400 and 515 °C. Both samples annealed by MWA (**Figure 4.17 a**) and RTP (**Fig 4.17 b**) at 400 °C show uniform and continuous layers while agglomeration can be seen in the samples annealed by MWA and RTP at 500 °C (**Fig 4.17 c-d**). This agglomeration is responsible for the resistivity enhancement at higher temperature in Fig 4.16 and is due to a diffusion-out of the Ge from the NiSiGe layer[352] to minimize the surface energy of the crystal.

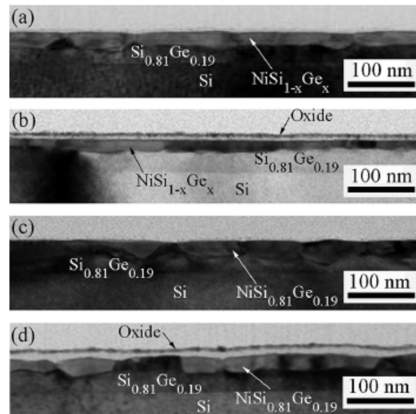

Fig 4.17: Cross section TEM image of samples annealed by a) MWA at 400, b) RTP at 400, c) MWA at 515 and d) RTP at 515°C[349].

Despite the annealing process under nitrogen flow in RTP, the thin oxide layer formed on top of the NiSiGe is observed. The formation of this oxide layer is due to the existence of air during the RTP process. Insufficient purge before and during annealing is responsible for exposing the sample to the air. The thickness of NiSiGe formed by RTP is less than that of RTP due to the consumption of SiGe to form the oxide layer.

4.5.4. Measurements of NiSiGe layer by the HRRLM technique

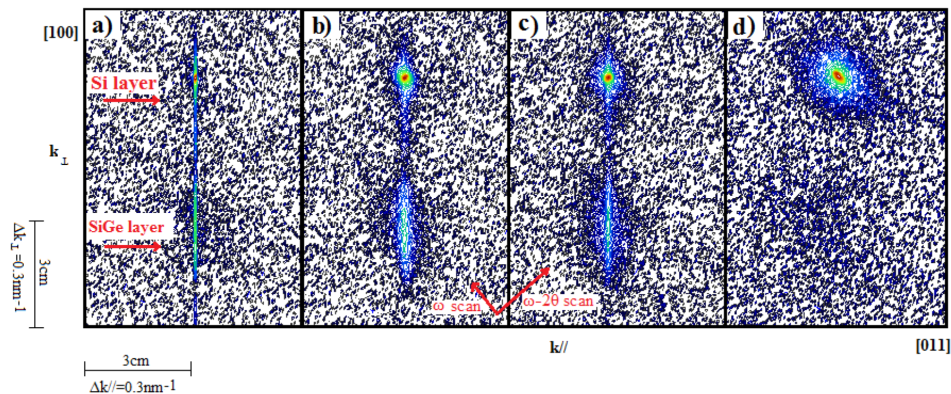

Fig 4.18: HRRLMs of samples annealed by a) MWA at 400 °C, b) RTP at 400 °C, c) MWA at 515 °C and d) RTP at 515 °C[349]

The remaining SiGe layer not reacting with Ni in the two series of samples annealed by MWA and RTP was investigated by the HRRLM technique around the (113) reflection to determine the strain relaxation and defect density. **Figure 4.18** illustrates HRRLMs of samples annealed by RTP and MWA at 284 and 515 °C. Misfit parameters both in perpendicular and parallel to the growth direction were achieved from the position of the SiGe layer peak in K space and the defect density was estimated from the peak broadness[353]. The misfit parameters summarized in **Table 4.4** was used to estimate the amount of strain relaxation.

Table 4.4: Misfit parameters of samples annealed by MWA and RTP at 284, 400 and 515°C[349]

Sample ID	F_z	$F_{x,y}$	R (%)
284 MWA	0.0119	1.66×10^{-5}	0.01
400 MWA	0.0116	1.84×10^{-5}	0.03
515 MWA	No layer peak	No layer peak	Very high relaxation
284 RTP	0.0123	Negligible	Negligible
400 RTP	0.0125	3.3	Negligible
515 RTP	0.0116	5.84×10^{-5}	0.01

The HRLMs of the sample annealed by RTP at 284 °C (**Fig 4.18 a**) shows a completely sharp SiGe layer and Si substrate peak with negligible relaxation. The broadness in the HRRLMs of the sample annealed by MWA at 284 °C (**Figure 4.18 b**) is due to defect generation and strain relaxation, which often are significant for samples annealed by RTP. **Figure 4.18 a,c** and **Fig 4.18 b,d** indicate that the defect generation and strain relaxation rate are enhanced by increasing the temperature so that the layer peak disappears in **Figure 4.18 d**, showing very high relaxation due to strong diffuse scattering. Therefore, it is understood that despite that the same temperature is applied for MWA and RTP the results are different and that the strain relaxation occurs at lower temperature for MWA compared to RTP. This means that the temperature close to the surface where silicide is formed is higher in MWA than for RTP. This behavior is compatible with CMOS technology where source/drain contacts are formed under low thermal budget and with low resistivity layers with high quality that are needed to integrate the MOSFETs in the CMOS device.

The results show that the MWA technique offers a silicide formation at lower temperature compared to traditional annealing techniques such as the illuminated-based annealing process.

4.6. Quantum dot sensitized solar cells

The research implemented for QDSSCs can be divided in two categories - toxic Cd-based and low toxic Cd-free QDSSCs. Mn-doped type II ZnSe/CdS core/shell as Cd-based and Cu_2GeS_3/InP, ZnS-coated InP and $CuInS_2$ as Cd-free QDs were employed as sensitizers in QDSSCs and investigated.

4.6.1. Cd-based quantum dot sensitized solar cells

One of the mostly used materials in QD sensitized solar cells is cadmium. Also other toxic materials are used due to special absorption and band alignment as well as high quantum yield, which are compatible for TiO_2-based substrates. For example, ZnSe single cores and type II

ZnSe/CdS core/shell QDs with different Mn concentrations as Cd-based sensitizers are employed and investigated in this thesis.

4.6.1.1. Band gap engineering, effect of Mn dopants on optical properties of QDs

In this thesis, ZnSe single cores and type II ZnSe/CdS QDs doped with different Mn concentration were successfully synthesized. After purifying by methanol and acetone, they were dispersed in toluene. The TEM image of ZnSe/CdS in **Figure 4.19** is a demonstration of successfully grown QDs.

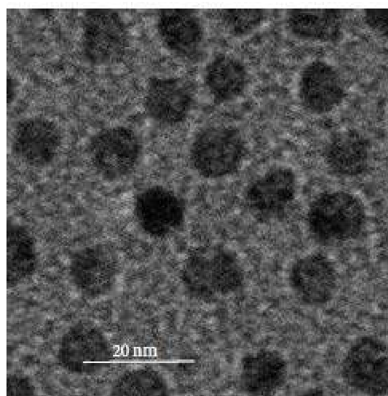

Figure 4.19: TEM image of type II ZnSe/CdS core/shell QDs [354]

All sensitizer QDs were deposited onto TiO_2 photoanodes and measured by a UV-Visible spectrophotometer. **Figure 4.20** illustrates absorption of QDs onto TiO_2 and their fluorescence when dispersed in chloroform.

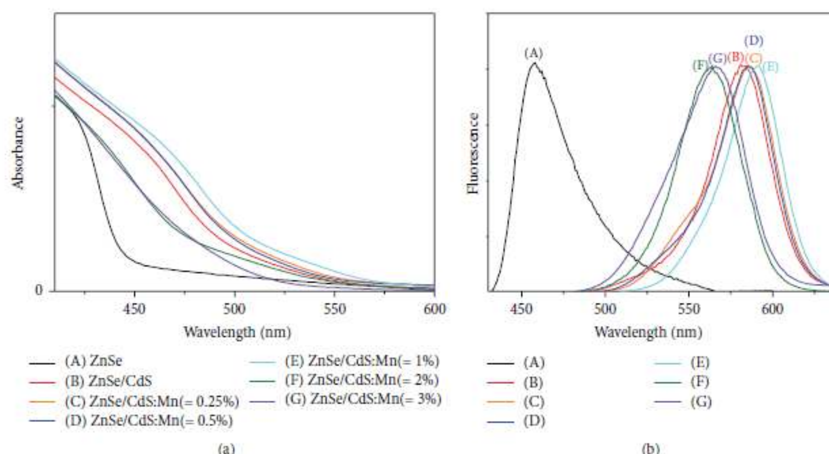

Figure 4.20: Absorption and PL spectra of ZnSe single core and ZnSe/CdS QDs doped with different Mn concentrations (0-3%) [354].

It is found that a single core ZnSe has a relatively narrow absorption while ZnSe/CdS core-shells have broader absorption. The absorption edge of ZnSe/CdS core-shells is red-shifted up

to 488 nm in wavelength compared to the absorption edge of the ZnSe single core (437 nm). A similar behavior is seen in the fluorescence peak wavelength of the ZnSe/CdS core-shell compared to the single ZnSe core or CdS shell. This behavior is due to a decrease of the band gap which is equal to the energy difference between the conduction band of the shell and the valence band of the core [239, 355]. In this way, type II core-shells show smaller band gaps which result in broader absorption. Band gaps were estimated from the absorption edge using a method explained in the literature [356, 357] with the key equation:

$$\alpha h\upsilon = k(h\upsilon - E_g)^{\frac{1}{2}} \tag{4.5}$$

where α, k and E_g are absorption coefficient, a constant and band gap energy, respectively.

The band gaps of QDs were estimated from continuing the straight line of tangent toward zero absorption coefficient for the plotted $(\alpha h\upsilon)^2$ in terms of $(h\upsilon)$ - the results are summarized in **Table 4.5**.

Table 4.5: Absorption band edge and calculated band gap of ZnSe single core and ZnSe/CdS QDs doped with different Mn concentrations (0-3%) [354]

Samples	(a)	(b)	(c)	(d)	(e)	(f)	(g)
Optical Band gap(eV)	2.81	2.52	2.48	2.49	2.44	2.61	2.59
Absorption band edge(nm)	437	488	495	493	504	471	474

Mn doping shows opposite behavior in absorption and emission peak wavelengths for low and high Mn content. Low Mn content (0.25-1%) causes red shift and higher Mn doping levels result in blue shift. This behavior is due to changes in the band gap of the QDs (**Table 4.5**). The red shift is expected due to the contribution of Mn as metal dopant and blue shift is due to the formation of another wide band gap phase like MnS. Low solid solubility of Mn($<1\%$) in CdS is the main reason for the formation of the MnS phase[358-361].

4.6.1.2. Performance assessment of devices sensitized by Mn-doped ZnSe/CdS QDs

All QDs were introduced into porous TiO_2 nanoparticles deposited on indium tin oxide conductive glass. The devices sensitized by these QDs were assembled by the method mentioned in the experimental part. In order to evaluate the performance of the devices, they were exposed to simulated solar irradiation working under 100mWcm^{-2} intensity. Device parameters are listed in **Table 4.6** and the current density-photovoltage characteristics of the devices are shown in **Figure 4.21**. The device sensitized by type II ZnSe/CdS core/shells shows a dramatic increase in current compared to a single ZnSe core. This increase is due to special carrier extraction and broad absorption of light in the type II QDs. Another issue that should be considered here is the strain induced in the CdS shell due to the difference in the lattice constant between CdS bulk shell (54.82 Å) and ZnSe bulk core (5.67 Å) [362].

Table 4.6: Device parameters of solar cells sensitized with ZnSe single core and ZnSe/CdS QDs doped with different Mn concentrations (0-3%) [354].

Samples	(a)	(b)	(c)	(d)	(e)	(f)	(g)
V_{oc} (V)	0.365	0.470	0.580	0.575	0.545	0.535	0.508
J_{sc} (mA/cm^2)	0.484	2.235	4.011	3.753	3.634	3.109	2.594
ff	0.852	0.537	0.549	0.553	0.595	0.524	0.513
η (%)	0.15	0.565	1.276	1.194	1.179	0.871	0.674

Since the strain increases the electron mobility[363, 364] and electron transport[365], one can expect that the electron mobility and transport in strained CdS could be higher than in unstrained CdS.

Compared to single ZnSe core and ZnSe/CdS core/shell, about 3 times and 10 times increase in efficiency of the device sensitized with ZnSe/CdS doped with the lowest concentration (0.25-1%) is seen. A stabilizing effect is expected for all devices because all samples were covered by a layer of ZnS to prevent recombinaition of electrons with the electrolyte[366] and trapping excitons in defect states [367].

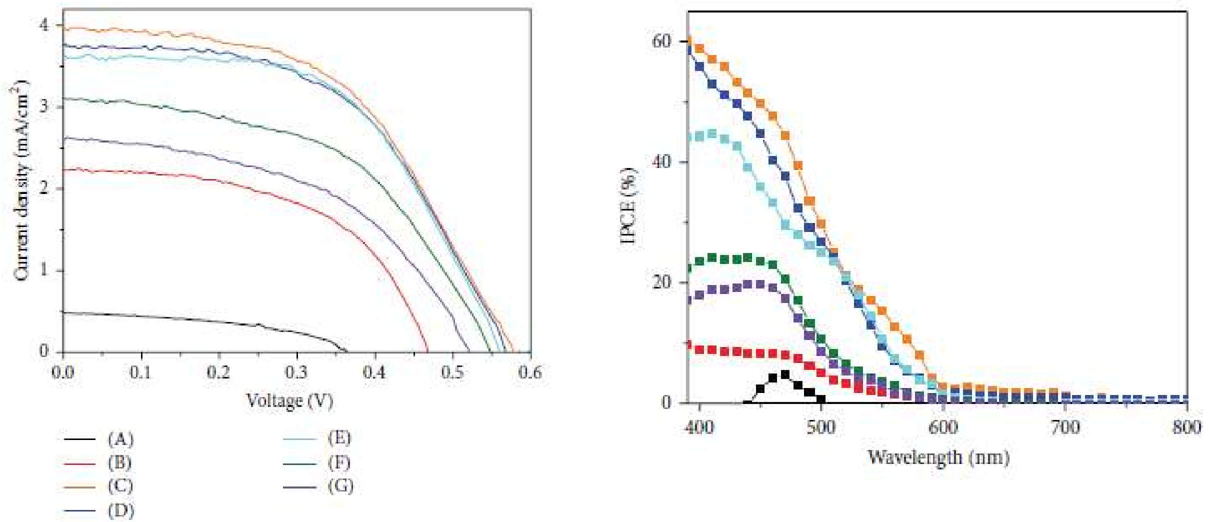

Figure 4.21: J-V characteristics and IPCE spectra of devices sensitized with ZnSe single core and ZnSe/CdS QDs doped with Mn at different concentrations (0-3%) [354]

Devices sensitized with higher Mn content (2-3%) show a decrease in all device parameters and consequently in device performance. It is attributed to a decrease in absorption range which results from lowering the band gap due to the formation of the MnS phase. The best power conversion efficiency is given by the device sensitized with ZnSe/CdS doped with the lowest Mn concentration (0.25%). This is probably because a proper Mn content generates intermediate energy states which can help separating the electron-hole pairs and suppress the recombination process [368-370]. Another issue that should be considered here is that, like for Mn doped GaAs[371], it is expected that Mn atoms occupy interstitial or substitutional sites

in Cd_{1-2x} Mn_xS lattices or precipitate as MnS. Since the solid solubility of Mn in a CdS matrix is less than 1%, a substitutional or interstitial site is expected to be occupied by Mn at low concentration, while the formation of MnS is a probable phenomenon in case of higher Mn concentration (2-3%). This hypothesis is supported by that the precipitated MnS was seen by eye for the sample with 6% Mn content.

The external quantum efficiency of all samples was estimated by incident photon to current efficiency (IPCE) measurements (**Figure 4.21**). The key equations are expressed as [372]:

$$IPCE(\lambda) = LHE(\lambda)\eta_{coll}\phi_{inj} \tag{4.6}$$

$$LHE(\lambda) = 1 - 10^{-Abs(\lambda)} \tag{4.7}$$

where ϕ_{inj}, η_{coll}, λ and $LHE(\lambda)$ are the quantum yield, the electron collection efficiency, incident light wavelength and the light harvesting efficiency, respectively.

Single ZnSe cores demonstrate poor power conversion efficiency compared to type II ZnSe/CdS core/shells, as resulting from a poor absorption and much recombination. On the other hand, an increase in IPCE of ZnSe/CdS is attributed to a wider absorption range and superior exciton separation, which suppresses recombination in type II QDs. The dramatic increase in IPCE of samples doped with low Mn content could be due to enhancement in the electron injection process. It is worthwhile to mention that new energy states formed in the band gap of QDs are responsible for the improvement in electron injection from QDs to the TiO_2 substrate. This improvement process is suppressed with increasing the Mn content to 2-3% due to the formation of impurities like MnS that can increase the recombination, as already mentioned above.

4.6.1.3. Study of excited state dynamics of ZnSe/CdS doped with different Mn concentrations

In order to evaluate the electron injection rate, time-resolved fluorescence lifetime measurements were employed. In these measurements, the excited state dynamics of the QDs wewe studied for the two conditions of deposition onto TiO_2 conductive glass and insulator glass. The fluorescence emission decay of each sample, shown in **Figure 4.22**, could be fit by a three exponential model (n=3, n is nth exponential component in equation 4.8) [373, 374]. The fit parameters listed in **Table 4.7** were used to estimate the QD lifetime by the following equation[375]:

$$<\tau> = \frac{\sum_n (a_n \tau_n^2)}{\sum_n (a_n \tau_n)} \tag{4.8}$$

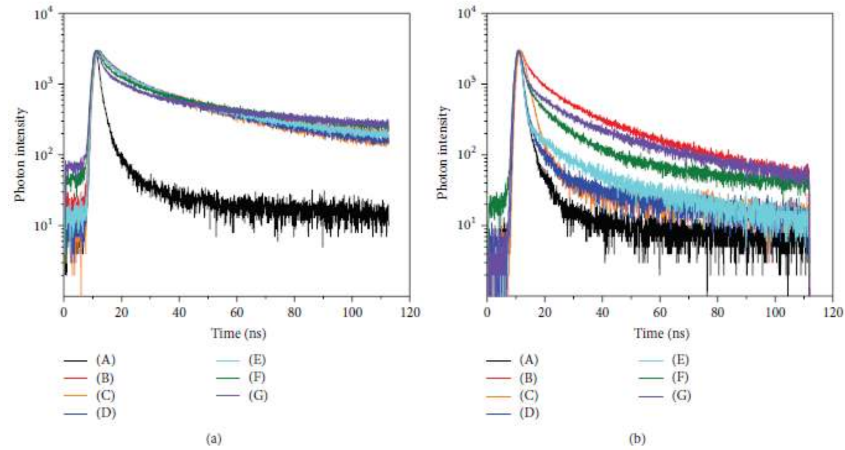

Figure 4.22: Fluorescence emission decay of ZnSe single core and ZnSe/CdS QDs doped with different Mn concentrations (0-3%) a) deposited of insulator glass, b) deposited on TiO_2 conductive glass [354].

Table 4.7: Fitting parameters, lifetime and electron injection of ZnSe single core and ZnSe/CdS QDs doped with different Mn concentrations (0-3%) [354]

TiO_2	T1	T2	T3	A1	A2	A3	CHISQ	<T>(ns)	K(n/s)
(a)	1.60	0.19	2.64	22.54	62.47	14.99	1.18	1.87	
(a)-TiO_2	0.23	2.03	1.90	32.24	25.66	42.12	1.045	1.86	0.004
(b)	13.1	2.64	54.3	33.49	6.23	60.28	1.21	49.2	
(b)-TiO_2	6.42	25.5	1.21	27.72	61.2	11.08	1.05	23.4	0.022
(c)	13.10	2.50	54.1	36.01	6.93	57.06	1.03	48.5	
(c)-TiO_2	0.32	1.74	12.5	57.4	25.53	11.72	1.03	9.15	0.088
(d)	11.90	2.30	53.8	30.72	6.22	63.06	1.03	49.5	
(d)-TiO_2	0.390	1.73	14.1	65.41	24.36	10.23	1.08	10	0.079
(e)	11.1	2.28	50.5	29.03	6.06	64.91	1.04	46.8	
(e)-TiO_2	3.38	13.8	0.31	6.32	27.25	66.43	1.15	12.6	0.058
(f)	10.6	45.8	1.53	25.38	64.63	9.99	1.06	42.7	
(f)-TiO_2	7.78	24.1	1.41	36.89	28	35.11	1.17	18.4	0.030
(g)	6.41	47.4	1.15	17.32	67.54	15.14	1.09	45.8	
(g)-TiO_2	6.13	20.9	1.11	17.23	58.25	24.51	1.24	19.4	0.029

The results based on QDs deposited onto TiO_2 conductive glass show that the fluorescence lifetime of single core ZnSe (2ns) QDs is much lower than that of type II ZnSe/CdS core/shell QDs (49 ns). This is expected because the special band structure design in type II QDs makes the electrons and holes effectively separated, delays recombination and consequently increases the fluorescence lifetime [355]. There is a difference between the fluorescence lifetime of QDs deposited on conductive glass and those deposited on an insulator which is due to the difference in the electron injection process. The electrons can be injected from the QDs to TiO_2 in the case of QDs deposited on TiO_2, resulting in a shortening of the fluorescence lifetime, but they can hardly be injected to the insulator, resulting in a long fluorescence lifetime. The electron injection rate constant of all QDs was estimated from the following equation [373, 374]:

$$K_{et} = \frac{1}{\tau_{(QD+TiO_2)}} - \frac{1}{\tau_{(QD)}} \tag{4.9}$$

$\tau_{(QD+TiO_2)}$ and $\tau_{(QD)}$ are fluorescence lifetimes obtained from QDs deposited onto the conductive and insulator glass, respectively.

As seen in **Table 4.7**, the minimum electron injection rate refers to the single ZnSe core due to the high recombination rate. This rate is increased when type II ZnSe/CdS core/shells are applied due to the special electron-hole separation which suppresses recombination. The highest rate refers to the lowest (0.25%) Mn-doped ZnSe/CdS due to the generation of optimum energy states which not only make QDs better separated but also speed up electron injection. For a deeper understanding of the device configuration and the electron transfer process from QDs to TiO_2, a physical model is considered that is schematically illustrated in **Figure 4.23**. Under light illumination, the photogenerated electrons and holes are created and confined in the conduction band of the Cds shell and valence band of the ZnSe core, respectively. Mid-states generated in the band gap of CdS by Mn atoms help transferring electrons from the conduction band of the CdS shell into the TiO_2 substrate, leading to an enhancement in power conversion efficiency.

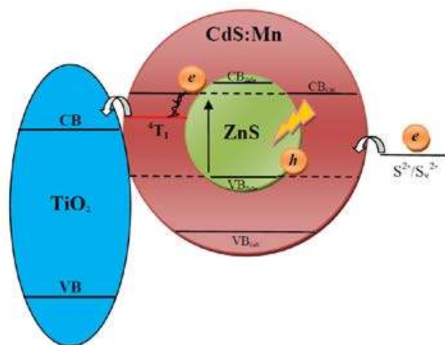

Fig 4.23: Schematics of a physical model for electron transport in a device sensitized with Mn-doped type II ZnSe/CdS QDs [354].

4.6.2. Cd-free "green" quantum dot sensitized solar cells

As a final part of my thesis, InP single core, ZnS-coated InP, Cu_2GeS_3 single core, InP-coated Cu_2GeS_3, $CuInS_2$ single core and ZnS-coated $CuInS_2$ QDs, synthesized and employed as "green" sensitizer in QDSSCs, were investigated and discussed.

4.6.2.1. Optical and structural properties of Cd-free QDs

4.6.2.1.1. Cu2GeS single core and type II Cu_2GeS_3/InP core/shell QDs

The synthesized type II Cu_2GeS_3/InP core/shell and Cu_2GeS_3 single core nanocrystals were dispersed in toluene and attached to TiO_2 nanoparticles by the drop casting technique. **Figure**

4.24 illustrates absorption spectra of the photoelectrodes sensitized with the two types of QDs as well as the corresponding band gap. The higher absorption of Cu_2GeS_3/InP is attributed to a higher QD concentration. The slight shift of the absorption onset towards longer wavelength is due to the change in color and band gap of the Cu_2GeS_3/InP QDs compared to the Cu_2GeS_3 QDs. Due to the efficient band alignment in type II Cu_2GeS_3/InP QDs, the electrons and holes are, respectively, localized in the conduction band of the shell and the valence band of the core[239], which results in a smaller band gap and broader absorption range. The band gaps of 1.75 and 1.61 eV were estimated for the Cu_2GeS_3 and Cu_2GeS_3/InP QDs, respectively, from the method described in Refs [354, 357], which confirm the band gap change.

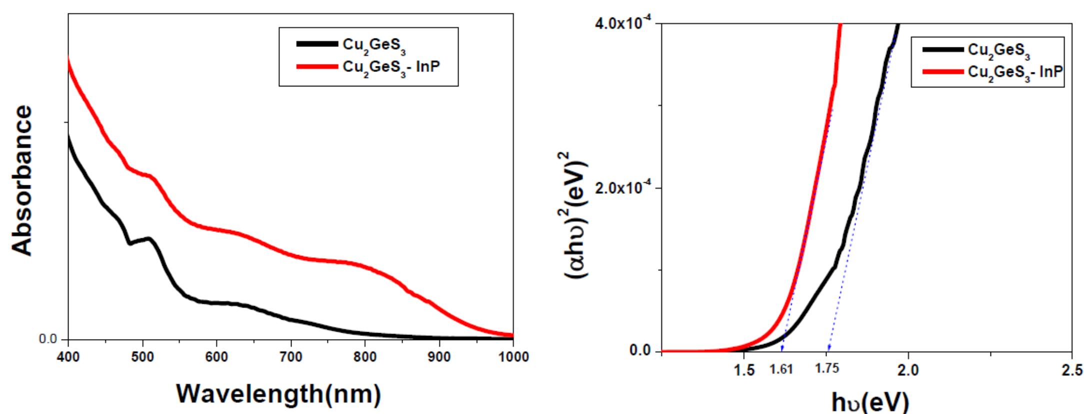

Figure 4.24: Absorption spectra and calculated band gaps of Cu_2GeS_3 and Cu_2GeS_3/InP QDs[376].

4.6.2.1.2. InP single core and ZnS shell-coated InP QDs

After the successful synthesis of pure InP single core and ZnS shell coated InP QDs, they were analyzed with a UV-Visible spectrophotometer. **Fig 4.25** shows the absorption spectra of the QDs and the corresponding band gaps.

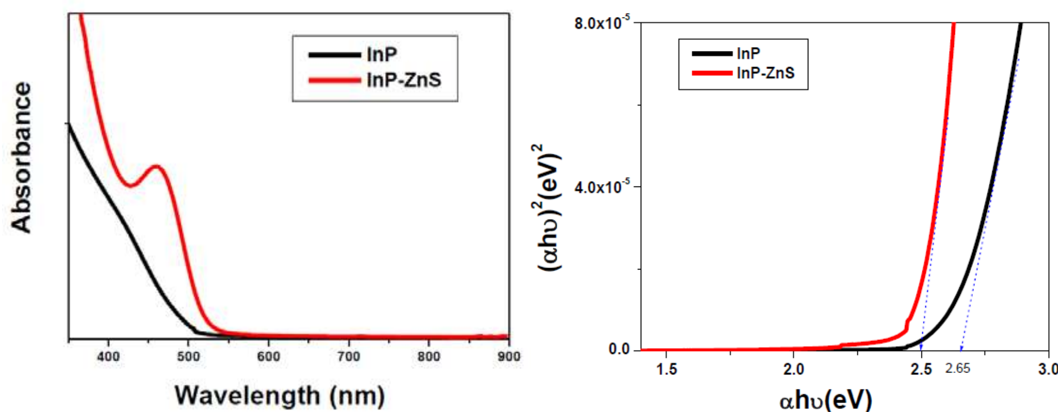

Fig 4.25: Absorption spectra and calculated band gap of InP and ZnS-coated InP [377].

The red-shift in absorption onset of ZnS-coated InP QDs is due to the change in band gap of the nanostructure. InP QDs were attributed a calculated band gap of about 2.65 eV which is somewhat higher than that of InP-ZnS (2.50 eV). This change in bandgap results in change in color of the QDs. ZnS shell coating on InP QDs causes the wave function of the exciton to change and makes the band gap of the nanostructure smaller. This behavior has been observed and reported in the literature, showing that a thicker ZnS shell leads to a broader absorption[205].

4.6.2.1.3. $CuInS_2$ single core and ZnS-coated $CuInS_2$ QDs

Colloidal pure $CuInS_2$ QDs coated with ZnS shells were successfully synthesized by the hot injection method. **Figure 4.26A-B** presents absorption and photoluminescence of as-synthesized pure $CuInS_2$ QDs and coated with a ZnS shell. Although the photoluminescence of $CuInS_2$ with the maximum peak at 810 nm is too low the broad absorption exceeding the wavelength of 850 nm is beneficial for utilization in QDSSCs (**Fig 4.27A)**. One of the reasons for the low intensity of PL in $CuInS_2$ QDs is the presence of surface defects which affect the device performance but which can be alleviated by shell coating. To eliminate surface defects and get higher quantum yield and higher PL, $CuInS_2$ QDs were coated by ZnS shells with different thickness.

As seen in **Figure 4.26B**, ZnS shell coating leads to a significant improvement in the intensity which increases with increasing ZnS shell thickness. It has been demonstrated that ZnS shell coating on $CuInS_2$ QDs could minimize the non-radiative decay, which results in a longer lifetime and higher PL intensity [280, 378]. A minor blue shift of the PL maximum is due to partial alloying of the $CuInS_2$ QDs with the wide band gap ZnS[379] and can also be ascribed to the etch of the core materials during shell growth[380].

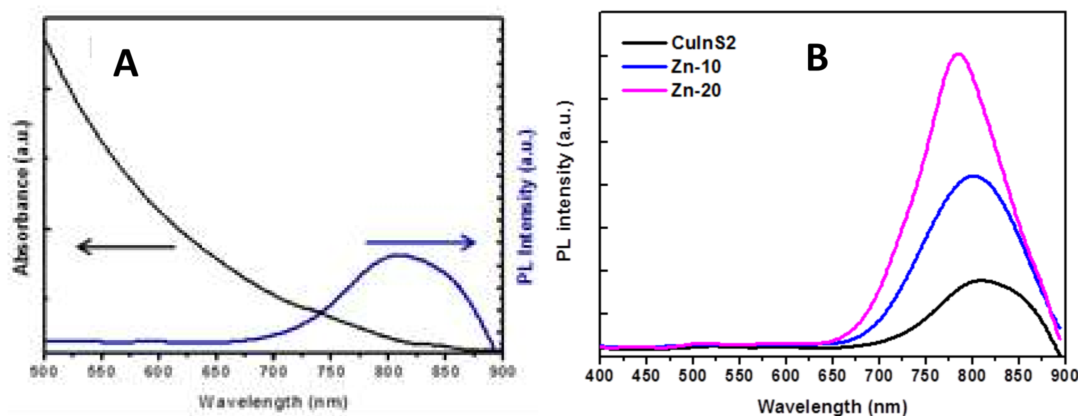

Figure 4.26: Absorption and PL spectra of pure and ZnS-coated $CuInS_2$ QDs [381].

Since the loading amount of QDs directly affects the photocurrent of the device and indirectly influences the interfacial recombination, it must be carefully evaluated. $CuInS_2$ QDs, pure or overcoated with ZnS shells, were attached to the TiO_2 substrate to evaluate the loading efficiency of the QDs. In addition, to promote the tethering of the QDs onto the TiO_2

substrate, the ligands of the $CuInS_2$ QDs were exchanged through a ligand exchange process before being attached to the TiO_2.

Figure 4.27 shows absorption spectra of $CuInS_2$ in terms of ZnS shell thickness and hybrid passivation. The photoanode sensitized with surface passivated QDs has higher absorbance and lower absorbance with a blue shift of the absorption onset with increasing the shell thickness, like previously notified.

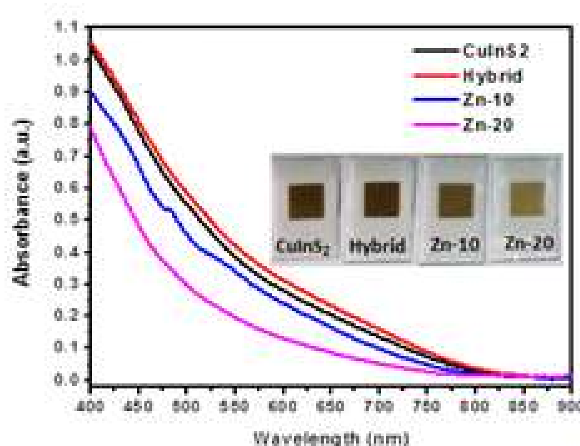

Figure 4.27: Absorbance of photoelectrode sensitized with pure, ZnS-coated and hybrid passivated $CuInS_2$ QDs [381].

Since size and shape of the QDs and type of ligand and solvent can affect the loading of the QDs onto TiO_2, we expect different images for $CuInS_2$ coated with ZnS shell and for those that are hybrid passivated. **Figure 4.28** shows TEM images of $CuInS_2$ coated with ZnS shell and those that are hybrid passivated.

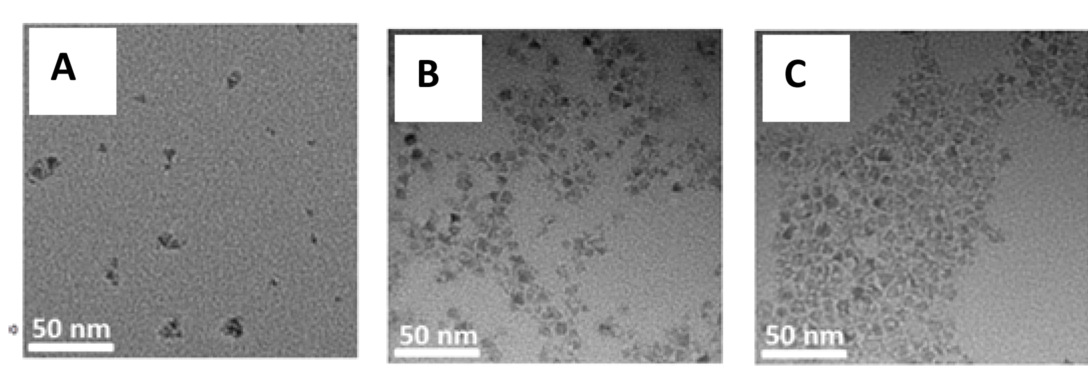

Figure 4.28: TEM image of A) hybrid passivated and ZnS-coated in B) 10min and C) 20 min [381].

TEM images of the hybrid passivated QDs indicate the size of about 7 nm, which is smaller than for those coated with different ZnS shell thickness (8 and 8.5 nm). Therefore, the lower loading efficiency of QDs coated with ZnS shell is attributed to the larger size. It means that it is difficult for the larger QDs to penetrate into the TiO_2 matrix. The higher loading efficiency

of the passivated QDs is due to a smaller chain of exchanged ligands. Thus, hybrid passivation can be an efficient way for increasing the loading efficiency of QDs onto a TiO_2 substrate.

4.6.2.2. Performance assessment - J-V and IPCE characteristics

The solar cell devices were analyzed in order to achieve information about how efficiently the incoming photons convert to electrons. To get this goal, the devices were measured under simulated light and the incident photon conversion efficiency, sometimes referred to as the external quantum efficiency (EQE), was plotted with respect to the wavelength of the incident photons. Since the absorbed photon conversion efficiency (APCE) excludes the effect of different absorbance of the photoanode resulting from different loading efficiency, it can reflect the electron transfer efficiency. To evaluate the performance of the device sensitized with different QDs, current density-voltage measurements were employed.

4.6.2.2.1. Cu_2GeS_3 single core and type II Cu_2GeS_3/InP QDs

The devices sensitized with Cu_2GeS_3 single core and type II Cu_2GeS_3/InP QDs were illuminated by AM 1.5 G simulated light - the results as current density-voltage characteristics and corresponding device parameters are shown in **Fig 4.29** and **Table 4.8**, respectively. The Cu2GeS3/InP-based device produces the higher efficiency due to its higher value of the open circuit voltage (V_{oc}=0.427 V), the short circuit current (J_{sc}=1.505 mA/cm^2) and the corresponding higher fill factor. This can be attributed to a lower recombination resulting from an efficient carrier separation in type II QDs.

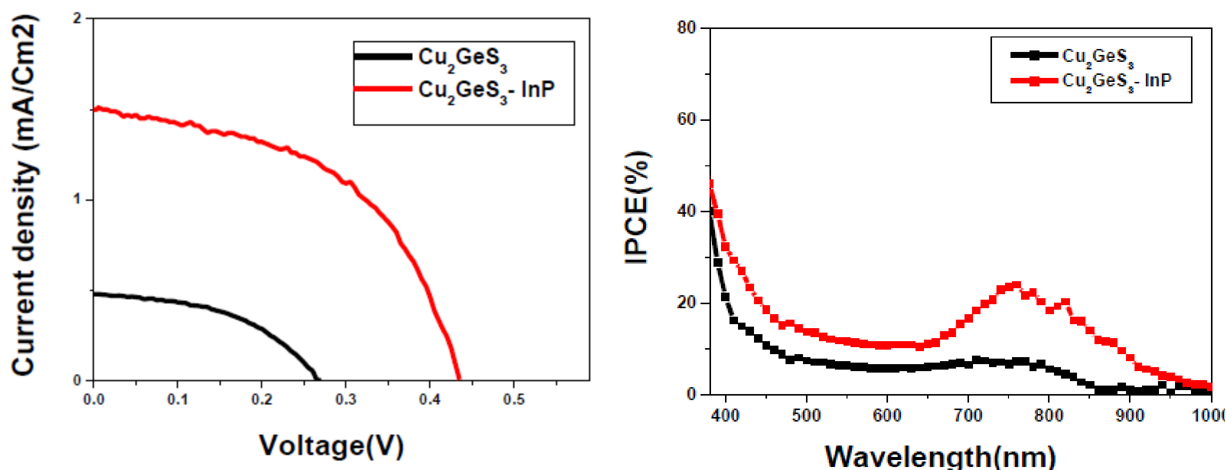

Figure 4.29: J-V characteristics and IPCE spectra of Cu_2GeS_3 and Cu_2GeS_3/InP QD based devices [376].

Table 4.8: Cu_2GeS_3 and Cu_2GeS_3/InP QD based solar cell device parameters [376]

Samples	V_{oc} (V)	J_{sc} (mA/cm^2)	*ff*	η (%)
Cu_2GeS_3	0.265	0.478	0.473	0.060
Cu_2GeS_3/InP	0.427	1.505	0.511	0.32

The IPCE of the devices, sometimes referred to as the external quantum efficiency, is illustrated in Fig 4.29 and matched with corresponding absorption spectra. The IPCE onset is seen in the wavelengths of 856 to 991 nm which are a bit longer than that of absorption. The higher IPCE refers to the type II-based device, which is in agreement with a recently published paper [382]. In fact, type II-based devices not only make the absorption broader, which increases the light harvesting efficiency, but also improve the electron injection efficiency which is responsible for the higher IPCE as calculated by

$$IPCE(\lambda) = LHE(\lambda)\eta_{coll}\phi_{inj} \tag{4.10}$$

4.6.2.2.2. ZnS-coated InP QDs

The J-V characteristics of the devices sensitized with the two types of QDs (InP single core and ZnS-coated InP) are illustrated in **Figure 4.30** and the device parameters are summarized in **Table 4.9**.

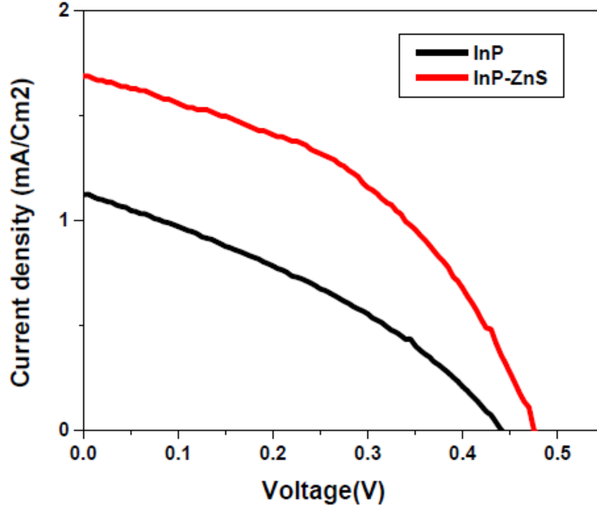

Figure 4.30: J-V characteristics of device sensitized with InP and ZnS-coated InP QDs [377].

Table 4.9: InP and ZnS-coated InP-based solar cell device parameters [377]

Samples	(a)	(b)
V_{oc} (V)	0.440	0.475
J_{sc} (mA/cm^2)	1.124	1.574
ff	0.344	0.469
η (%)	0.17	0.351

It is found that the device sensitized with ZnS-coated InP QDs exhibits higher efficiency which results from a higher open circuit voltage (0.475 V) and short circuit current (1.574 mA/cm^2). The higher V_{oc} in the InP-ZnS based device could be ascribed to the higher J_{sc} as follow[383]:

$$V_{oc} = \frac{K_b T}{q\beta}[\ln \frac{J_{sc}}{J_o} + 1] \tag{4-11}$$

where J_o is the dark current, T is temperature, q is electron charge and β is the Boltzmann constant.

The higher fill factor shows that ZnS shell coating suppresses carrier recombination. It may be due to surface passivation of the InP QDs, which causes the number of surface traps to decrease. The same effect was observed for ZnS shell-coated $CuInS_2$ QDs, which is explained in the next section. It is worthwhile to mention that the ZnS shell coating of the InP QDs not only protects these sensitive QDs against moisture and electrolyte but also makes the device efficiency to increase by more than 2 times.

The IPCE and APCE spectra of the two devices are shown in **Figure 4.31**. The difference between IPCE and APCE is attributed to different loading amount of the QDs into the TiO_2 matrix. Comparing the absorption of QDs and IPCE shows that the absorption onset is red-shifted for both devices. The higher value of the IPCE for the device sensitized with InP-ZnS is attributed to the broader absorption range, which increases the light harvesting efficiency and improves the electron injection efficiency. It should be mentioned here that ZnS was recently used as a wide band gap semiconductor to increase the quantum yield and stability of InP [206, 208, 209]. Since InP QDs are very sensitive to moisture, the lower IPCE of the device sensitized with InP QDs could be attributed to the low stability of InP QDs. The capability of InP QDs is thus affected by air and electrolyte prior to and during the measurement. Lower absorption range and electron injection efficiency can be other reasons for low values of the IPCE. Lifetime measurements are here needed in order to further evaluate the electron injection and transfer. It is notable that ZnS shells not only protect InP QDs against moisture and electrolyte but also significantly increases the power conversion efficiency.

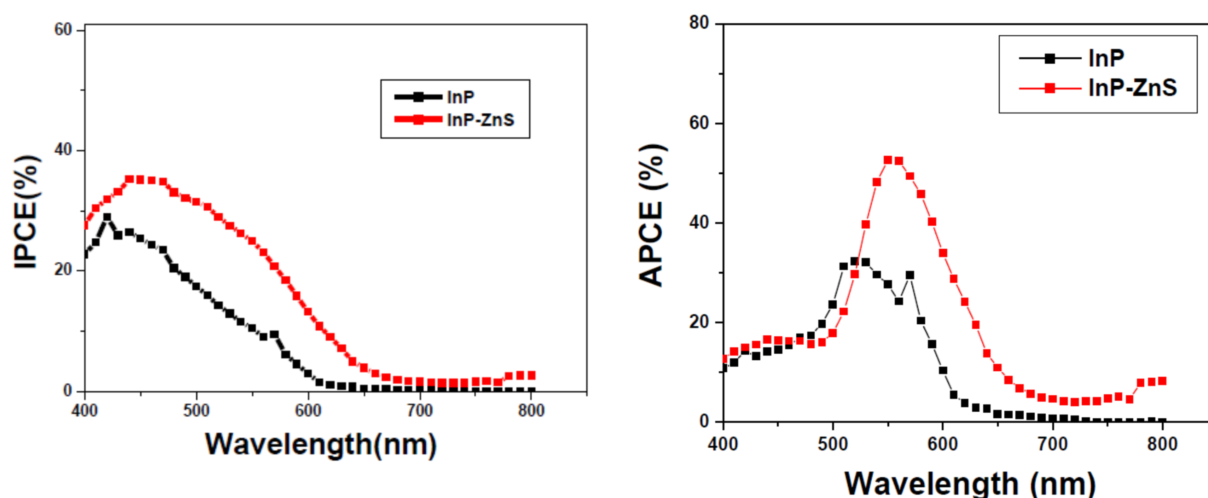

Figure 4.31: IPCE and APCE spectra of devices sensitized with InP single core and ZnS-coated InP QDs [377].

4.6.2.2.3. ZnS-coated $CuInS_2$ QDs

Figure 4.32 illustrates the J-V characteristics of the devices and the corresponding device parameters are summarized in **Table 4.10**. The highest efficiency with the value of 4.7% refers to the device sensitized with hybrid passivated QDs. This high efficiency results from the higher current density (J_{sc}) and potential (V_{oc}) with the value of 15.34 mA/Cm^2 and 0.560 V, respectively. The higher value of J_{sc} can be attributed to the hybrid pasivation strategy.

Hybrid passivation not only improves the loading of QDs onto the TiO_2 substrate, which can enhance the light harvesting efficiency, but can also promote the quantum efficiency of the QDs, which in turn can increase electron injection. The increase of V_{oc} could be due to a decrease of carrier recombinaton at the interfaces, which may be caused by the decrease of surface defects in the hybrid passivated QDs.

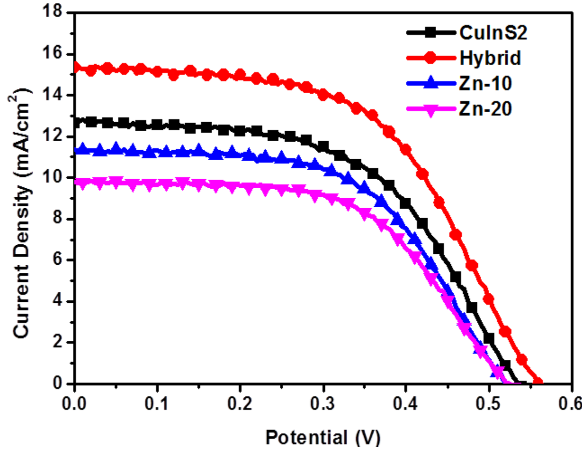

Figure 4.32: J-V characteristics of devices sensitized with pure, ZnS-coated and hybrid passivated $CuInS_2$ QDs [381]

Table 4.10: Device parameters of solar cells sensitized with pure, ZnS-coated and hybrid passivated $CuInS_2$ QDs [381]

Samples	CuInS2	Hybrid	Zn-10	Zn-20
V_{oc} (V)	0.535	0.560	0.520	0.525
J_{sc} (mA/cm^2)	12.67	15.34	11.35	9.81
ff	0.544	0.545	0.561	0.567
η (%)	3.7	4.7	3.3	2.9

Compared to pure QDs, the ZnS shell coating causes the corresponding device efficiency to decrease so that the efficiency is lowered while increasing the shell thickness. The low efficiency can be ascribed to a low loading of the QDs. The improvement in fill factor of the ZnS shell coated devices is believed to be mainly due to a suppression of recombination. The fill factor is increased with increasing shell thickness which indicates that ZnS shells could eliminate surface traps. The IPCE and calculated APCE of the studied devices are shown in **Figure 4.33**.

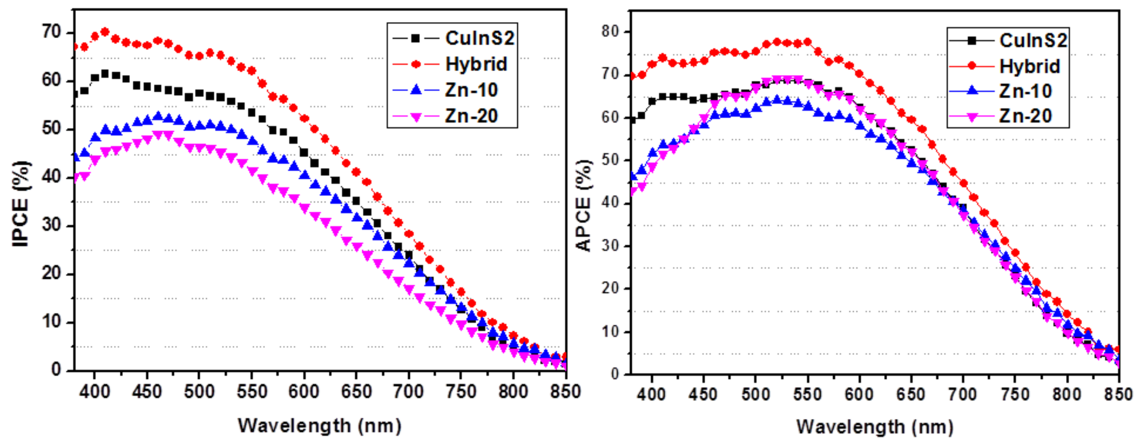

Figure 4.33: The IPCE and APCE spectra of devices sensitized with pure, ZnS coated and hybrid passivated $CuInS_2$ QDs [381].

Significant enhancement in both IPCE and APCE of the devices sensitized with hybrid passivated QDs is evidenced, indicating that hybrid passivation increases the electron transfer efficiency through improving the quantum yield (ϕ_{inj}) and electron collection efficiency (η_{cc}). This improvement can be attributed to a decrease of surface traps under the hybrid passivation process.

A significant reduction in IPCE of the devices sensitized with ZnS shell coating is seen. From the APCE it is found that one of the reasons for this reduction is lowering of the loading of QDs onto the photoelectrode. Another reason is that the ZnS shell acts as a barrier for the photogenerated electrons and prevents electron transfer from $CuInS_2$ to the TiO_2 substrate due to that the conduction band of ZnS is higher than that of $CuInS_2$[310]. It has recently been demonstrated that ZnS shells decrease the electron transfer which is responsible for the electron transfer efficiency[384].

4.6.2.3. Study of excited state dynamics of Cu_2GeS_3 single core and type II Cu_2GeS_3/InP QDs

The excited state dynamics of Cu_2GeS_3 and type II Cu_2GeS_3/InP QDs were evaluated by time-resolved transient measurements - the corresponding curves are shown in **Fig 4.34** and **Figure 4.35**, including fitting model and residuals.

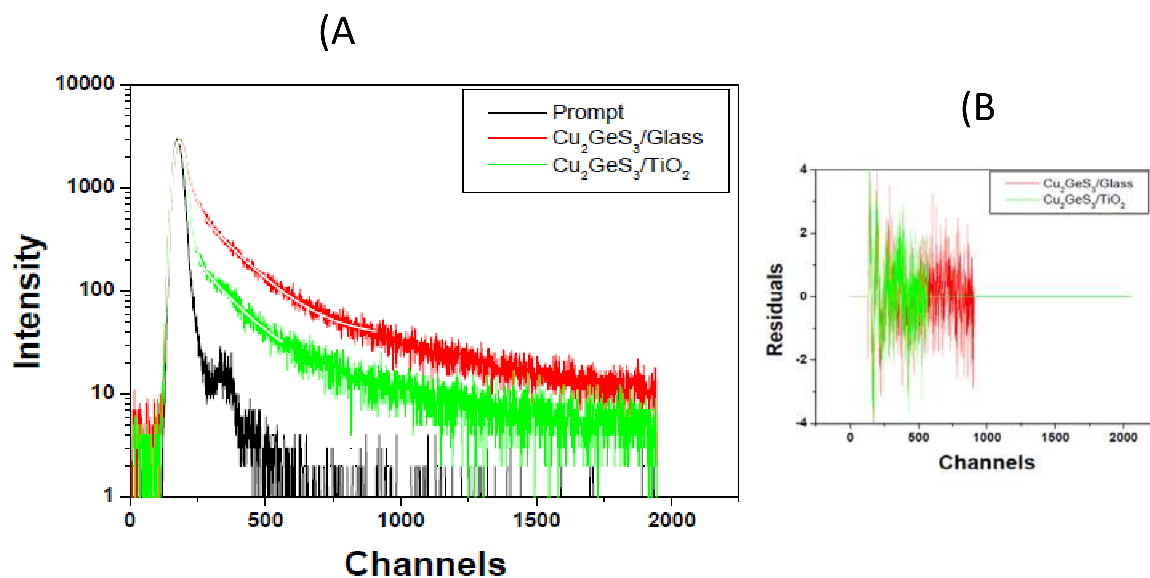

Figure 4.34: Time-resolved fluorescence intensity decay curves, fitting model (A) and residuals (B) of Cu_2GeS_3 QDs deposited onto insulator glass[376].

The three-exponential model was matched to the curve and the fitting data was used to calculate the lifetimes and the electron injection rate constants. The lifetime of Cu_2GeS_3/InP and Cu_2GeS_3 QDs deposited on insulator glass were 8.11 and 5.92 ns, which are higher than that of QDs deposited on TiO_2. That is due to the more efficient electron-hole pair separation in type II QDs that not only decreases wave function overlap but also delays recombination[355].

Electron injection rate constants of QDs calculated from the lifetime shown in **Table 4.11** demonstrate that Cu_2GeS_3/InP-based devices have higher values for the electron injection.

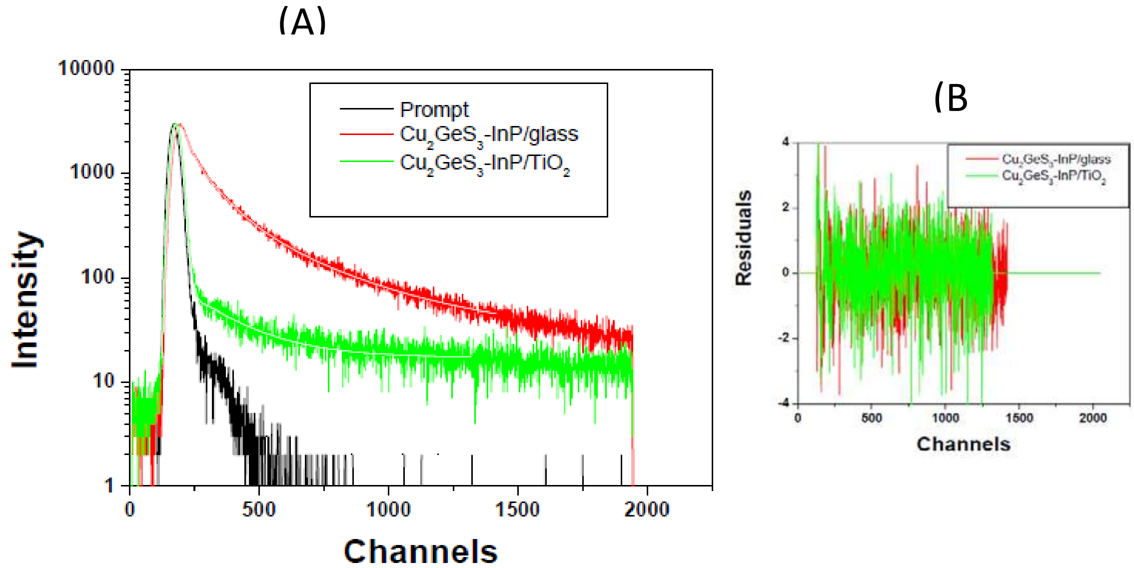

Figure 4.35: Time-resolved fluorescence intensity decay curves, fitting model (A) and residuals (B) of Cu_2GeS_3 QDs deposited onto TiO_2 conductive glass[376].

It is attributed to efficient carrier extraction which facilitates electron transport from the QDs to the TiO_2 substrate. This effect in type II QDs was recently reported and attributed to special band structure design of the nanostructures where the conduction band energy level of the core is higher than that of the shell[382]. The increase in electron injection rate constant can directly affect the device efficiency as electron injection and collection play important roles.

Table 4.11: Fitting parameters, life time and electron injection of Cu_2GeS_3 and Cu_2GeS_3/InP QDs [376]

TiO_2	T1	T2	T3	A1	A2	A3	CHISQ	<T>	K (ns^{-1})
Cu_2GeS_3-InP	2.92	10	0.72	42.87	39.32	17.81	1.08	8.11	
Cu_2GeS_3-InP /TiO_2	0.30	5.78	0.69	41.32	8.66	50.02	1.22	3.25	0.184
Cu_2GeS_3	0.16	6.26	0.24	37.3	34.91	27.79	1.19	5.92	
Cu_2GeS_3/TiO_2	0.28	0.18	4.55	48.95	24.89	26.16	1.86	3.98	0.082

For a better understanding of electron injection and transfer in type II Cu_2GeS_3/InP QDs the physical model shown in **Figure 4.36** is considered. Since these QDs are type II, a similar mechanism as for ZnSe/CdS is expected. Photogenerated electrons and holes are confined in the conduction band of the shell and the valence band of the core, respectively. The electron is

then injected into TiO_2 and the QD is reset by hole transport through the redox couple of the electrolyte. This process is repeated to give a current which flows in the circuit connected to the device.

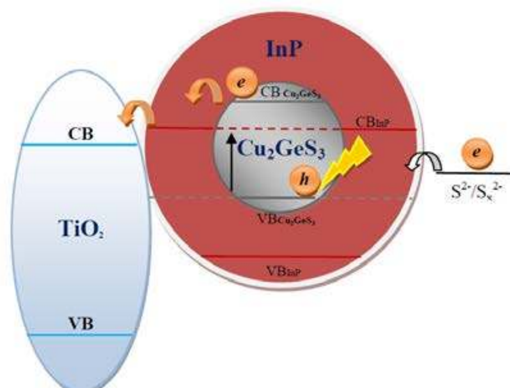

Figure 4.36: Schematic of physical model showing the electron transport in the device sensitized with Cu_2GeS_3/InP QDs [376].

In summary, Mn-doping of Cd-based QDSSCs and ZnS-shell coating, design of type II and hybrid passivation in Cd-free and "green" QDSSCs were successfully employed as strategies to boost the solar cell power conversion efficiency. Mn doping as a band gap engineering tool not only increases the absorption range but also facilitates electron injection which is responsible for the higher efficiency. Due to the nature of type II core-shells, Cu_2GeS_3-InP QDs not only give large absorption exceeding to the infrared region but also increases the electron injection rate, which results in higher power conversion efficiency. The thin ZnS-shell thickness in InP-ZnS QDs makes them air and moisture stable. The red-shift of absorption onset causes the QD absorption to increase. These benefits together with the high quantum yield of InP-ZnS QDs lead to an increase of the efficiency when compared to InP-based devices. ZnS-shell coating decreases the surface traps and hybrid passivation increases the loading efficiency of the $CuInS_2$ QDs into the substrate, which is responsible for the improvement of device performance.

CHAPTER 5

Conclusions and Future Outlook

5.1. Conclusions

This thesis presents results of research in the areas of electronics, photonics and photovoltaics. The main focus was to investigate, design and fabricate multicomponent nanostructures for MOSFET, photonic detector and hybrid solar cell applications. From the experimental points of view, a number of pure and doped epitaxial strain relaxed and compressive strained GeSn(Si,C) layers were grown, characterized and developed to produce tensile strained layers in Ge/GeSn(Si)/GeSi/Ge/Si and Ge/GeSn/Si system heterostructures, which are promising for MOSFET, photonic detector and second generation solar cell applications. Colloidal Cd-based and Cd-free QDSSCs were fabricated and explored for applications in 3rd generaton solar cells. Type II ZnSe/CdS QDs as Cd-based QDs, type II Cu_2GeS_3/InP, ZnS-coated InP QDs and $CuInS_2$ QDs as Cd-free QDs were employed as sensitizers in solar cell devices and evaluated. The results are summarized as follows:

Strain-relaxed layers:

1- Epitaxial strain- relaxed GeSn layers were successfully grown by RPCVD at different temperatures. The Sn segregation was found to increase with increase of the growth temperature which affects the interface quality when p-i-n devices are fabricated.

2- Low resistivity was obtained for boron-doped layers with low partial pressure. Strain-relaxed GeSn layers were found to be usable as a template to produce tensile strain layers, while they could not be integrated in the main part of p-i-n device due to high defect density coming from large mismatch between the lattice constant of the layer and substrate.

Compressive strain layers:

1- Pure and doped epitaxial compressive-strained GeSn(Si,C) layers were grown on virtual Ge substrates by RPCVD at different temperatures, showing that Sn can successfully be introduced into a Ge matrix.

2- It was found that high temperature causes strain to relax and that increasing the Si content and phosphor and boron doping can compensate the strain and increase the Sn content due to the small atomic size of Si and dopants. Furthermore, introducing C atoms offers layers that are totally strain-compensated having no Sn segregation and consequently high surface quality which can be utilized in the main part of a p-i-n device.

3- Lower resistivity was achieved at higher temperature and lower temperature for boron and phosphor doping, respectively, which is useful for a p-i-n device.

4- Compared to the RTP technique, NiSiGe with low resistivity as a contact was formed by MWA at low temperature which is compatible for CMOS technology in which a low thermal budget is demanded.

Tensile strain layers:

1- Ge/GeSn/Si and Ge/GeSn(Si)/GeSi/Ge/Si systems were designed and successfully fabricated to produce tensile strain of 0.52 and 45%, corresponding to bandgaps of 0.65 and 0.72 eV, respectively.

2- Two heterostructures are proposed for detection applications where indirect-direct band gaps are useful, and also for high performance channel MOSFETs in CMOS technology where high carrier mobility tensile strain layers are needed.

Quantum dots:

Cd-based

Colloidal pure and Mn-doped ZnSe/CdS core/shell QDs with various Mn concentrations were successfully synthesized by the hot injection method and employed as sensitizers in solar cells. Proper Mn-doping was found to cause an increase in the absorption spectra and red shift in the absorption band edge and in the photoluminescence emission peak. The mid-states generated by Mn can facilitate electron transfer from the QDs to the TiO2 substrate. Superior light absorption, better carrier separation in type II QDs and efficient electron injection rates offer a power conversion efficiency of about 2 and 3 times larger than those of core and undoped QDSSCs, respectively.

Cd-free

1- Low toxic type II QDs using Cu_2GeS_3 as core and InP as shell were theoretically designed and colloidal Cu_2GeS_3 single core and type II Cu_2GeS_3/InP QDs were experimentally synthesized and employed in QDSSCs. Cu_2GeS_3 shows absorption extending to the infrared region and an even larger red-shift was achieved by type II Cu_2GeS_3/InP QDs. This red-shift corresponds to a change towards a smaller bandgap due to the manipulation of the conduction and valence bands, which can harvest light energy located even in the infrared spectrum. Special band structure engineering and creation of improved electron-

hole separation through design of type II Cu_2GeS_3/InP QDs not only give superior ability to broaden the absorption range but could also facilitate the electron transfer from the QDs to the TiO_2 substrate, which all resulted in increasing the device performance by 5 times.

2- ZnS-coated InP QDs were successfully synthesized and employed as sensitizers in QDSSCs. ZnS-coating caused broader absorption through red-shift in the absorption spectrum and was successful for protecting the moisture-sensitive InP QDs against interaction with air and electrolyte. In addition, it suppressed recombination, decreased the surface traps and made the device power conversion efficiency to increase by more than 2 times.

3- ZnS-coating and hybrid passivation were employed to evaluate $CuInS_2$-based QDSSCs. ZnS is successful to suppress recombination but it also blocks the electrons to be transferred to the substrate. In contrast, hybrid passivation increased the loading efficiency of the QDs and decreased surface traps, which are aspects responsible for the higher efficiency.

5.2. Future outlook

Since many findings in this work are new and have not been earlier addressed, more in depth interpretations are required and more aspects need to be investigated than what here was possible due to the limited time available for this thesis work. For example, one important issue investigated in this thesis was the mobility enhancement for utilization of tensile strain in MOSFETs. Two ways of increasing the mobility in MOSFETs were investigated - fabrication of tensile strained Ge for MOSFET channels and utilization of compressive strained GeSn to produce tensile strain in MOSFET channels. Here, more measurements, such as Hall measurements, could be suggested to experimentally evaluate the real electron and hole mobility in these layers. To compare the effect of tensile strain on the speed of photodetectors, fabrication of relaxed and compressive-based photodetectors as well as tensile-based photodetectors are suggested. The structures of n-GeSn/i-GeSn/p-GeSn/Ge/Si and n-GeSn/i-GeSn/p-GeSn/GeSn/Si and n-Ge/i-Ge/p-Ge/GeSn/Si (or n-Ge/i-Ge/p-Ge/GeSn(Si)/GeSi/Ge/Si) for detection in the infrared region can be considered for compressive, relaxed and tensile-based photodetectors, respectively. Two important applications of photodetectors mentioned above are - medical applications where the skin becomes invisible and blood veins and blood liquids can be analyzed, and where the structure of veins, that is unique for each person, can be imaged as an alternative to fingerprints for a cheap and easy way of identification.

The loading efficiency of QDs investigated in this work can be further increased by hybrid passivation, particularly for ZnS-coated InP and Cu_2GeS_3/InP QDs as novel low toxic and “green” QDs employed in QDSSCs. Due to special band alignment in devices sensitized with Cu_2GeS_3-InP and $CuInS_2$ QDs, the use of materials like Spiro could be an effective way to enhance hole transport and consequently reset the QDs effectively. The effects of shell thickness in Cu_2GeS_3-InP and InP-ZnS QDs in terms of stability and efficiency should be further investigated. The excited state dynamics of InP-ZnS and $CuInS_2$ QDs should be evaluated to obtain more information about lifetimes and electron injection rates. The stability

of QDs as an important factor in QDSSCs should be further evaluated. These are just a few examples of measures that are pressing for making QD sensitized solar cells competitive in the future energy market.

While all Cd-free QDs investigated in this thesis have potential for commercialization due to low toxicity and eco-friendly properties, the power conversion efficiency must clearly be improved. To get this goal, three different ways can be suggested: one way is to use low dimensional materials such as carbon nanotubes and graphene in the photoanode and counter electrode to increase the conductivity for electron and hole transport. Another way is to use electrolyte solutions, like iodide and bromide-based redox couples, which have different Fermi levels. This could be an effective way for better hole transport. Doping QDs with transition metals and upconversion nanaoparticles is another approach to increase the efficiency.

The low toxic sensitizer QDs are thus alternatives to toxic Cd, Pb and Hg-based QDs that have been employed as dopants in dye-sensitized, solid state and perovskite solar cells. Due to high quantum yield and photoluminescence, InP-ZnS QDs can be further used as biomarkers in biology systems or for cancer therapy where QDs can be sensitized by bacteria in the human body using bio-ligands. The scope is thus wide open for taking the area of my thesis research many steps further for the benefit of new technology with applications in areas that are useful for society and mankind.

References

1. Buzea, C., I.I. Pacheco, and K. Robbie, *Nanomaterials and nanoparticles: Sources and toxicity.* Biointerphases, 2007. **2**(4): p. MR17-MR71.
2. Roduner, E., *Size matters: why nanomaterials are different.* Chemical Society Reviews, 2006. **35**(7): p. 583-592.
3. Cao, G. and Y. Wang, *Nanostructures and Nanomaterials: Synthesis, Properties, and Applications*. 2011: World Scientific.
4. Busch, G., *Early history of the physics and chemistry of semiconductors-from doubts to fact in a hundred years.* European Journal of Physics, 1989. **10**(4): p. 254.
5. Badawy, W.A., *A review on solar cells from Si-single crystals to porous materials and quantum dots.* Journal of advanced research, 2015. **6**(2): p. 123-32.
6. Fortunato, E., P. Barquinha, and R. Martins, *Oxide Semiconductor Thin-Film Transistors: A Review of Recent Advances.* Advanced Materials, 2012. **24**(22): p. 2945-2986.
7. Park, J.S., et al., *Review of recent developments in amorphous oxide semiconductor thin-film transistor devices.* Thin Solid Films, 2012. **520**(6): p. 1679-1693.
8. Martyniuk, P., et al., *New concepts in infrared photodetector designs.* Applied Physics Reviews, 2014. **1**(4).
9. Pennelli, G., *Review of nanostructured devices for thermoelectric applications.* Beilstein Journal of Nanotechnology, 2014. **5**: p. 1268-1284.
10. Pillarisetty, R., *Academic and industry research progress in germanium nanodevices.* Nature, 2011. **479**(7373): p. 324-328.
11. Assefa, S., F. Xia, and Y.A. Vlasov, *Reinventing germanium avalanche photodetector for nanophotonic on-chip optical interconnects.* Nature, 2010. **464**(7285): p. 80-U91.
12. Moontragoon, P., Z. Ikonić, and P. Harrison, *Band structure calculations of Si–Ge–Sn alloys: achieving direct band gap materials.* Semiconductor Science and Technology, 2007. **22**(7): p. 742.
13. Liu, J.F., et al., *Tensile strained Ge p-i-n photodetectors on Si platform for C and L band telecommunications.* Applied Physics Letters, 2005. **87**(1).
14. Wang, J.L., W.-Y. ; Zang, H. ; Yu, M.B. ; Chua, K.T. ; Loh, T.H. ; Ye, J.D. ; Yang, R. ; Wang, X.L. ; Lee, S.J. ; Cho, B.J. ; Lo, G.Q. ; Kwong, D.L., *Integration of Tensile-Strained Ge p-i-n Photodetector on Advanced CMOS Platform.* IEEE International Conference on Group IV Photonics GFP: p. 52-54.
15. Jamshidi, A., et al., *Growth of GeSnSiC layers for photonic applications.* Surface & Coatings Technology, 2013. **230**: p. 106-110.
16. Fischetti, M.V. and S.E. Laux, *Band structure, deformation potentials, and carrier mobility in strained Si, Ge, and SiGe alloys.* Journal of Applied Physics, 1996. **80**(4): p. 2234-2252.
17. Krishnamohan, T., et al., *High-mobility ultrathin strained Ge MOSFETs on bulk and SOI with low band-to-band tunneling leakage: Experiments.* Ieee Transactions on Electron Devices, 2006. **53**(5): p. 990-999.

18. Sau, J.D. and M.L. Cohen, *Possibility of increased mobility in Ge-Sn alloy system.* Physical Review B, 2007. **75**(4).
19. Umesh K. Mishra, J.S., *Semiconductor Device Physics and Design*. 2008: Springer.
20. Davies, J.H., *The Physics of Low-dimensional Semiconductors*. 1998: Cambridge Uunversity.
21. Fewster, P.F. and N.L. Andrew, *Determining The Lattice-Relaxation In Semiconductor Layer Systems By X-Ray-Diffraction.* Journal of Applied Physics, 1993. **74**(5): p. 3121-3125.
22. Radamson, H.H. and J. Hallstedt, *Application of high-resolution x-ray diffraction for detecting defects in SiGe(C) materials.* Journal of Physics-Condensed Matter, 2005. **17**(22): p. S2315-S2322.
23. Endres, J., S. Danis, and G. Bauer, *The misfit dislocation density profile in graded SiGe/Si(001) layers prepared at different temperatures.* Journal of Physics-Condensed Matter, 2013. **25**(17).
24. Marshall, A.F., et al., *Misfit dislocation dissociation and Lomer formation in low mismatch SiGe/Si heterostructures.* Journal of Materials Research, 2005. **20**(2): p. 447-455.
25. Yu, D., Y. Zhang, and F. Liu, *First-principles study of electronic properties of biaxially strained silicon: Effects on charge carrier mobility.* Physical Review B, 2008. **78**(24).
26. Kang, T.-K., *Physics of enhanced impact ionization in strained-Si p-channel metal-oxide-semiconductor field-effect transistors.* Applied Physics Letters, 2008. **92**(15).
27. Takagi, S.I., et al., *Comparative study of phonon-limited mobility of two-dimensional electrons in strained and unstrained Si metal-oxide-semiconductor field-effect transistors.* Journal of Applied Physics, 1996. **80**(3): p. 1567-1577.
28. Lieten, R.R., et al., *Tensile-Strained GeSn Metal-Oxide-Semiconductor Field-Effect Transistor Devices on Si(111) Using Solid Phase Epitaxy.* Applied Physics Express, 2013. **6**(10).
29. Gupta, S., et al., *Achieving direct band gap in germanium through integration of Sn alloying and external strain.* Journal of Applied Physics, 2013. **113**(7): p. 073707.
30. Wirths, S., et al., *Lasing in direct-bandgap GeSn alloy grown on Si.* Nature Photonics, 2015. **9**(2): p. 88-92.
31. Liu, L., et al., *Effect of tensile strain on the electronic structure of Ge: A first-principles calculation.* Journal of Applied Physics, 2014. **116**(11).
32. Pizzi, G., M. Virgilio, and G. Grosso, *Tight-binding calculation of optical gain in tensile strained 001 -Ge/SiGe quantum wells.* Nanotechnology, 2010. **21**(5).
33. El Kurdi, M., et al. *Stimulated emission in single tensile-strained Ge photonic wire*. in *Group IV Photonics (GFP), 2011 8th IEEE International Conference on*. 2011.
34. Hoshina, Y., et al., *First-Principles Analysis of Indirect-to-Direct Band Gap Transition of Ge under Tensile Strain.* Japanese Journal of Applied Physics, 2009. **48**(4).
35. Wang, X., et al., *Infrared absorption of n-type tensile-strained Ge-on-Si.* Optics Letters, 2013. **38**(5): p. 652-654.
36. Wirths, S., et al., *Band engineering and growth of tensile strained Ge/(Si)GeSn heterostructures for tunnel field effect transistors.* Applied Physics Letters, 2013. **102**(19).

37. Zhu, Y., et al., *Tensile-Strained Nanoscale Ge/In0.16Ga0.84As Heterostructure for Tunnel Field-Effect Transistor.* Acs Applied Materials & Interfaces, 2014. **6**(7): p. 4947-4953.
38. Lin, H., et al., *Low-temperature growth of Ge1 − xSnx thin films with strain control by molecular beam epitaxy.* Thin Solid Films, 2012. **520**(11): p. 3927-3930.
39. Su, S., et al., *Epitaxial growth and thermal stability of Ge1−xSnx alloys on Ge-buffered Si(0 0 1) substrates.* Journal of Crystal Growth, 2011. **317**(1): p. 43-46.
40. He, G. and H.A. Atwater, *Synthesis of epitaxial SnxGe1−x alloy films by ion-assisted molecular beam epitaxy.* Nuclear Instruments and Methods in Physics Research Section B: Beam Interactions with Materials and Atoms, 1995. **106**(1–4): p. 126-132.
41. Bauer, M., et al., *Ge-Sn semiconductors for band-gap and lattice engineering.* Applied Physics Letters, 2002. **81**(16): p. 2992-2994.
42. Grzybowski, G., et al., *Next generation of Ge1−ySny (y = 0.01-0.09) alloys grown on Si(100) via Ge3H8 and SnD4: Reaction kinetics and tunable emission.* Applied Physics Letters, 2012. **101**(7): p. 072105.
43. Vincent, B., et al., *Undoped and in-situ B doped GeSn epitaxial growth on Ge by atmospheric pressure-chemical vapor deposition.* Applied Physics Letters, 2011. **99**(15): p. 152103.
44. Jha, A.R., *Solar cell technology and applications*. 2009: CRC press.
45. Mcintosh, P., *Solar Cell Technology*. 2012: India: World Technologies.
46. Hussein, A.K., *Applications of nanotechnology in renewable energies—a comprehensive overview and understanding.* Renewable and Sustainable Energy Reviews, 2015. **42**: p. 460-476.
47. Chapin, D.M., C.S. Fuller, and G.L. Pearson, *A New Silicon p‐n Junction Photocell for Converting Solar Radiation into Electrical Power.* Journal of Applied Physics, 1954. **25**(5): p. 676-677.
48. Werner, J.H., *Second and third generation photovoltaics dreams and reality*, in *Advances in Solid State Physics 44*, B. Kramer, Editor. 2004. p. 51-66.
49. Conibeer, G., *Third-generation photovoltaics.* Materials Today, 2007. **10**(11): p. 42-50.
50. Kouhnavard, M., et al., *A review of semiconductor materials as sensitizers for quantum dot-sensitized solar cells.* Renewable and Sustainable Energy Reviews, 2014. **37**: p. 397-407.
51. Albero, J., et al., *Efficiency Records in Mesoscopic Dye-Sensitized Solar Cells.* Chemical Record, 2015. **15**(4): p. 803-828.
52. Ring, E.F.J. and K. Ammer, *Infrared thermal imaging in medicine.* Physiological Measurement, 2012. **33**(3): p. R33-R46.
53. Figgemeier, H., et al., *SWIR detectors for night vision at AIM.* Infrared Technology and Applications Xl, 2014. **9070**.
54. Rieke, G.H., *Infrared detector arrays for astronomy*, in *Annual Review of Astronomy and Astrophysics*. 2007. p. 77-115.
55. Dumas, D., et al., *Curved infrared detectors: application to spectrometry and astronomy.* High Energy, Optical, and Infrared Detectors for Astronomy Iv, 2010. **7742**.
56. Kinch, M.A., *Fundamentals of Infrared Detector Materials*. 2007: SPIE.

57. Yeh, C., *Applied photonics*. 1994.
58. Byrnes, J., *Unexploded Ordnance Detection and Mitigation*. 2008: Springer.
59. Corsi, C., *History highlights and future trends of infrared sensors.* Journal of Modern Optics, 2010. **57**(18): p. 1663-1686.
60. Rogalski, A., *HgCdTe infrared detector material: history, status and outlook.* Reports on Progress in Physics, 2005. **68**(10): p. 2267-2336.
61. Rogalski, A., *Quantum well photoconductors in infrared detector technology.* Journal of Applied Physics, 2003. **93**(8): p. 4355-4391.
62. Lu, W., et al., *Development of an infrared detector: Quantum well infrared photodetector.* Science in China Series G-Physics Mechanics & Astronomy, 2009. **52**(7): p. 969-977.
63. Guo, F., et al., *The theory and experiment of very-long-wavelength 256x1 GaAs/Al(x)Ga(1-x)As quantum well infrared detector linear arrays.* Science in China Series G-Physics Mechanics & Astronomy, 2008. **51**(7): p. 805-812.
64. Ganbold, T., et al., *Position-sensitive multi-wavelength photon detectors based on epitaxial InGaAs/InAlAs quantum wells.* Journal of Crystal Growth, 2015. **425**: p. 341-345.
65. Stiff-Roberts, A.D., *Quantum-dot infrared photodetectors: a review.* Journal of Nanophotonics, 2009. **3**.
66. Martyniuk, P. and A. Rogalski, *Quantum-dot infrared photodetectors: Status and outlook.* Progress in Quantum Electronics, 2008. **32**(3-4): p. 89-120.
67. Barve, A.V., et al., *Review of current progress in quantum dot infrared photodetectors.* Laser & Photonics Reviews, 2010. **4**(6): p. 738-750.
68. Barve, A.V., et al., *Confinement enhancing barriers for high performance quantum dots-in-a-well infrared detectors.* Applied Physics Letters, 2011. **99**(19).
69. Zavvari, M., *Quantum-dot-based single-photon avalanche detector for mid-infrared applications.* Journal of the Optical Society of America B-Optical Physics, 2015. **32**(5): p. 737-742.
70. Pal, D. and E. Towe, *Characteristics of high-operating-temperature InAs/GaAs quantum-dot infrared detectors.* Applied Physics Letters, 2006. **88**(15).
71. Chua, Y.C., et al., *Tuning In0.3Ga0.7As/GaAs multiple quantum dots for long-wavelength infrared detectors.* Applied Physics Letters, 2004. **85**(6): p. 1003-1005.
72. Pan, D., E. Towe, and S. Kennerly, *Photovoltaic quantum-dot infrared detectors.* Applied Physics Letters, 2000. **76**(22): p. 3301-3303.
73. Klin, O., et al., *A study of MBE growth-related defects in InAs/GaSb type-II supperlattices for long wavelength infrared detectors.* Journal of Crystal Growth, 2015. **425**: p. 54-59.
74. Malm, H., et al., *High image quality type-II superlattice detector for 3.3 mu M detection of volatile organic compounds.* Infrared Physics & Technology, 2015. **70**: p. 34-39.
75. Lv, Y.Q., et al., *Mid-wavelength focal plane arrays infrared detector based on type-II InAs/GaSb superlattice.* Optical and Quantum Electronics, 2015. **47**(7): p. 1731-1738.
76. Plis, E., et al., *Dual color longwave InAs/GaSb type-II strained layer superlattice detectors.* Infrared Physics & Technology, 2015. **70**: p. 93-98.

77. Zhang, L.X., et al., *Anodic fluoride passivation of type II InAs/GaSb superlattice for short-wavelength infrared detector.* Applied Physics a-Materials Science & Processing, 2015. **118**(2): p. 547-551.
78. Klipstein, P.C., et al. *Type-II superlattice detector for long-wave infrared imaging*. 2015.
79. Khoshakhlagh, A., et al., *High performance long-wave type-II superlattice infrared detectors.* Journal of Vacuum Science & Technology B, 2013. **31**(3).
80. Malm, H., et al., *High image quality type-II superlattice detector for 3.3 μm detection of volatile organic compounds.* Infrared Physics & Technology, 2015. **70**: p. 34-39.
81. Rehm, R., et al., *InAs/GaSb superlattice infrared detectors.* Infrared Physics & Technology, 2015. **70**: p. 87-92.
82. Khoshakhlagh, A., et al., *High performance long-wave type-II superlattice infrared detectors.* Journal of Vacuum Science & Technology B, 2013. **31**(3): p. 03C122.
83. Rehm, R., et al., *InAs/GaSb superlattice infrared detectors.* Infrared Physics & Technology, 2015. **70**: p. 87-92.
84. Perera, A.G.U., et al., *Demonstration of Si homojunction far-infrared detectors.* Applied Physics Letters, 1998. **72**(18): p. 2307-2309.
85. Eppeldauer, G.P., et al., *IR-enhanced Si reference detectors for one-step scale transfers from 300nm to 1000nm.* Metrologia, 2014. **51**(6): p. S252-S257.
86. Colace, L., et al., *Metal-semiconductor-metal near-infrared light detector based on epitaxial Ge/Si.* Applied Physics Letters, 1998. **72**(24): p. 3175-3177.
87. Sorianello, V., et al., *Thermal evaporation of Ge on Si for near infrared detectors: Material and device characterization.* Microelectronic Engineering, 2011. **88**(4): p. 526-529.
88. Jiang, R.L., et al., *Photoelectric properties of Si-Si1-xGex-Ge heterostructures for infrared detector.* Chinese Physics Letters, 1997. **14**(11): p. 876-878.
89. Park, J.S., R.P.G. Karunasiri, and K.L. Wang, *Normal Incidence Infrared Detector Using P-Type Sige Si Multiple Quantum-Wells.* Applied Physics Letters, 1992. **60**(1): p. 103-105.
90. Karunasiri, R.P.G., J.S. Park, and K.L. Wang, *Si1-Xgex/Si Multiple Quantum-Well Infrared Detector.* Applied Physics Letters, 1991. **59**(20): p. 2588-2590.
91. Jiang, R.L., et al., *SiGe/Ge heterojunction infrared detector.* Journal of Vacuum Science & Technology a-Vacuum Surfaces and Films, 1997. **15**(3): p. 968-970.
92. *Near-IR multi-quantum-well SiGe detectors show promise for photonics integration.* Laser Focus World, 2012. **48**(4): p. 13-13.
93. Mathews, J., et al., *Extended performance GeSn/Si(100) p-i-n photodetectors for full spectral range telecommunication applications.* Applied Physics Letters, 2009. **95**(13): p. 133506.
94. Werner, J., et al., *Germanium-tin p-i-n photodetectors integrated on silicon grown by molecular beam epitaxy.* Applied Physics Letters, 2011. **98**(6): p. 061108.
95. Su, S., et al., *GeSn p-i-n photodetector for all telecommunication bands detection.* Optics Express, 2011. **19**(7): p. 6400-6405.
96. Simon M. Sze, K.K.N., *Physics of Semiconductor Devices*. 2007: John Wiley & Sons.

97. Yuhua Cheng, C.H., *MOSFET Modeling & BSIM3 User's Guide*. 2002: Kluwer Academic
98. Feng, Q., et al. *Si and SiC power MOSFET characterization and comparison*. in *Transportation Electrification Asia-Pacific (ITEC Asia-Pacific), 2014 IEEE Conference and Expo*. 2014.
99. Fabre, J., P. Ladoux, and M. Piton, *Characterization and Implementation of Dual-SiC MOSFET Modules for Future Use in Traction Converters.* Ieee Transactions on Power Electronics, 2015. **30**(8): p. 4079-4090.
100. Nagaoka, K., et al., *High-speed gate drive circuit for SiC MOSFET by GaN HEMT.* Ieice Electronics Express, 2015. **12**(11).
101. Liu, C., et al., *Comparison of Switching Loss in GaN- and SiC-base IGBT and MOSFET: A Survey.* International Conference on Computer Science and Artificial Intelligence (Iccsai 2014), 2015: p. 174-177.
102. Ouaida, R., et al., *Gate Oxide Degradation of SiC MOSFET in Switching Conditions.* Ieee Electron Device Letters, 2014. **35**(12): p. 1284-1286.
103. Flicker, J.D., et al., *Progress in SiC MOSFET Reliability.* Gallium Nitride and Silicon Carbide Power Technologies 4, 2014. **64**(7): p. 87-98.
104. Qi, F., et al., *Si and SiC Power MOSFET Characterization and Comparison.* 2014 Ieee Transportation Electrification Conference and Expo (Itec) Asia-Pacific 2014, 2014.
105. Chiou, Y.-C., H.-Y. Chen, and C.-C. Huang, *The effect of Young's modulus of contact-etch-stop layer (CESL) stressor on the strained-Si MOSFET.* Physica Status Solidi a-Applications and Materials Science, 2012. **209**(10): p. 1950-1953.
106. Yan, R.H., A. Ourmazd, and K.F. Lee, *Scaling The Si Mosfet - From Bulk To Soi To Bulk.* Ieee Transactions on Electron Devices, 1992. **39**(7): p. 1704-1710.
107. Joodaki, M., *On the extraction of the external drain and source resistors and effective channel length in Si-MOSFET.* Solid-State Electronics, 2015. **111**: p. 1-6.
108. Chen, Y.H., S.J. Chang, and T.J. Hsueh, *Si-Based MOSFET and Thin Film Transistor Prepared via Hot Wire Implantation Doping Technique.* Ieee Electron Device Letters, 2015. **36**(2): p. 93-95.
109. Nakatsugawa, H., et al., *Self-cooling on power MOSFET using n-type Si wafer.* 9th European Conference on Thermoelectrics (Ect2011), 2012. **1449**: p. 548-551.
110. Avci, U.E., et al., *Energy Efficiency Comparison of Nanowire Heterojunction TFET and Si MOSFET at Lg=13nm, Including P-TFET and Variation Considerations.* 2013 Ieee International Electron Devices Meeting (Iedm), 2013.
111. Yu, H.-Y., et al., *p-Channel Ge MOSFET by Selectively Heteroepitaxially Grown Ge on Si.* Ieee Electron Device Letters, 2009. **30**(6): p. 675-677.
112. Fu, C.-H., et al., *Improved electrical characteristics and reliability of Ge MOSFET device with nitrided high-k gate dielectric by plasma immersion ion implantation.* Microelectronic Engineering, 2011. **88**(7): p. 1560-1563.
113. Kuzum, D., et al., *The Effect of Donor/Acceptor Nature of Interface Traps on Ge MOSFET Characteristics.* Ieee Transactions on Electron Devices, 2011. **58**(4): p. 1015-1022.
114. Yu, H.Y., et al., *p-Channel Ge MOSFET by Selectively Heteroepitaxially Grown Ge on Si.* Ieee Electron Device Letters, 2009. **30**(6): p. 675-677.

115. Wu, Y.H., et al., *Electrical Characteristics of Thermal-SiON-Gated Ge p-MOSFET Formed on Si Substrate.* Ieee Electron Device Letters, 2009. **30**(1): p. 72-74.
116. Xu, J.P., et al., *Improved electrical properties of Ge p-MOSFET with HfO2 gate dielectric by using TaOxNy interlayer.* Ieee Electron Device Letters, 2008. **29**(10): p. 1155-1158.
117. Zhang, Q.C., et al., *Drive-current enhancement in Ge n-channel MOSFET using laser annealing for source/drain activation.* Ieee Electron Device Letters, 2006. **27**(9): p. 728-730.
118. Krishnamohan, T., et al., *Low defect ultra-thin fully strained-Ge MOSFET on relaxed Si with high mobility and low band-to-band-tunneling (BTBT).* 2005 Symposium on VLSI Technology, Digest of Technical Papers. 2005. 82-83.
119. Kamata, Y., et al., *Dramatic improvement of Ge p-MOSFET characteristics realized by amorphous Zr-silicate/Ge gate stack with excellent structural stability through process temperatures*. Ieee International Electron Devices Meeting 2005, Technical Digest. 2005. 441-444.
120. Rahhal, L., et al., *Impact of Ge proportion on advanced SiGe bulk P-MOSFET matching performances.* Solid-State Electronics, 2013. **85**: p. 15-22.
121. Yang, Z., et al., *Effects of Ge fraction on electrical characteristics of strained Si1-xGex channel p-MOSFET.* Acta Physica Sinica, 2011. **60**(7).
122. Jiang, Y., et al., *Ge-rich (70%) SiGe nanowire MOSFET fabricated using pattern-dependent Ge-condensation technique.* Ieee Electron Device Letters, 2008. **29**(6): p. 595-598.
123. Lambert, A.D., et al., *Low frequency noise measurements of p-channel SI(1-x)GE(x) MOSFET's.* Ieee Transactions on Electron Devices, 1999. **46**(7): p. 1484-1486.
124. Jiang, Y., et al., *Omega-Gate p-MOSFET With Nanowirelike SiGe/Si Core/Shell Channel.* Ieee Electron Device Letters, 2009. **30**(4): p. 392-394.
125. Norris, D.J., et al., *Energy filtered TEM analyses of Ge snowploughing during oxidation of SiGe/Si MOSFET device structures*, in *Microscopy of Semiconducting Materials 2001*, A.G. Cullis and J.L. Hutchison, Editors. 2001. p. 185-188.
126. Hong, M., et al., *III-V metal-oxide-semiconductor field-effect transistors with high kappa dielectrics.* Japanese Journal of Applied Physics Part 1-Regular Papers Brief Communications & Review Papers, 2007. **46**(5B): p. 3167-3180.
127. Kwo, J. and M. Hong, *Research advances on III-V MOSFET electronics beyond Si CMOS.* Journal of Crystal Growth, 2009. **311**(7): p. 1944-1949.
128. Lu, L., et al., *Solid Phase Reactions of Ni-GaAs Alloys for High Mobility III-V MOSFET Applications.* Chinese Physics Letters, 2012. **29**(4).
129. Lee, C.-C., et al., *Impact of Strain Engineering on Nanoscale Strained In GaAs MOSFET Devices.* Journal of Nanoscience and Nanotechnology, 2011. **11**(7): p. 5623-5627.
130. Chin, H.-C., et al., *A New Silane-Ammonia Surface Passivation Technology for Realizing Inversion-Type Surface-Channel GaAs N-MOSFET with 160 nm Gate Length and High-Quality Metal-Gate/High-k Dielectric Stack*. Ieee International Electron Devices Meeting 2008, Technical Digest. 2008. 383-386.

131. Droopad, R., et al., *Development of GaAs-based MOSFET using molecular beam epitaxy.* Journal of Crystal Growth, 2007. **301**: p. 139-144.
132. Chin, H.-C., et al., *n-channel GaAs MOSFET with TaN/HfAlO gate stack formed using in situ vacuum anneal and silane passivation.* Journal of the Electrochemical Society, 2008. **155**(7): p. H464-H468.
133. Rajagopalan, K., et al., *Enhancement-mode GaAs n-channel MOSFET.* Ieee Electron Device Letters, 2006. **27**(12): p. 959-962.
134. Ye, P.D., et al., *GaAs MOSFET with oxide gate dielectric grown by atomic layer deposition.* Ieee Electron Device Letters, 2003. **24**(4): p. 209-211.
135. Lee, C.C., et al., *Impact of Strain Engineering on Nanoscale Strained In GaAs MOSFET Devices.* Journal of Nanoscience and Nanotechnology, 2011. **11**(7): p. 5623-5627.
136. Yokoyama, M., et al., *III-V/Ge High Mobility Channel Integration of InGaAs n-Channel and Ge p-Channel Metal-Oxide-Semiconductor Field-Effect Transistors with Self-Aligned Ni-Based Metal Source/Drain Using Direct Wafer Bonding.* Applied Physics Express, 2012. **5**(7).
137. Longo, P., et al., *A TEM nanoanalytical investigation of Pd/Ge ohmic contacts for the miniaturization and optimization of n-InGaAs MOSFET devices*, in *Electron Microscopy and Analysis Group Conference 2009*, R.T. Baker, Editor. 2010.
138. Adhikari, M.S. and Y. Singh, *High-performance dual-channel InGaAs MOSFET for small signal RF applications.* Electronics Letters, 2015. **51**(15): p. 1203-1204.
139. Vardi, A., et al., *InGaAs Double-Gate Fin-Sidewall MOSFET.* 2014 72nd Annual Device Research Conference (Drc), 2014: p. 219-220.
140. Alian, A., et al., *Impact of the channel thickness on the performance of ultrathin InGaAs channel MOSFET devices.* 2013 Ieee International Electron Devices Meeting (Iedm), 2013.
141. Zhang, X.G., et al., *In0.7Ga0.3As Channel n-MOSFET with Self-Aligned Ni-InGaAs Source and Drain.* Electrochemical and Solid State Letters, 2011. **14**(2): p. H60-H62.
142. Singisetti, U., et al., *InGaAs channel MOSFET with self-aligned source/drain MBE regrowth technology*, in *Physica Status Solidi C: Current Topics in Solid State Physics, Vol 6, No 6*, M. Walther, Editor. 2009. p. 1394-1398.
143. Lin, C.A., et al., *Depletion-mode In0.2Ga0.8As/GaAs MOSFET with molecular beam epitaxy grown Al2O3/Ga2O3(Gd2O3) as gate dielectrics.* Journal of Crystal Growth, 2009. **311**(7): p. 1954-1957.
144. *International Technology Roadmap for Semiconductors (ITRS).* 2013.
145. Suyog Gupta, B.M.-K., Yoshio Nishi, Krishna C Saraswat, *Band Structure and Ballistic Electron Transport Simulations in GeSn Alloys.* Proc. Simul. Semicond. Processes Devices.
146. Han, G., et al., *High-Mobility Germanium-Tin (GeSn) P-channel MOSFETs Featuring Metallic Source/Drain and Sub-370 degrees C Process Modules.* 2011 Ieee International Electron Devices Meeting (Iedm), 2011.
147. Grätzel, M., *Dye-sensitized solar cells.* Journal of Photochemistry and Photobiology C: Photochemistry Reviews, 2003. **4**(2): p. 145-153.

148. O'Regan, B. and M. Gratzel, *A low-cost, high-efficiency solar cell based on dye-sensitized colloidal TiO2 films.* Nature, 1991. **353**(6346): p. 737-740.
149. Jena, A., et al., *Dye Sensitized Solar Cells: A Review.* Transactions of the Indian Ceramic Society, 2012. **71**(1): p. 1-16.
150. Mehmood, U., et al., *Recent Advances in Dye Sensitized Solar Cells.* Advances in Materials Science and Engineering, 2014.
151. Arjunan, T.V. and T.S. Senthil, *Review: Dye sensitised solar cells.* Materials Technology, 2013. **28**(1-2): p. 9-14.
152. Su'ait, M.S., M.Y.A. Rahman, and A. Ahmad, *Review on polymer electrolyte in dye-sensitized solar cells (DSSCs).* Solar Energy, 2015. **115**: p. 452-470.
153. Rahman, M.Y.A., et al., *Polymer electrolyte for photoelectrochemical cell and dye-sensitized solar cell: a brief review.* Ionics, 2014. **20**(9): p. 1201-1205.
154. Ileperuma, O.A., *Gel polymer electrolytes for dye sensitised solar cells: a review.* Materials Technology, 2013. **28**(1-2): p. 65-70.
155. Qu, J. and C. Lai, *One-Dimensional TiO2 Nanostructures as Photoanodes for Dye-Sensitized Solar Cells.* Journal of Nanomaterials, 2013.
156. Batmunkh, M., M.J. Biggs, and J.G. Shapter, *Carbon Nanotubes for Dye-Sensitized Solar Cells.* Small, 2015. **11**(25): p. 2963-2989.
157. Calogero, G., et al., *Vegetable-based dye-sensitized solar cells.* Chemical Society Reviews, 2015. **44**(10): p. 3244-3294.
158. Suzuki, Y., Y. Okamoto, and N. Ishii, *Dye-sensitized solar cells using double-oxide electrodes: a brief review.* Tunisia-Japan Symposium: R&D of Energy and Material Sciences for Sustainable Society, 2015. **596**.
159. Weerasinghe, H.C., F. Huang, and Y.-B. Cheng, *Fabrication of flexible dye sensitized solar cells on plastic substrates.* Nano Energy, 2013. **2**(2): p. 174-189.
160. Wei, W., H. Wang, and Y.H. Hu, *A review on PEDOT-based counter electrodes for dye-sensitized solar cells.* International Journal of Energy Research, 2014. **38**(9): p. 1099-1111.
161. Roy-Mayhew, J.D. and I.A. Aksay, *Graphene Materials and Their Use in Dye-Sensitized Solar Cells.* Chemical Reviews, 2014. **114**(12): p. 6323-6348.
162. Macaira, J., L. Andrade, and A. Mendes, *Review on nanostructured photoelectrodes for next generation dye-sensitized solar cells.* Renewable & Sustainable Energy Reviews, 2013. **27**: p. 334-349.
163. Prakash, T., *Review on Nanostructured Semiconductors for Dye Sensitized Solar Cells.* Electronic Materials Letters, 2012. **8**(3): p. 231-243.
164. Uzaki, K., et al., *Dye-Sensitized Solar Cells Consisting of 3D-Electrodes-A Review: Aiming at High Efficiency From the View Point of Light Harvesting and Charge Collection.* Journal of Solar Energy Engineering-Transactions of the Asme, 2010. **132**(2).
165. Ma, J., et al., *Light reharvesting and enhanced efficiency of dye-sensitized solar cells based 3D-CNT/graphene counter electrodes.* Journal of Materials Chemistry A, 2015. **3**(23): p. 12307-12313.

166. Cho, C.-Y., H.-N. Kim, and J.H. Moon, *Characterization of charge transport properties of a 3D electrode for dye-sensitized solar cells.* Physical Chemistry Chemical Physics, 2013. **15**(26): p. 10835-10840.
167. Lim, C.K., et al., *Enhanced Photovoltaic Performance of Dye-Sensitized Solar Cell Using Composite Photoanode on 3D Electrode.* Micro/Nano Materials, Devices, and Systems, 2013. **8923**.
168. Burschka, J., et al., *Sequential deposition as a route to high-performance perovskite-sensitized solar cells.* Nature, 2013. **499**(7458): p. 316-319.
169. Mathew, S., et al., *Dye-sensitized solar cells with 13% efficiency achieved through the molecular engineering of porphyrin sensitizers.* Nat Chem, 2014. **6**(3): p. 242-247.
170. Kojima, A., et al., *Organometal Halide Perovskites as Visible-Light Sensitizers for Photovoltaic Cells.* Journal of the American Chemical Society, 2009. **131**(17): p. 6050-6051.
171. Kim, H.-S., et al., *Lead Iodide Perovskite Sensitized All-Solid-State Submicron Thin Film Mesoscopic Solar Cell with Efficiency Exceeding 9%.* Scientific Reports, 2012. **2**: p. 591.
172. Liu, M., M.B. Johnston, and H.J. Snaith, *Efficient planar heterojunction perovskite solar cells by vapour deposition.* Nature, 2013. **501**(7467): p. 395-398.
173. Lee, M.M., et al., *Efficient Hybrid Solar Cells Based on Meso-Superstructured Organometal Halide Perovskites.* Science, 2012. **338**(6107): p. 643-647.
174. Ball, J.M., et al., *Low-temperature processed meso-superstructured to thin-film perovskite solar cells.* Energy & Environmental Science, 2013. **6**(6): p. 1739-1743.
175. Eperon, G.E., et al., *Morphological Control for High Performance, Solution-Processed Planar Heterojunction Perovskite Solar Cells.* Advanced Functional Materials, 2014. **24**(1): p. 151-157.
176. Saliba, M., et al., *Influence of Thermal Processing Protocol upon the Crystallization and Photovoltaic Performance of Organic–Inorganic Lead Trihalide Perovskites.* The Journal of Physical Chemistry C, 2014. **118**(30): p. 17171-17177.
177. Jung, H.S. and N.-G. Park, *Perovskite Solar Cells: From Materials to Devices.* Small, 2015. **11**(1): p. 10-25.
178. Yang, Y. and W. Wang, *Effects of incorporating PbS quantum dots in perovskite solar cells based on CH3NH3PbI3.* Journal of Power Sources, 2015. **293**: p. 577-584.
179. Lv, M., et al., *Colloidal CuInS2 Quantum Dots as Inorganic Hole-Transporting Material in Perovskite Solar Cells.* Acs Applied Materials & Interfaces, 2015. **7**(31): p. 17482-17488.
180. Chen, L.-C., et al., *Fabrication and Properties of High-Efficiency Perovskite/PCBM Organic Solar Cells.* Nanoscale research letters, 2015. **10**(1): p. 1020-1020.
181. Gratia, P., et al., *Frontispiece: A Methoxydiphenylamine-Substituted Carbazole Twin Derivative: An Efficient Hole-Transporting Material for Perovskite Solar Cells.* Angewandte Chemie (International ed. in English), 2015. **54**(39).
182. Li, Z., *Stable Perovskite Solar Cells Based on WO3 Nanocrystals as Hole Transport Layer.* Chemistry Letters, 2015. **44**(8): p. 1140-1141.

183. Cao, J., et al., *Well-Defined Thiolated Nanographene as Hole-Transporting Material for Efficient and Stable Perovskite Solar Cells.* Journal of the American Chemical Society, 2015. **137**(34): p. 10914-10917.
184. Han, G.S., et al., *Epitaxial 1D electron transport layers for high-performance perovskite solar cells.* Nanoscale, 2015. **7**(37): p. 15284-90.
185. Gu, Z., et al., *Novel planar heterostructure perovskite solar cells with CdS nanorods array as electron transport layer.* Solar Energy Materials and Solar Cells, 2015. **140**: p. 396-404.
186. Tao, H., et al., *Perovskite solar cell based on network nanoporous layer consisted of TiO2 nanowires and its interface optimization.* Journal of Power Sources, 2015. **290**: p. 144-152.
187. Zhang, J. and T. Pauporte, *One-Dimensional Self-Standing TiO2 Nanotube Array Layers Designed for Perovskite Solar Cell Applications.* Chemphyschem, 2015. **16**(13): p. 2836-2841.
188. Yang, W.S., et al., *High-performance photovoltaic perovskite layers fabricated through intramolecular exchange.* Science, 2015. **348**(6240): p. 1234-1237.
189. Bera, D., et al., *Quantum Dots and Their Multimodal Applications: A Review.* Materials, 2010. **3**(4): p. 2260.
190. Luis M. Liz-Marzán, P.V.K., *Nanoscale Materials*. 2003: Springer.
191. Jun-Jie Zhu, J.-J.L., Hai-Ping Huang, Fang-Fang Cheng, *Quantum Dots for DNA Biosensing*. 2013: Sptinger.
192. Ekimov A. I., O.A.A., *Quantum size effect in three-dimensional microscopic semiconductor crystals.* JETP Lett, 1981. **34**(6): p. 345.
193. Rossetti, R. and L. Brus, *Electron-hole recombination emission as a probe of surface chemistry in aqueous cadmium sulfide colloids.* The Journal of Physical Chemistry, 1982. **86**(23): p. 4470-4472.
194. Pisanic, T.R., II, Y. Zhang, and T.H. Wang, *Quantum dots in diagnostics and detection: principles and paradigms.* Analyst, 2014. **139**(12): p. 2968-2981.
195. Kumar, C.S.S.R., *Semiconductor Nanomaterials*. 2010: John Wiley & Sons.
196. Vasudevan, D., et al., *Core–shell quantum dots: Properties and applications.* Journal of Alloys and Compounds, 2015. **636**: p. 395-404.
197. Rawalekar, S., M.V.N. Raj, and H.N. Ghosh, *Synthesis and Optical Properties of Type I CdSe/ZnSe Core-Shell Quantum Dot.* Science of Advanced Materials, 2012. **4**(5-6): p. 637-642.
198. Acharya, K.P., et al., *Elucidation of Two Giants: Challenges to Thick-Shell Synthesis in CdSe/ZnSe and ZnSe/CdS Core/Shell Quantum Dots.* Journal of the American Chemical Society, 2015. **137**(11): p. 3755-3758.
199. Kwon, Y.-T., et al., *Synthesis of CdSe/ZnSe quantum dots passivated with a polymer for oxidation prevention.* Surface & Coatings Technology, 2014. **259**: p. 83-86.
200. Suganthi, A.R.B., P. Sagayaraj, and Ieee, *Investigation on the Facile Methods for the Synthesis and Characterization of CdSe/ZnSe Core/Shell Nanocomposites*. 2013 International Conference on Advanced Nanomaterials and Emerging Engineering Technologies. 2013. 530-531.

201. Tripathi, S.K. and M. Sharma, *Synthesis and optical study of green light emitting polymer coated CdSe/ZnSe core/shell nanocrystals.* Materials Research Bulletin, 2013. **48**(5): p. 1837-1844.
202. Liu, L.-w., et al., *Optimizing the synthesis of CdS/ZnS core/shell semiconductor nanocrystals for bioimaging applications.* Beilstein Journal of Nanotechnology, 2014. **5**: p. 919-926.
203. Xuan, T.-T., et al., *Microwave-Assisted Synthesis of CdS/ZnS:Cu Quantum Dots for White Light-Emitting Diodes with High Color Rendition.* Chemistry of Materials, 2015. **27**(4): p. 1187-1193.
204. Zhai, X., et al., *Shape-Controlled CdS/ZnS Core/Shell Heterostructured Nanocrystals: Synthesis, Characterization, and Periodic DFT Calculations.* Crystal Growth & Design, 2015. **15**(3): p. 1344-1350.
205. Li, L. and P. Reiss, *One-pot synthesis of highly luminescent InP/ZnS nanocrystals without precursor injection.* Journal of the American Chemical Society, 2008. **130**(35): p. 11588-+.
206. Lim, K., H.S. Jang, and K. Woo, *Synthesis of blue emitting InP/ZnS quantum dots through control of competition between etching and growth.* Nanotechnology, 2012. **23**(48).
207. Massadeh, S., S. Xu, and T. Nann, *Synthesis and Exploitation of InP/ZnS Quantum Dots for Bioimaging.* Colloidal Quantum Dots for Biomedical Applications Iv, 2009. **7189**.
208. Ryu, E., et al., *Step-Wise Synthesis of InP/ZnS Core-Shell Quantum Dots and the Role of Zinc Acetate.* Chemistry of Materials, 2009. **21**(4): p. 573-575.
209. Xu, S., J. Ziegler, and T. Nann, *Rapid synthesis of highly luminescent InP and InP/ZnS nanocrystals.* Journal of Materials Chemistry, 2008. **18**(23): p. 2653-2656.
210. Cingarapu, S., et al., *Synthesis of CdSe/ZnS and CdTe/ZnS Quantum Dots: Refined Digestive Ripening.* Journal of Nanomaterials, 2012.
211. Duran, G.M., et al., *Microwave-assisted synthesis of water soluble thiol capped CdSe/ZnS quantum dots and its interaction with sulfonylurea herbicides.* Journal of Colloid and Interface Science, 2014. **428**: p. 235-241.
212. McConnachie, L.A., et al., *The Glutathione Synthesis Gene Gclm Modulates Amphiphilic Polymer-Coated CdSe/ZnS Quantum Dot-Induced Lung Inflammation in Mice.* Plos One, 2013. **8**(5).
213. Zheng, H., L.J. Mortensen, and L.A. DeLouise, *Thiol Antioxidant-Functionalized CdSe/ZnS Quantum Dots: Synthesis, Characterization, Cytotoxicity.* Journal of Biomedical Nanotechnology, 2013. **9**(3): p. 382-392.
214. Zhu, H., et al., *Synthesis and Optical Properties of Thiol Functionalized CdSe/ZnS (Core/Shell) Quantum Dots by Ligand Exchange.* Journal of Nanomaterials, 2014.
215. Shu, C., et al., *Facile synthesis and characterization of water soluble ZnSe/ZnS quantum dots for cellar imaging.* Spectrochimica Acta Part a-Molecular and Biomolecular Spectroscopy, 2013. **104**: p. 143-149.
216. Xu, S., Y. Cui, and Cie, *Synthesis Of Nontoxic White Light Znse/Zns/Mns Quantum Dots.* Proceedings of Cie 2012 Lighting Quality and Energy Efficiency, 2012: p. 570-570.

217. Zhang, J., et al., *Microwave-assisted aqueous synthesis of transition metal ions doped ZnSe/ZnS core/shell quantum dots with tunable white-light emission.* Applied Surface Science, 2015. **351**: p. 655-661.
218. Zhang, X., et al., *Low temperature aqueous phase synthesis and optical property study of ZnSe/ZnS core/shell quantum dots.* Optoelectronics and Advanced Materials-Rapid Communications, 2015. **9**(7-8): p. 924-929.
219. Zhao, D., et al., *Facile synthesis and characterization of highly luminescent UV-blue-emitting ZnSe/ZnS quantum dots via a one-step hydrothermal method.* Rsc Advances, 2014. **4**(87): p. 47005-47011.
220. Lee, D.U., et al., *Optical and electronic properties of type-II CdSe/CdS core-shell quantum dots.* Applied Physics Express, 2015. **8**(6).
221. Sugunan, A., et al., *Synthesis of tetrahedral quasi-type-II CdSe-CdS core-shell quantum dots.* Nanotechnology, 2011. **22**(42).
222. Cao, C., et al., *Synthesis and characterization of TiO2/CdS core-shell nanorod arrays and their photoelectrochemical property.* Journal of Alloys and Compounds, 2012. **523**: p. 139-145.
223. Mazumdar, S. and A.J. Bhattacharyya, *One-pot synthesis of a TiO2-CdS nano-heterostructure assembly with enhanced photocatalytic activity.* Rsc Advances, 2015. **5**(44): p. 34942-34948.
224. Danek, M., et al., *Synthesis of luminescent thin-film CdSe/ZnSe quantum dot composites using CdSe quantum dots passivated with an overlayer of ZnSe.* Chemistry of Materials, 1996. **8**(1): p. 173-180.
225. Taniguchi, S., et al., *The one-pot synthesis of core/shell/shell CdTe/CdSe/ZnSe quantum dots in aqueous media for in vivo deep tissue imaging.* Journal of Materials Chemistry, 2011. **21**(9): p. 2877-2882.
226. Zhang, W., et al., *Design and Synthesis of Highly Luminescent Near-Infrared-Emitting Water-Soluble CdTe/CdSe/ZnS Core/Shell/Shell Quantum Dots.* Inorganic Chemistry, 2009. **48**(20): p. 9723-9731.
227. Kim, S., et al., *Type-II quantum dots: CdTe/CdSe(core/shell) and CdSe/ZinTe(core/shell) heterostructures.* Journal of the American Chemical Society, 2003. **125**(38): p. 11466-11467.
228. Wang, J., et al., *Core/Shell Colloidal Quantum Dot Exciplex States for the Development of Highly Efficient Quantum-Dot-Sensitized Solar Cells.* Journal of the American Chemical Society, 2013. **135**(42): p. 15913-15922.
229. Schops, O., et al., *Recombination dynamics of CdTe/CdS core-shell nanocrystals.* Journal of Physical Chemistry B, 2006. **110**(5): p. 2074-2079.
230. Arivarasan, A., G. Sasikala, and R. Jayavel, *In situ synthesis of CdTe:CdS quantum dot nanocomposites for photovoltaic applications.* Materials Science in Semiconductor Processing, 2014. **25**: p. 238-243.
231. Ma, Y., Y. Li, and X. Zhong, *Facile synthesis of high-quality CdTe/CdS core/shell quantum dots in aqueous phase by using dual capping ligands.* Rsc Advances, 2014. **4**(85): p. 45473-45480.
232. Wei, F., et al., *Synthesis of highly luminescent CdTe/CdS/ZnS quantum dots by a one-pot capping method.* Chemical Engineering Journal, 2013. **226**: p. 416-422.

233. DeGroot, M.W., N.J. Taylor, and J.F. Corrigan, *Molecular nanocluster analogues of CdSe/ZnSe and CdTe/ZnTe core/shell nanoparticles.* Journal of Materials Chemistry, 2004. **14**(4): p. 654-660.
234. Cheng, C.T., et al., *Syntheses and photophysical properties of type-II CdSe/ZnTe/ZnS (core/shell/shell) quantum dots.* Journal of Materials Chemistry, 2005. **15**(33): p. 3409-3414.
235. Xie, R.G., X.H. Zhong, and T. Basche, *Synthesis, characterization, and spectroscopy of type-II core/shell semiconductor nanocrystals with ZnTe cores.* Advanced Materials, 2005. **17**(22): p. 2741-+.
236. Jiao, S., et al., *Band Engineering in Core/Shell ZnTe/CdSe for Photovoltage and Efficiency Enhancement in Exciplex Quantum Dot Sensitized Solar Cells.* Acs Nano, 2015. **9**(1): p. 908-915.
237. Pan, Z., et al., *Highly Efficient Inverted Type-I CdS/CdSe Core/Shell Structure QD-Sensitized Solar Cells.* Acs Nano, 2012. **6**(5): p. 3982-3991.
238. Goswami, Y.C., et al., *Synthesis of CdS/CdSe Core/Shell Ultra small Nanostructures Using New Microwave Assisted Ultrasonic Sol Gel Route.* Solid State Physics: Proceedings of the 58th Dae Solid State Physics Symposium 2013, Pts a & B, 2014. **1591**: p. 414-416.
239. Ivanov, S.A., et al., *Type-II core/shell CdS/ZnSe nanocrystals: Synthesis, electronic structures, and spectroscopic properties.* Journal of the American Chemical Society, 2007. **129**(38): p. 11708-11719.
240. Nemchinov, A., et al., *Synthesis and characterization of type IIZnSe/CdS core/shell nanocrystals.* Journal of Physical Chemistry C, 2008. **112**(25): p. 9301-9307.
241. Qiu, X.K., et al., *ZnO/CdS/CdSe core/double shell nanorod arrays derived by a successive ionic layer adsorption and reaction process for quantum dot-sensitized solar cells.* Semiconductor Science and Technology, 2011. **26**(9).
242. Wang, Y., et al., *Stimulated Emission and Lasing from CdSe/CdS/ZnS Core-Multi-Shell Quantum Dots by Simultaneous Three-Photon Absorption.* Advanced Materials, 2014. **26**(18): p. 2954-2961.
243. Raj, S., et al., *Formation of core@multi-shell CdSe@CdZnS-ZnS quantum dot heterostructure films by pulse electrophoresis deposition.* Superlattices and Microstructures, 2015. **83**: p. 618-626.
244. Xu, S.C., et al., *Luminescent CdTe/CdS core-shell and CdTe/CdS/ZnS multi-layer quantum dots: synthesis and investigations for bioapplication - art. no. 68310U*, in *Nanophotonics, Nanostructure, and Nanometrology Ii*, X. Zhu, S.Y. Chou, and Y. Arakawa, Editors. 2008. p. U8310-U8310.
245. Boldt, K., et al., *Controlling Charge Carrier Overlap in Type-II ZnSe/ZnS/CdS Core-Barrier-Shell Quantum Dots.* Journal of Physical Chemistry Letters, 2015. **6**(13): p. 2590-2597.
246. Jasmine, P.C.L., A.J. Peter, and C.W. Lee, *Intersubband optical transition energy in a CdTe/Zn0.2Cd0.8Te/ZnTe core/shell/shell spherical quantum dot with Smorodinsky-Winternitz confinement potential.* Chemical Physics, 2015. **452**: p. 40-45.

247. Zhou, H.F., et al., *Wide emission-tunable CdTeSe/ZnSe/ZnS core-shell quantum dots and their conjugation with E. coli O-157.* Materials Research Bulletin, 2015. **65**: p. 53-60.
248. Xie, W.F., *Photoionization and third-order susceptibility of a neutral donor in ZnS/InP/ZnSe core/shell spherical quantum dots.* Physica B-Condensed Matter, 2014. **449**: p. 57-60.
249. Adegoke, O., T. Nyokong, and P.B.C. Forbes, *Structural and optical properties of alloyed quaternary CdSeTeS core and CdSeTeS/ZnS core–shell quantum dots.* Journal of Alloys and Compounds, 2015. **645**: p. 443-449.
250. Maity, P., T. Debnath, and H.N. Ghosh, *Slow Electron Cooling Dynamics Mediated by Electron Hole Decoupling in Highly Luminescent CdSxSe1-x Alloy Quantum Dots.* Journal of Physical Chemistry C, 2015. **119**(19): p. 10785-10792.
251. Cheng, J.W., et al., *Aqueous synthesis of high-fluorescence CdZnTe alloyed quantum dots.* Journal of Alloys and Compounds, 2014. **589**: p. 539-544.
252. Wei, H.Y., et al., *Investigation on Interfacial Charge Transfer Process in CdSexTe1-x Alloyed Quantum Dot Sensitized Solar Cells.* Electrochimica Acta, 2015. **173**: p. 156-163.
253. Yahia-Ammar, A., et al., *Thin-coated water soluble CdTeS alloyed quantum dots as energy donors for highly efficient FRET.* Dalton Transactions, 2014. **43**(41): p. 15583-15592.
254. Maity, P., T. Debnath, and H.N. Ghosh, *Slow Electron Cooling Dynamics of Highly Luminescent CdSxSe1-x Alloy Quantum Dot*, in *Ultrafast Phenomena Xix*, I. Yamanouchi, et al., Editors. 2015. p. 275-278.
255. Kim, T., et al., *Large-Scale Synthesis of InPZnS Alloy Quantum Dots with Dodecanethiol as a Composition Controller.* The Journal of Physical Chemistry Letters, 2012. **3**(2): p. 214-218.
256. Adegoke, O., T. Nyokong, and P.B.C. Forbes, *Structural and optical properties of alloyed quaternary CdSeTeS core and CdSeTeS/ZnS core-shell quantum dots.* Journal of Alloys and Compounds, 2015. **645**: p. 443-449.
257. Kershaw, S.V., et al., *Multiple exciton generation in cluster-free alloy CdxHg1-xTe colloidal quantum dots synthesized in water.* Physical Chemistry Chemical Physics, 2014. **16**(47): p. 25710-25722.
258. Siffalovic, P., et al., *Evaluation of low-cadmium ZnCdSeS alloyed quantum dots for remote phosphor solid-state lighting technology.* Applied Optics, 2015. **54**(23): p. 7094-7098.
259. Wang, Y., et al., *Quaternary Alloy Quantum Dots: Toward Low-Threshold Stimulated Emission and All-Solution-Processed Lasers in the Green Region.* Advanced Optical Materials, 2015. **3**(5): p. 652-657.
260. Yu-Jen, S. and L. Yuh-Lang, *Assembly of CdS quantum dots onto mesoscopic TiO 2 films for quantum dot-sensitized solar cell applications.* Nanotechnology, 2008. **19**(4): p. 045602.
261. Jun, H.K., M.A. Careem, and A.K. Arof, *Quantum dot-sensitized solar cells—perspective and recent developments: A review of Cd chalcogenide quantum dots as sensitizers.* Renewable and Sustainable Energy Reviews, 2013. **22**: p. 148-167.

262. Hanna, M.C. and A.J. Nozik, *Solar conversion efficiency of photovoltaic and photoelectrolysis cells with carrier multiplication absorbers.* Journal of Applied Physics, 2006. **100**(7): p. 074510.
263. Ellingson, R.J., et al., *Highly Efficient Multiple Exciton Generation in Colloidal PbSe and PbS Quantum Dots.* Nano Letters, 2005. **5**(5): p. 865-871.
264. Flory, F., L. Escoubas, and G. Berginc, *Optical properties of nanostructured materials: a review.* Journal of Nanophotonics, 2011. **5**(1): p. 052502-052502-20.
265. Nozik, A.J., *Quantum dot solar cells.* Physica E: Low-dimensional Systems and Nanostructures, 2002. **14**(1–2): p. 115-120.
266. Beard, M.C., *Multiple Exciton Generation in Semiconductor Quantum Dots.* The Journal of Physical Chemistry Letters, 2011. **2**(11): p. 1282-1288.
267. Semonin, O.E., et al., *Peak External Photocurrent Quantum Efficiency Exceeding 100% via MEG in a Quantum Dot Solar Cell.* Science, 2011. **334**(6062): p. 1530-1533.
268. Htoon, H., et al., *Highly Emissive Multiexcitons in Steady-State Photoluminescence of Individual "Giant" CdSe/CdS Core/Shell Nanocrystals.* Nano Letters, 2010. **10**(7): p. 2401-2407.
269. Nozik, A.J., *Exciton Multiplication and Relaxation Dynamics in Quantum Dots: Applications to Ultrahigh-Efficiency Solar Photon Conversion†.* Inorganic Chemistry, 2005. **44**(20): p. 6893-6899.
270. Nozik, A.J., et al., *Semiconductor Quantum Dots and Quantum Dot Arrays and Applications of Multiple Exciton Generation to Third-Generation Photovoltaic Solar Cells.* Chemical Reviews, 2010. **110**(11): p. 6873-6890.
271. Schaller, R.D. and V.I. Klimov, *High Efficiency Carrier Multiplication in PbSe Nanocrystals: Implications for Solar Energy Conversion.* Physical Review Letters, 2004. **92**(18): p. 186601.
272. Schaller, R.D. and V.I. Klimov, *High efficiency carrier multiplication in PbSe nanocrystals: Implications for solar energy conversion.* Physical Review Letters, 2004. **92**(18).
273. Gratzel, M., *Photoelectrochemical cells.* Nature, 2001. **414**(6861): p. 338-344.
274. Thambidurai, M., et al., *Strong quantum confinement effect in nanocrystalline CdS.* Journal of Materials Science, 2010. **45**(12): p. 3254-3258.
275. Haug, H. and S.W. Koch, *Quantum Theory of the Optical and Electronic Properties of Semiconductors*. 2004: World Scientific.
276. Baskoutas, S. and A.F. Terzis, *Size-dependent band gap of colloidal quantum dots.* Journal of Applied Physics, 2006. **99**(1).
277. Baskoutas, S., A.F. Terzis, and W. Schommers, *Size-dependent exciton energy of narrow band gap colloidal quantum dots in the finite depth square-well effective mass approximation.* Journal of Computational and Theoretical Nanoscience, 2006. **3**(2): p. 269-271.
278. Cho, E., et al., *Modeling on the size dependent properties of InP quantum dots: a hybrid functional study.* Nanotechnology, 2013. **24**(21).
279. Segets, D., et al., *Determination of the Quantum Dot Band Gap Dependence on Particle Size from Optical Absorbance and Transmission Electron Microscopy Measurements.* ACS Nano, 2012. **6**(10): p. 9021-9032.

280. Jara, D.H., et al., *Size-Dependent Photovoltaic Performance of CuInS2 Quantum Dot-Sensitized Solar Cells.* Chemistry of Materials, 2014. **26**(24): p. 7221-7228.
281. Ho, M.Q., et al., *Size-Dependent Optical Properties of Luminescent Zn3P2 Quantum Dots.* Journal of Physical Chemistry C, 2015. **119**(19): p. 10576-10584.
282. Keuleyan, S.E., et al., *Mercury Telluride Colloidal Quantum Dots: Electronic Structure, Size-Dependent Spectra, and Photocurrent Detection up to 12 mu m.* Acs Nano, 2014. **8**(8): p. 8676-8682.
283. Lekha, P., et al., *Size dependent electron transfer from CdTe quantum dots linked to TiO2 thin films in quantum dot sensitized solar cells.* Materials Chemistry and Physics, 2013. **141**(1): p. 216-222.
284. Salini, K., K.S. Rahul, and V. Mathew, *Size-dependent electronic and optical properties of an exciton in CdSe/CdS/CdSe/CdS multilayer spherical quantum dot.* Applied Physics a-Materials Science & Processing, 2014. **116**(3): p. 1371-1377.
285. Zhu, D.-H., et al., *Size-Dependent Electron Injection and Photoelectronic Properties of CuInS2 Quantum Dot Sensitized Solar Cells.* Acta Physico-Chimica Sinica, 2014. **30**(10): p. 1861-1866.
286. Neeleshwar, S., et al., *Size-dependent properties of CdSe quantum dots.* Physical Review B, 2005. **71**(20).
287. Vogel, R., P. Hoyer, and H. Weller, *Quantum-Sized Pbs, Cds, Ag2s, Sb2s3, And Bi2s3 Particles As Sensitizers For Various Nanoporous Wide-Bandgap Semiconductors.* Journal of Physical Chemistry, 1994. **98**(12): p. 3183-3188.
288. Gorer, S. and G. Hodes, *Quantum size effects in the study of chemical solution deposition mechanisms of semiconductor films.* The Journal of Physical Chemistry, 1994. **98**(20): p. 5338-5346.
289. Ying, E., et al., *Synthesis and Bio-Imaging Application of Highly Luminescent Mercaptosuccinic Acid-Coated CdTe Nanocrystals.* PLoS ONE, 2008. **3**(5): p. e2222.
290. Duan, J.L., et al., *Recent advances in critical materials for quantum dot-sensitized solar cells: a review.* Journal of Materials Chemistry A, 2015. **3**(34): p. 17497-17510.
291. Tian, J. and G. Cao, *Semiconductor quantum dot-sensitized solar cells.* Nano reviews, 2013. **4**.
292. Ruhle, S., M. Shalom, and A. Zaban, *Quantum-Dot-Sensitized Solar Cells.* Chemphyschem, 2010. **11**(11): p. 2290-2304.
293. Wang, Z.L. and W. Wu, *Nanotechnology-Enabled Energy Harvesting for Self-Powered Micro-/Nanosystems.* Angewandte Chemie International Edition, 2012. **51**(47): p. 11700-11721.
294. Tian, J. and G. Cao, *Semiconductor quantum dot-sensitized solar cells.* Nano Reviews, 2013. **4**: p. 10.3402/nano.v4i0.22578.
295. Lin, S.-C., et al., *Quantum-dot-sensitized solar cells: Assembly of CdS-quantum-dots coupling techniques of self-assembled monolayer and chemical bath deposition.* Applied Physics Letters, 2007. **90**(14): p. 143517.
296. Yang, Z., et al., *Quantum dot-sensitized solar cells incorporating nanomaterials.* Chemical Communications, 2011. **47**(34): p. 9561-9571.
297. El Chaar, L., L.A. lamont, and N. El Zein, *Review of photovoltaic technologies.* Renewable and Sustainable Energy Reviews, 2011. **15**(5): p. 2165-2175.

298. Yasuo, C., et al., *Dye-Sensitized Solar Cells with Conversion Efficiency of 11.1%.* Japanese Journal of Applied Physics, 2006. **45**(7L): p. L638.
299. Grätzel, M., *Solar Energy Conversion by Dye-Sensitized Photovoltaic Cells.* Inorganic Chemistry, 2005. **44**(20): p. 6841-6851.
300. Huang, J., et al., *Improved Performance of Colloidal CdSe Quantum Dot-Sensitized Solar Cells by Hybrid Passivation.* ACS Applied Materials & Interfaces, 2014. **6**(21): p. 18808-18815.
301. Mora-Seró, I., et al., *Recombination in Quantum Dot Sensitized Solar Cells.* Accounts of Chemical Research, 2009. **42**(11): p. 1848-1857.
302. 김현주, L.D. Yoon, and S. Jae-Sung, *Luminescence Properties of Ag Doped ZnO as Quantum Dot Materials for Improving Efficiency of Dye-sensitized Solar Cell.* Journal of the Korean Institute of Electrical and Electronic Material Engineers, 2004. **17**(9): p. 988-993.
303. Wijayantha, K.G.U., L.M. Peter, and L.C. Otley, *Fabrication of CdS quantum dot sensitized solar cells via a pressing route.* Solar Energy Materials and Solar Cells, 2004. **83**(4): p. 363-369.
304. Duan, J., et al., *Recent advances in critical materials for quantum dot-sensitized solar cells: a review.* Journal of Materials Chemistry A, 2015. **3**(34): p. 17497-17510.
305. Carey, G.H., et al., *Record Charge Carrier Diffusion Length in Colloidal Quantum Dot Solids via Mutual Dot-To-Dot Surface Passivation.* Advanced Materials, 2015. **27**(21): p. 3325-3330.
306. Zhao, K., et al., *Boosting Power Conversion Efficiencies of Quantum-Dot-Sensitized Solar Cells Beyond 8% by Recombination Control.* Journal of the American Chemical Society, 2015. **137**(16): p. 5602-5609.
307. Mousavi-Kamazani, M., et al., *Synthesis and characterization of CuInS2 quantum dot in the presence of novel precursors and its application in dyes solar cells.* Materials Letters, 2015. **145**: p. 99-103.
308. Hu, X., et al., *Aqueous colloidal CuInS2 for quantum dot sensitized solar cells.* Journal of Materials Chemistry, 2011. **21**(40): p. 15903-15905.
309. Peng, Z., et al., *ZnSe passivation layer for the efficiency enhancement of CuInS2 quantum dots sensitized solar cells.* Journal of Alloys and Compounds, 2014. **587**: p. 613-617.
310. Pan, Z., et al., *High-Efficiency "Green" Quantum Dot Solar Cells.* Journal of the American Chemical Society, 2014. **136**(25): p. 9203-9210.
311. Duy-Cuong Nguyen, S.I., Ken Fukatsu, and Keiji Tanimoto. *Making nanoparticle ink for compound solar cells*. SPIE, 2013.
312. Kahan, A., M. Chi, and L. Friedman, *Infrared transitions in strained-layer GexSi1−x/Si.* Journal of Applied Physics, 1994. **75**(12): p. 8012-8021.
313. Basu, P.K., G. Sen, and B. Mukhopadhyay. *Feasibilty of laser action in strained Ge and Group IV alloys on Si platform.* in *Emerging Trends in Electronic and Photonic Devices & Systems, 2009. ELECTRO '09. International Conference on*. 2009.
314. Soref, R.A., L. Friedman, and G. Sun, *Silicon intersubband lasers.* Superlattices and Microstructures, 1998. **23**(2): p. 427-439.

315. Liu, J., et al., *Tensile strained Ge p-i-n photodetectors on Si platform for C and L band telecommunications.* Applied Physics Letters, 2005. **87**(1): p. 011110.
316. Gurdal, O., et al., *Low-temperature growth and critical epitaxial thicknesses of fully strained metastable Ge1−xSnx(x≲0.26) alloys on Ge(001)2×1.* Journal of Applied Physics, 1998. **83**(1): p. 162-170.
317. Piao, J., et al., *Molecular-beam epitaxial growth of metastable Ge1−xSnx alloys.* Journal of Vacuum Science & Technology B, 1990. **8**(2): p. 221-226.
318. Jamshidi, A., et al., *Growth of GeSnSiC layers for photonic applications.* Surface and Coatings Technology, 2013. **230**: p. 106-110.
319. Wortman, J.J. and R.A. Evans, *Young's Modulus, Shear Modulus, and Poisson's Ratio in Silicon and Germanium.* Journal of Applied Physics, 1965. **36**(1): p. 153-156.
320. Krishnamurthy, S., A. Sher, and A.B. Chen, *Generalized Brooks' formula and the electron mobility in SixGe1−x alloys.* Applied Physics Letters, 1985. **47**(2): p. 160-162.
321. Pairot, M., I. Zoran, and H. Paul, *Band structure calculations of Si–Ge–Sn alloys: achieving direct band gap materials.* Semiconductor Science and Technology, 2007. **22**(7): p. 742.
322. Aella, P., et al., *Optical and structural properties of SixSnyGe1−x−y alloys.* Applied Physics Letters, 2004. **84**(6): p. 888-890.
323. Radamson, H.H., et al., *Strain engineering in GeSnSi materials.* Sige, Ge, and Related Compounds 5: Materials, Processing, and Devices, 2012. **50**(9): p. 527-531.
324. Wirths, S., et al., *Reduced Pressure CVD Growth of Ge and Ge1-xSnx Alloys.* Ecs Journal of Solid State Science and Technology, 2013. **2**(5): p. N99-N102.
325. Vincent, B., et al., *Undoped and in-situ B doped GeSn epitaxial growth on Ge by atmospheric pressure-chemical vapor deposition.* Applied Physics Letters, 2011. **99**(15).
326. Werner, J., et al., *Germanium-tin p-i-n photodetectors integrated on silicon grown by molecular beam epitaxy.* Applied Physics Letters, 2011. **98**(6).
327. Oehme, M., et al., *Room-Temperature Electroluminescence From GeSn Light-Emitting Pin Diodes on Si.* Ieee Photonics Technology Letters, 2011. **23**(23): p. 1751-1753.
328. Radamson, H.H., et al., *Strain Engineering in GeSnSi Materials.* ECS Transactions, 2013. **50**(9): p. 527-531.
329. Kouvetakis, J. and A.V.G. Chizmeshya, *New classes of Si-based photonic materials and device architectures via designer molecular routes.* Journal of Materials Chemistry, 2007. **17**(17): p. 1649-1655.
330. Noroozi, M., et al., *CVD Growth of GeSnSiC Alloys Using Disilane, Digermane, Tin Tetrachloride and Methylsilane*, in *Sige, Ge, and Related Compounds 6: Materials, Processing, and Devices*, D. Harame, et al., Editors. 2014. p. 703-710.
331. Soref, R., J. Kouvetakis, and J. Menendez, *Advances in SiGeSn/Ge technology*, in *Group IV Semiconductor Nanostructures-2006*, L. Tsybeskov, et al., Editors. 2007. p. 13-24.
332. Moontragoon, P., et al., *Electronic properties calculation of Ge1 − x − ySixSny ternary alloy and nanostructure.* Journal of Non-Crystalline Solids, 2012. **358**(17): p. 2096-2098.

333. D'Costa, V.R., et al., *Tunable Optical Gap at a Fixed Lattice Constant in Group-IV Semiconductor Alloys.* Physical Review Letters, 2009. **102**(10).
334. Menéndez, J. and J. Kouvetakis, *Type-I Ge/Ge1−x−ySixSny strained-layer heterostructures with a direct Ge bandgap.* Applied Physics Letters, 2004. **85**(7): p. 1175-1177.
335. Moontragoon, P., Z. Ikonic, and P. Harrison, *Band structure calculations of Si-Ge-Sn alloys: achieving direct band gap materials.* Semiconductor Science and Technology, 2007. **22**(7): p. 742-748.
336. Soref, R.A. and L. Friedman, *Direct-gap Ge/GeSn/Si and GeSn/Ge/Si heterostructures.* Superlattices and Microstructures, 1993. **14**(2–3): p. 189-193.
337. Baribeau, J.-M., N.L. Rowell, and D.J. Lockwood. *Self-assembled SiGe dots*. 2005.
338. Wang, K.L., S. Tong, and H.J. Kim, *Properties and applications of SiGe nanodots.* Materials Science in Semiconductor Processing, 2005. **8**(1–3): p. 389-399.
339. Kouvetakis, J., et al., *Practical Materials Chemistry Approaches for Tuning Optical and Structural Properties of Group IV Semiconductors and Prototype Photonic Devices.* Photonics Journal, IEEE, 2010. **2**(6): p. 924-941.
340. *International Technology Roadmap for Semiconductors (ITRS).* 2011.
341. Jan, C.H., et al., *A 65nm ultra low power logic platform technology using uni-axial strained silicon transistors*. Ieee International Electron Devices Meeting 2005, Technical Digest. 2005. 65-68.
342. Luo, J., et al., *Surface-energy triggered phase formation and epitaxy in nanometer-thick Ni1−xPtx silicide films.* Applied Physics Letters, 2010. **96**(3): p. 031911.
343. Zhang, Z., et al., *Morphological stability and specific resistivity of sub-10 nm silicide films of Ni1−xPtx on Si substrate.* Applied Physics Letters, 2010. **96**(7): p. 071915.
344. Ortolland, C., et al. *Silicide yield improvement with NiPtSi formation by laser anneal for advanced low power platform CMOS technology*. in *Electron Devices Meeting (IEDM), 2009 IEEE International*. 2009.
345. Vandenabeele, P. and K. Maex, *Influence of temperature and backside roughness on the emissivity of Si wafers during rapid thermal processing.* Journal of Applied Physics, 1992. **72**(12): p. 5867-5875.
346. Shima, A., et al. *Dopant profile engineering of CMOS devices formed by non-melt laser spike annealing*. in *VLSI Technology, 2005. Digest of Technical Papers. 2005 Symposium on*. 2005.
347. Buchta, R., et al., *Temperature control during chemical vapor deposition of polycrystalline silicon with substrate heating by microwaves.* Applied Physics Letters, 1993. **62**(24): p. 3153-3155.
348. Xu, P., et al., *Ultra-shallow junctions formed using microwave annealing.* Applied Physics Letters, 2013. **102**(12).
349. Hu, C., et al., *Characterization of Ni(Si,Ge) films on epitaxial SiGe(100) formed by microwave annealing.* Applied Physics Letters, 2012. **101**(9): p. 092101.
350. Jarmar, T., et al., *Morphological and phase stability of nickel–germanosilicide on Si1−xGex under thermal stress.* Journal of Applied Physics, 2002. **92**(12): p. 7193-7199.

351. Seger, J., et al., *Increased nucleation temperature of NiSi2 in the reaction of Ni thin films with Si1−xGex.* Applied Physics Letters, 2002. **81**(11): p. 1978-1980.
352. Seger, J., et al., *Morphological instability of NiSi1−uGeu on single-crystal and polycrystalline Si1−xGex.* Journal of Applied Physics, 2004. **96**(4): p. 1919-1928.
353. Henry, H.R. and H. Julius, *Application of high-resolution x-ray diffraction for detecting defects in SiGe(C) materials.* Journal of Physics: Condensed Matter, 2005. **17**(22): p. S2315.
354. Jamshidi, A., et al., *Efficiency Enhanced Colloidal Mn-Doped Type II Core/Shell ZnSe/CdS Quantum Dot Sensitized Hybrid Solar Cells.* Journal of Nanomaterials, 2015. **2015**: p. 9.
355. Ning, Z., et al., *Solar cells sensitized with type-II ZnSe-CdS core/shell colloidal quantum dots.* Chemical Communications, 2011. **47**(5): p. 1536-1538.
356. Sahraei, R., G.M. Aval, and A. Goudarzi, *Compositional, structural, and optical study of nanocrystalline ZnS thin films prepared by a new chemical bath deposition route.* Journal of Alloys and Compounds, 2008. **466**(1-2): p. 488-492.
357. Dizaji, H.R., A.J. Zavaraki, and M.H. Ehsani, *Effect Of Thickness On The Structural And Optical Properties Of Zns Thin Films Prepared By Flash Evaporation Technique Equipped With Modified Feeder.* Chalcogenide Letters, 2011. **8**(4): p. 231-237.
358. Liu, M., et al., *L-Cystine-assisted hydrothermal synthesis of Mn1-xCdxS solid solutions with hexagonal wurtzite structure for efficient photocatalytic hydrogen evolution under visible light irradiation.* Journal of Materials Chemistry A, 2014. **2**(13): p. 4619-4626.
359. Chauhan, R., A. Kumar, and R.P. Chaudhary, *Synthesis, structural and photocatalytic studies of Mn-doped CdS nanoparticles.* Research on Chemical Intermediates, 2013. **39**(2): p. 645-657.
360. Elango, M., et al., *Structural, optical and magnetic studies on non-aqueous synthesized CdS:Mn nanomaterials.* Journal of Alloys and Compounds, 2012. **538**: p. 48-55.
361. Zhai, H., et al., *Synthesis, structural and optical properties of water-soluble Mn-doped CdS nanocrystals.* Micro & Nano Letters, 2011. **6**(4): p. 257-260.
362. Ido, T., *Energy Bandgap And Lattice-Constant Contours Of 2-6 Quaternary Alloys.* Journal of Electronic Materials, 1980. **9**(5): p. 869-882.
363. Bufler, F.M., et al., *Full band Monte Carlo investigation of electron transport in strained Si grown on Si1-xGex substrates.* Applied Physics Letters, 1997. **70**(16): p. 2144-2146.
364. Dollfus, P., S. Galdin, and P. Hesto, *Monte-Carlo investigation of in-plane electron transport in tensile strained Si and Si1-yCy (y <= 0.03).* European Physical Journal-Applied Physics, 1999. **7**(1): p. 73-77.
365. Wang, Y.G., et al., *Improvement of electron transport in a ZnSe nanowire by in situ strain.* Journal of Physics D-Applied Physics, 2011. **44**(12).
366. Mora-Sero, I., et al., *Recombination in Quantum Dot Sensitized Solar Cells.* Accounts of Chemical Research, 2009. **42**(11): p. 1848-1857.
367. Guijarro, N., et al., *Uncovering the role of the ZnS treatment in the performance of quantum dot sensitized solar cells.* Physical Chemistry Chemical Physics, 2011. **13**(25): p. 12024-12032.

368. Yu, X.-Y., et al., *Highly efficient CdTe/CdS quantum dot sensitized solar cells fabricated by a one-step linker assisted chemical bath deposition.* Chemical Science, 2011. **2**(7): p. 1396-1400.
369. Itzhakov, S., et al., *Type-II Quantum-Dot-Sensitized Solar Cell Spanning the Visible and Near-Infrared Spectrum.* Journal of Physical Chemistry C, 2013. **117**(43): p. 22203-22210.
370. Balet, L.P., et al., *Inverted core/shell nanocrystals continuously tunable between type-I and type-II localization regimes.* Nano Letters, 2004. **4**(8): p. 1485-1488.
371. Yu, K.M., et al., *Effect of the location of Mn sites in ferromagnetic Ga1-xMnxAs on its Curie temperature.* Physical Review B, 2002. **65**(20).
372. Gratzel, M., *Solar energy conversion by dye-sensitized photovoltaic cells.* Inorganic Chemistry, 2005. **44**(20): p. 6841-6851.
373. Kongkanand, A., et al., *Quantum dot solar cells. Tuning photoresponse through size and shape control of CdSe-TiO2 architecture.* Journal of the American Chemical Society, 2008. **130**(12): p. 4007-4015.
374. Ning, Z., et al., *Wave-Function Engineering of CdSe/CdS Core/Shell Quantum Dots for Enhanced Electron Transfer to a TiO2 Substrate.* Journal of Physical Chemistry C, 2010. **114**(35): p. 15184-15189.
375. James, D.R., et al., *Distributions Of Fluorescence Lifetimes - Consequences For The Photophysics Of Molecules Adsorbed On Surfaces.* Chemical Physics Letters, 1985. **120**(4-5): p. 460-465.
376. A. Jamshidi , J.H., J. Fei , V. Chmyrov , J. Widengren , L. Sun , H. Ågren *Synthesize of Cd-Free and Low Toxic Cu2GeS3-Inp quantum dot for Infrared Solar Cell applications.* Manuscript, 2015.
377. A. Jamshidi , L.S., H. Ågren, *"Green" colloidal InP/ZnS quantum dots sensitized solar cell.* Manuscript, 2015.
378. Li, L., et al., *Efficient Synthesis of Highly Luminescent Copper Indium Sulfide-Based Core/Shell Nanocrystals with Surprisingly Long-Lived Emission.* Journal of the American Chemical Society, 2011. **133**(5): p. 1176-1179.
379. Uehara, M., et al., *Synthesis of CuInS2 fluorescent nanocrystals and enhancement of fluorescence by controlling crystal defect.* The Journal of Chemical Physics, 2008. **129**(13): p. 134709.
380. Li, T.-L., Y.-L. Lee, and H. Teng, *CuInS2 quantum dots coated with CdS as high-performance sensitizers for TiO2 electrodes in photoelectrochemical cells.* Journal of Materials Chemistry, 2011. **21**(13): p. 5089-5098.
381. J. Huang, B.X., A. Jamshidi, L. Sun and H. Ågren, *Photovoltaic Performance Improvement Strategy for Colloidal "green" CuInS2 QDs: Hybrid passivation vs ZnS shell.* Manuscript, 2015.
382. Jamshidi, A., et al., *Efficiency Enhanced Colloidal Mn-Doped Type II Core/Shell ZnSe/CdS Quantum Dot Sensitized Hybrid Solar Cells.* Journal of Nanomaterials.
383. Fabregat-Santiago, F., et al., *Characterization of nanostructured hybrid and organic solar cells by impedance spectroscopy.* Physical Chemistry Chemical Physics, 2011. **13**(20): p. 9083-9118.

384. Sun, J., J. Zhao, and Y. Masumoto, *Shell-thickness-dependent photoinduced electron transfer from CuInS2/ZnS quantum dots to TiO2 films.* Applied Physics Letters, 2013. **102**(5): p. 053119.